Quantum Sensing of 2D Magnets

Inauguraldissertation

zur
Erlangung der Würde eines Doktors der Philosophie
vorgelegt der
Philosophisch-Naturwissenschaftlichen Fakultät
der Universität Basel

von

Märta Tschudin

Basel, 2025

Genehmigt von der Philosophisch-Naturwissenschaftlichen Fakultät
auf Antrag von

Erstbetreuer: Prof. Dr. Patrick Maletinsky
Zweitbetreuer: Prof. Dr. Christian Schönenberger
Externer Experte: Prof. Dr. Roman Gorbachev

Basel, den 25.06.2024

Prof. Dr. Marcel Mayor
Dekan

Abstract

The discovery of two-dimensional (2D) magnetic materials has generated significant scientific interest due to their distinct properties from their bulk counterparts and their ability to host exotic phases such as magnetic moiré patterns and novel spin textures. Understanding 2D magnetism is essential for advancing technologies based on these materials, which hold great promise for spintronics applications.

To study magnetism in low dimensions, highly sensitive sensors with nanoscale spatial resolution and cryogenic compatibility are required, as most 2D magnets only exhibit long range magnetic order at low temperatures. Previous approaches, like electronic transport measurements and optical imaging, have limitations in terms of offering only indirect magnetization measurements and limited spatial resolution. To address these challenges, we use an innovative quantum sensor based on the Nitrogen-Vacancy (NV) center in diamond, which allows for quantitative magnetic imaging at the nanoscale under cryogenic conditions. Scanning NV magnetometry, where an NV center is positioned at the apex of a diamond tip, provides quantitative, high-resolution (~ 50 nm) magnetic stray field maps of measurement probes.

In this thesis, we apply single-spin scanning NV magnetometry to investigate 2D magnets. We examine the chromium-trihalides (CrX_3, X = {I, Br, Cl}) and present the first quantitative, nanomagnetic imaging of antiferromagnetic (AFM) interlayer coupling in few-layer CrI_3. Furthermore, we showcase our efforts towards imaging magnetic moiré patterns in CrX_3 and conclude that magnetic and structural disorder in the fragile CrX_3 compounds currently pose challenges for observing distinct, long range ($> \mu$ms length scale) periodic moiré patterns.

Furthermore, we explore the nanomagnetic properties of CrSBr, a newly discovered 2D magnet with promising magnetic stability, down to individual monolayers. Our results reveal insights into the ferromagnetic (FM) intralayer and AFM interlayer magnetic coupling, phase transitions, and anisotropies in few-layer CrSBr. Our studies demonstrate homogeneous magnetization and stable magnetic order down to monolayers below the critical temperature of CrSBr. We find that the AFM-FM spin-flip transition in bilayer CrSBr is driven by the nucleation and propagation of a phase wall, rather than a continuous rotation of the magnetic moments. Near the critical temperature of CrSBr, we observe reduced anisotropy in few-layer flakes, and we image magnetic inhomogeneities in odd-layer flakes, indicating local disorder in intralayer exchange couplings, potentially masking present 2D-XY behavior. Our findings show that the 2D magnet CrSBr emerges as a promising platform to study magnetic spin textures in 2D. With it, we control and image the initialization of AFM domain walls in bilayer CrSBr. We characterize the spin configuration within the domain wall core and gain insight into the underlying spin arrangement of few-layer CrSBr. This is one of the first observations of AFM domain walls in atomically thin vdW materials, which is a field that remains largely unexplored to date and is key for advancing vdW based applications for spintronic devices.

Our results on quantitative, nanoscale magnetic imaging of 2D magnets pave the way for engineering advanced materials and technological developments based on 2D systems.

Contents

List of symbols and abbreviations

NV center

θ_{NV}	Polar angle of NV axis
ϕ_{NV}	Azimuthal angle of NV axis
d_{NV}	Distance between NV and source
$\hat{\boldsymbol{S}}, \hat{S}_x, \hat{S}_y, \hat{S}_z$	Spin operator and components
$\boldsymbol{S}$	Spin vector
B_{NV}/ B_{ext}	Magnetic field (along NV axis)
$B_\perp$	Magnetic field (perpendicular to NV axis)
D_0	Zero-field splitting

Material Properties

$\boldsymbol{B}$	Magnetic flux density (Magnetic field)
$\boldsymbol{H}$	Magnetic flux intensity
$\boldsymbol{m}$	Magnetic moment
$\boldsymbol{M}$	Magnetization
χ	Susceptibility
K	Anisotropy constant (micromagnetics)
J	Exchange parameter (lattice)
a,b,c	Crystal axes

Constants

$g_e = 2.0028$	Electronic g-factor
$\gamma_{\mathrm{NV}} = 28.0\,\mathrm{MHz/mT}$	Gyromagnetic ratio of NV spin
$h = 6.626 \cdot 10^{-34}\,\mathrm{m^2\,kg/s}$	Planck's constant
$\hbar = 1.055 \cdot 10^{-34}\,\mathrm{m^2\,kg/s}$	Reduced Planck's constant
$k_B = 1.381 \cdot 10^{-23}\,\mathrm{J/K}$	Boltzmann constant
$\mu_B = 9.274 \cdot 10^{-24}\,\mathrm{J/T}$	Bohr magneton
$\mu_0 = 4\pi \cdot 10^{-7}\,\mathrm{N/A^2}$	Vacuum permeability

Abbreviations

2D	two-dimensional
AFM	Antiferromagnet(ic)
	atomic force microscope
BKT	Berezinskii-Kosterlitz-Thouless
CrX_3	chromium-trihalides
CW	Continuous wave
DMI	Dzyaloshinskii-Moria interaction
DW	Domain wall
FM	Ferromagnet(ic)
hBN	hexagonal boron nitride
MCD	Magnetic Circular Dichroism
MFM	Magnetic force microscopy
MOKE	Magneto-Optical Kerr Effect
MW	Microwave
NA	Numerical aperture
NV	Nitrogen Vacancy
NV^-	Negatively charged NV center
NV^0	Neutral NV center
ODMR	Optically detected magnetic resonance
PL	Photoluminescence
SQUID	Superconducting quantum interference device
vdW	van der Waals
ZFS	Zero field splitting
ZPL	Zero-phonon line

1

Optical table with lenses © Märta Tschudin

1. Introduction

Magnetism is a manifestation of one of the fundamental forces in physics and is crucial to numerous everyday technologies. From the swipe on our smartphones to the storage of information, magnetic materials play an integral role. Traditionally, these technologies have relied on bulk, three-dimensional magnetic materials, extensively studied over the years. For some time it was believed that long range magnetic order could only stabilize in three dimensions and that two-dimensional magnetism could not exist, since spin-waves, collective excitations of magnetic moments, would destroy any long-range order in 2D lattices with continuous symmetry [1]. However, by breaking continuous symmetry in 2D crystals, the spin-waves only exist at a finite energy, and thus magnetic order can form and persist down to two-dimensions.

A recent, groundbreaking development in modern condensed matter physics has emerged as a unique platform to investigate 2D magnetism: the discovery of two-dimensional (2D) van der Waals (vdW) materials. These materials exhibit distinct properties from their bulk counterparts and host novel magnetic phases and phenomena, such as magnetic moiré patterns and spin textures, which can be challenging to realize in bulk systems [2]. The clean interfaces of 2D materials allows for combining and twisting different materials into heterostructures with atomically smooth boundaries, which offers countless possibilities of engineering novel material properties. Studying 2D magnets has the potential to lead to breakthroughs in fundamental physics and enables the development of advanced technologies, including low-power spintronic devices and quantum computing components [2, 3].

The field of vdW materials emerged with the discovery of graphene, a single layer of carbon atoms exfoliated from graphite 20 years ago [4, 5]. These vdW materials are composed of individual 2D sheets of bound atoms held together by weak vdW forces, allowing for separation down to single atomic layers and the combination into new materials with novel properties. Since the discovery of graphene, the field has rapidly expanded, revealing a diverse "zoo"[1] of 2D materials with various properties. However, a key member of this family - 2D magnets - was missing until their recent experimental discovery in 2017 [6, 7]. The identification of 2D magnets has opened new avenues for exploring magnetism in two dimensions, providing a unique platform for investigating numerous physical phenomena in 2D, such as domain wall formation [8, 9], magnetic moiré structures [10–12], and spin arrangements like skyrmions [13].

To study magnetism of atomically thin 2D magnets, sensitive magnetic probes are required, which can resolve the underlying physical phenomena on the nanoscale under cryogenic conditions, as most of the 2D magnets only exhibit magnetic order at low temperatures. The first studies on 2D magnets mostly relaid on electronic transport, which lacks spatial resolution and cannot directly image magnetic order, or on optical

[1] Pay a visit to the zoo in Appendix A.5!

probes, which suffer from a limited spatial resolution [6, 7]. A novel approach to studying 2D magnetic materials involves using a versatile quantum sensor based on an atomic defect in diamond - scanning Nitrogen-Vacancy (NV) magnetometry. The high sensitivity of this quantum sensor allows for detailed insight into the yet to be explored magnetism of 2D materials, which is key for advancing fundamental research on these newly discovered materials.

Scanning NV magnetometry is a powerful technique for high-resolution magnetic imaging of 2D materials, including vdW magnets, even under cryogenic conditions [14]. This method utilizes the NV center spin in diamond as a sensitive magnetic quantum sensor, which can be precisely controlled and read out using optical and microwave techniques [15]. In scanning NV magnetometry, a diamond tip with a single NV center at its apex is brought close to the sample surface. By scanning the diamond tip across the sample and measuring the shift of the electron spin resonance frequency of the NV center, a high-resolution magnetic stray field map is generated. The non-invasive, versatile nature of this technique, combined with high spatial resolution (<50 nm [16]) and magnetic field sensitivity on the order of $\mu\mathrm{T}/\sqrt{\mathrm{Hz}}$ [17], makes scanning NV magnetometry an excellent tool for probing magnetic properties and phenomena in 2D magnets.

In this thesis, we demonstrate the capability of scanning NV magnetometry to image various magnetic phases in 2D magnets. We first focus on the chromium-trihalide family, CrX_3 (X = {I, Br, Cl}), and present the first quantitative, nanomagnetic imaging of antiferromagnetic interlayer coupling in few-layer CrI_3, one of the earliest discovered 2D magnets. Magnetic exchange in CrI_3 is coupled to the structural order in the lattice [14, 18]. This effect can be exploited to create magnetic moiré patterns. Magnetic moirés form an interesting platform to study exotic magnetic phases such as skyrmions [19, 20], noncollinear spin textures [10], and moiré magnons [10] . We detail our efforts towards imaging moiré patterns in CrX_3 and discuss the current limitations due to magnetic and structural disorder. In order to make 2D magnets application-ready, it is thus crucial to discover and study more robust 2D magnetic vdW systems.

In light of the discovery of a novel class of more robust 2D magnets, we study nanomagnetism in CrSBr, a 2D magnet with promising air-stability. Our studies provide insights into the magnetic order, phase transitions, and anisotropies in this system. We observe a remarkably homogeneous magnetization in CrSBr (within our spatial resolution of $\sim$ 50 nm), and ambient stability of the magnetic order down to individual monolayers. Furthermore, we explore the AFM-FM spin-flip transition in bilayer CrSBr and find it to be driven by the nucleation and propagation of a phase wall, rather than a continuous rotation of the layer magnetization. We also examine the evolution of magnetization near the critical temperature T_N of CrSBr, directly evidencing the reduction of anisotropy as T_N is approached. Near T_N, we detect the onset of magnetic inhomogeneities in odd-layer flakes, attributed to local disorder in intralayer exchange couplings that obscure a possible 2D-XY behavior of CrSBr in this intermediate temperature regime.

By studying spin textures in few-layer CrSBr, we uncover the presence of AFM domain walls in bilayer CrSBr. While AFM domains are highly relevant for spintronics applications due to their reduced susceptibility to magnetic perturbations, they have primarily been observed in thin films or thick vdWs materials [21–24]. The observation

of AFM domain walls in atomically thin vdW materials remains largely unexplored. Here, we demonstrate the initialization of AFM domain walls in bilayer CrSBr for the first time. Combining our measurements with micromagnetic simulations, we evaluate possible configurations of spins within the domain wall core. Our findings suggest that the domain wall consists of an AFM core, where spins in the two CrSBr layers couple antiferromagnetically, but their rotation center is slightly shifted, resulting in a measurable stray field. We further identify a signature of the creation of an AFM domain wall in the observation of an FM cusp shaped region which forms in the FM-to-AFM spin-flip transition. These experiments provide valuable insights into the spin configuration of individual CrSBr layers and domain wall configurations, paving the way for developing spintronics applications based on vdW structures.

Structure of this thesis

This thesis has the following structure: Chapter 2 introduces vdW materials, with a focus on 2D magnets. We give a short overview of various magnetic imaging techniques used for studying 2D magnets and emphasize the advantages of single-spin magnetometry based on NV centers in diamond. We explain the basic principles and capabilities of magnetic field sensing using scanning NV magnetometry, demonstrating its effectiveness by imaging magnetism in the chromium-trihalides, CrX_3 (X = {I, Br, Cl}).

Chapter 3 describes the experimental methods for obtaining 2D magnetic samples and for setting up a scanning NV magnetometry system at cryogenic temperatures. For the sample fabrication, we discuss mechanical exfoliation and polymer-free stacking techniques for building vdW heterostructures. For the cryogenic scanning setup, we detail the components of the NV diamond sensor and summarize the key parts of the scanning probe cryostat.

Chapter 4 presents our results on imaging nanomagnetism in the novel 2D magnet CrSBr. Our studies provide a quantitative, nanoscale analysis of magnetization strength and anisotropy in few-layer CrSBr samples, addressing two key magnetic phase transitions through direct magnetic imaging using single-spin magnetometry.

Chapter 5 demonstrates one of the first successful initialization and detection of AFM domain walls in atomically thin vdW magnets. By combining our experimental findings with micromagnetic simulations, we extract information on the spin arrangement within the domain wall core and gain insight into the spin configuration of individual CrSBr layers.

The thesis concludes with a summary and an outlook in chapter 6, on future advancements in the field of scanning probe techniques for imaging magnetic phenomena at the nanoscale.

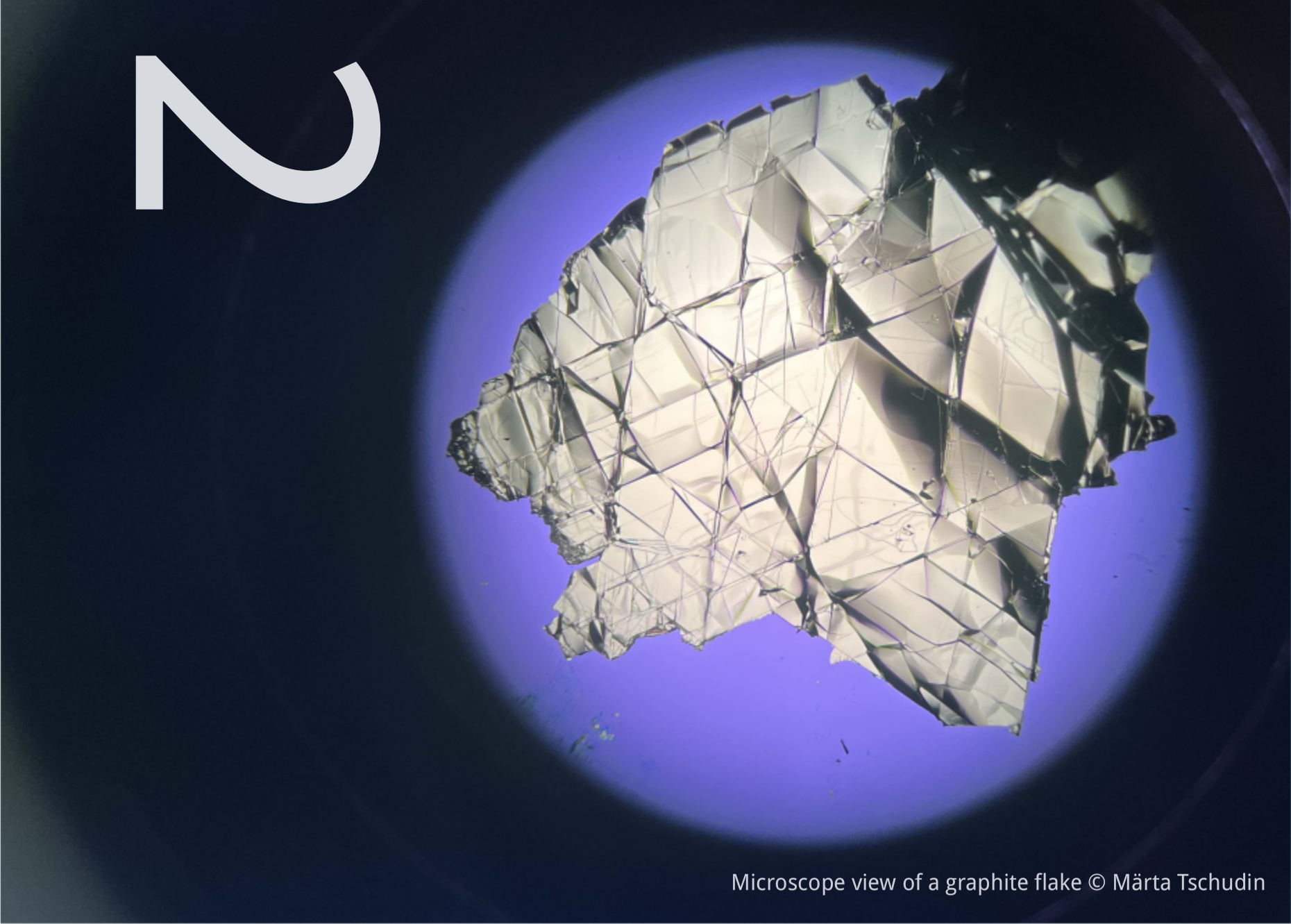

Microscope view of a graphite flake © Märta Tschudin

2. Scanning Nitrogen-Vacancy Magnetometry of 2D Magnets

2.1. Van der Waals materials

Since the discovery of graphene, a single layer of carbon atoms isolated from graphite [4, 25] (Nobel Prize in Physics, 2010), the field of two-dimensional (2D) van der Waals (vdW) materials has rapidly expanded, attracting significant scientific interest. These materials consist of 2D sheets of bound atoms held together by weak vdW forces, allowing them to be peeled apart down to monolayers. In the last decade, the existence of a wide range of vdW materials has been predicted and studied, including insulators, metals, semiconductors, superconductors, topological materials, and magnets [26, 27].

The motivation for studying 2D materials lies in their distinct and often enhanced physical properties compared to their bulk counterparts. As vdW materials are thinned to the 2D limit, they exhibit for example changes in the band structure [28] or crystal stacking order [14, 18], which opens a playground for discovering new physical phenomena and phases.

One major advantage of vdW materials is the ability to combine different 2D sheets into new materials with atomically smooth interfaces. These individual sheets can be readily exfoliated from bulk crystals using adhesive tape (see section 3.1 for details) and then combined into so called vdW heterostructures, where different 2D materials are stacked on top of each other. Additionally, vdW materials can be handled independently of substrates due their weak interaction with surfaces. They can, for example, be conveniently placed on pre-patterned electrical contacts, suspended, or placed on specific substrates, such as diamond surfaces [29, 30], for sensing applications. Moreover, the twist degree of freedom in combining 2D materials introduces new phases, as demonstrated by the emergence of superconductivity in magic-angle twisted bilayer graphene [31]. Such moiré physics has already led to many intriguing discoveries in condensed matter physics [32–34]. Overall, vdW materials provide an excellent platform for discovering novel magnetic phases in two dimensions.

2.2. Van der Waals magnets

In the first decade following the discovery of vdW materials, 2D magnets were notably absent. It was only in 2017 that long-range magnetic order in monolayer 2D magnets CrI_3 [6] and $Cr_2Ge_2Te_6$ [7] was demonstrated. The introduction of 2D magnets into the family of vdW materials has generated great interest, as - from a fundamental research perspective - 2D magnets open new avenues for investigating phase transitions and novel magnetic phases in two dimensions [3], such as domain wall formation [8, 9],

magnetic moiré structures [10–12], and spin arrangements like skyrmions [13]. This is particularly important because reduced dimensionality can significantly alter the magnetic behavior of materials, revealing new physical phenomena that are not present or are difficult to observe in three-dimensional systems [2].

Furthermore, integrating 2D magnets into vdW heterostructures allows for the study of magnetic exchange interactions at interfaces, providing insights into interlayer coupling [6, 14], spin transfer and proximity effects [35, 36]. Combing 2D magnets into heterostructures also opens up the potential for tuning magnetic properties through external fields [37] or strain [38]. These findings can lead to the development of novel, vdW materials based devices. From an application-driven viewpoint, 2D magnets therefore hold great potential as building blocks for high-efficiency, low-power spintronic devices, such as magnetic components for quantum computing, and other advanced technologies [2, 3].

In the following sections, we will discuss the origin of magnetic order in vdW materials and present an overview of different magnetic phenomena, which can occur in 2D magnets, such as exotic spin textures or engineered moiré structures. Studying magnetism in vdW materials poses challenges due to the need for measurement techniques sensitive enough to detect magnetic moments of individual atomic layers. In section 2.2.3, we will summarize common imaging methods for studying 2D magnets. We will highlight the advantages of single-spin magnetometry based on Nitrogen-Vacancy (NV) centers in diamond for studying vdW magnets and discuss the fundamentals of this imaging technique in section 2.3. Finally, in section 2.4, we will demonstrate how scanning NV magnetometry can be applied to study magnetism in chromium-trihalides, one of the first discovered families of 2D magnets.

2.2.1. Magnetism in 2D

Magnetic order in 2D systems can be theoretically described by several models, which depend on the degree of freedom of the spins/ magnetic moments [39].

The most general case is the isotropic Heisenberg model, where spins can orient in any direction with the crystal lattice, see Fig 2.1a. The corresponding Hamiltonian (only considering nearest neighbor interactions) is given by:

$$\mathcal{H}_{\text{Heisenberg}} = -\sum_{i<j} J\left(\hat{S}_i^x \hat{S}_j^x + \hat{S}_i^y \hat{S}_j^y + \hat{S}_i^z \hat{S}_j^z\right), \tag{2.1}$$

where J is the nearest neighbor exchange coupling and $\hat{S}^{x,y,z}$ are the spin operators at the i and j sites. By definition, a material is ferromagnetic (FM) for $J > 0$ and antiferromagnetic (AFM) for $J < 0$. According to the Mermin Wagner theorem [1], no long range magnetic order can exist in such an isotropic spin system in 2D. This is because gapless excitations, i.e. thermally excited spin-waves (whose quanta are denoted as magnons), will prevent any long range order in such systems. However, by introducing anisotropy in the system and hence opening a gap in the magnon spectrum, magnetic order can be restored in 2D at nonzero temperatures, up to the Curie temperature. Anisotropy can be introduced for example by magnetocrystalline anisotropy, i.e. the interaction between the magnetic ion and its surrounding crystalline field.

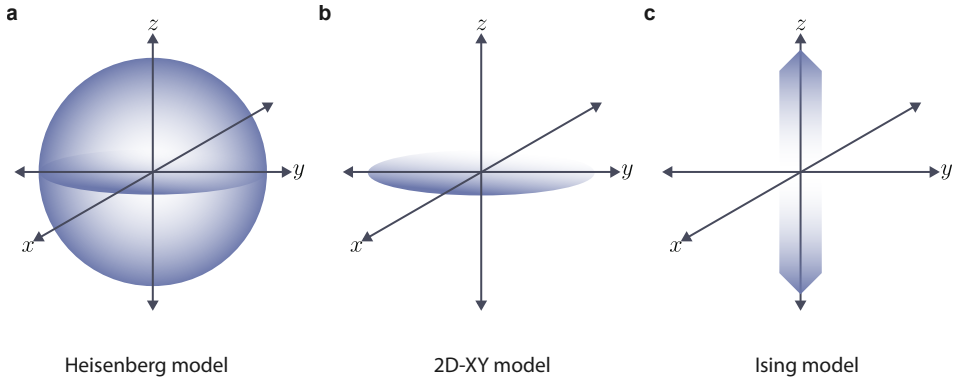

Figure 2.1.: Magnetic spin ordering models. **a** In the Heisenberg model, the magnetic moment can freely rotate within a three-dimensional sphere with out any energy penalty. **b** In the 2D-XY model, the magnetic spins can freely rotate within a plane, i.e. the xy-plane. **c** In the anisotropic Ising model, the spins are locked to align along one axis, here depicted for the z-axis.

Reducing the magnetic moment's degree of freedom to a two-dimensional plane, results in the 2D-XY model, which is described by the Hamiltonian:

$$\mathcal{H}_{\mathrm{XY}} = -\sum_{i<j} J_{xy} \left(\hat{S}_i^x \hat{S}_j^x + \hat{S}_i^y \hat{S}_j^y \right). \tag{2.2}$$

In the 2D-XY model, the spins can point into any direction within, for example, the xy-plane, see Fig. 2.1b, without any energy penalty. As a result, only "quasi" long range magnetic order can be observed in such systems at finite temperature, by introducing an easy-plane magnetic anisotropy. The corresponding phase transition is termed Berezinskii–Kosterlitz–Thouless (BKT) transition and can allow for the formation of spin vortex and anti-vortex pairs.

Restricting the magnetic spin's degree of freedom further, results in the Ising model:

$$\mathcal{H}_{\mathrm{Ising}} = -\sum_{i<j} J_z \hat{S}_i^z \hat{S}_j^z. \tag{2.3}$$

In this model, each spin is restricted to point along an anisotropy defined axis, i.e. the spin can point up or down for an Ising model with uniaxial anisotropy along the z-axis, as illustrated in Fig. 2.1c. In the Ising model, long range magnetic order can be established, because finite energy is required to tilt the spins off axis, which would destroy their magnetic alignment.

The first realization of 2D vdW magnets was achieved in 2017, where researches have demonstrated long range magnetic order down to monolayer flakes in CrI_3 [6] and in $Cr_2Ge_2Te_6$ [7] using optical imaging via the Kerr effect. Together with Raman spectroscopy on $FePS_3$ [40], these discoveries started the field of 2D magnetism based on vdW materials. While these materials are all Ising-types of 2D magnets with easy-axis anisotropy, in the following years more and more 2D magnetic materials have

been discovered and explored [2, 3, 41, 42], covering also different spin Hamiltonian classes, such as $CrCl_3$ for example, which, in the monolayer limit, is a candidate for the 2D-XY model [43].

2.2.2. Spin textures in 2D magnets

In recent years, significant efforts have been dedicated to studying the magnetic ground states and excitations in 2D magnets. Understanding the formation of (non-)collinear spin textures, the excitation of spin waves, and the coupling between lattice, charge, and magnetic moments in vdW magnets is crucial [39]. This knowledge will ultimately enable control over magnetic order, advancing 2D magnets toward application-ready technologies.

One important aspect of studying 2D magnets is gaining insight into phase transitions and domain formation, where the domain walls, i.e. the boundaries between different magnetic domains, exhibit unique properties and dynamics. Investigating domain walls in 2D magnets can reveal fundamental mechanisms of magnetism. For example, the spin-rotation within a domain wall (Bloch wall versus Néel wall) and the domain wall width can provide important information on exchange interactions and anisotropy within the material [44]. The domain wall width δ_{DW}, for example, depends on magnetic exchange J and anisotropy K: $\delta_{\mathrm{DW}} = \sqrt{J/K}$. Studying the evolution of domains [8, 9, 29] in 2D magnets is crucial, i.e. for the development of new magnetic storage technologies based on vdW magnets.

Furthermore, 2D magnets allow for the exploration of magnetic moiré structures, which arise when two layered materials with slightly mismatched lattices are stacked, creating a moiré pattern [10]. In moiré structures formed by twisting vdW materials with intrinsic magnetism, stacking order-dependent lattice configurations [14, 45, 46] can lead to a modulation of AFM and FM lattice sites when twisting two adjacent layers, resulting in a magnetic moiré pattern. Theoretical calculations predict various novel phases in magnetic moiré structures, including skyrmions [19, 20], noncollinear spin textures [10] and moiré magnons [47]. Recent experimental works on twisted CrI_3 have demonstrated coexisting layered AFM and FM phases [11, 48] and non-collinear spin textures [49]. This emerging field of magnetic moiré physics holds promise for discovering many novel phases and physical phenomena.

In the context of magnetic spin textures, 2D magnets provide a platform for studying exotic spin arrangements like skyrmions, which are topologically protected spin textures. Skyrmions and chiral spin textures can be stabilized by antisymmetric exchange interactions, such as the Dzyaloshinskii-Moriya interaction (DMI). Although few 2D magnets with intrinsic DMI have been discovered (NiI_2 has shown spiral magnetic order and associated DMI [50]), the thin nature of vdW materials allows DMI to be induced by proximity, as demonstrated in WTe_2/Fe_3GeTe_2 heterostructures where skyrmions have been observed [13].

To expand our understanding of the magnetic order in various spin arrangements and textures in 2D magnets, it is crucial to study them with appropriate measurement techniques. In the next section, we will highlight some common imaging and microscopy techniques for studying 2D magnets.

2.2.3. Methods for imaging 2D magnets

Experimental probes adapted to sense signals in small, micron-sized 2D magnetic samples are essential for investigating magnetism in van der Waals (vdW) materials. While magneto-transport measurements provide valuable information on electronic properties and magnetic transitions, for example by tunneling magneto resistance [51–53], they lack spatial resolution and cannot directly visualize magnetic domains or local variations in magnetization. Thus, imaging techniques are crucial for a comprehensive understanding of 2D magnets. There are two main types of imaging microscopy techniques for studying 2D magnets: Optical imaging techniques, which are fast and robust but have diffraction-limited spatial resolution. And scanning probe microscopy techniques, which are usually more complex regarding their experimental realization, but offer spatial resolutions from tens of nm down to individual atoms.

Common optical imaging techniques include the Magneto-Optical Kerr Effect (MOKE), which detects changes in polarization due to magnetization, and Magnetic Circular Dichroism (MCD), which measures differential absorption and the phase difference of circularly polarized light. These techniques have been used to unravel antiferromagnetic order in few-layer CrI_3 [6], detect the FM onset of magnetization in Fe_3GeTe_2 [54] or study optical control of AFM order in $MnBi_2Te_4$ [55]. MOKE and MCD have also been used to study 2D magnetic moiré superlattices, for example in CrI_3, to demonstrate the coexistance of FM and AFM states [48] and non-collinear spin textures [49]. Another optical imaging technique includes exciton-based imaging, which probes the interplay between excitons and magnetic order and has been applied for example to study magnetic order in CrSBr [56, 57]. While these techniques provide insight into the fundamental magnetism of 2D magnets, they are mostly qualitative and limited by diffraction, providing a spatial resolution of a few hundreds of nm, and are thus not able to spatially resolve features of magnetic moirés or domain walls.

A quantitative, optical microscopy technique for direct magnetic imaging is widefield Nitrogen-Vacancy (NV) magnetometry, where an ensemble of NV centers within a thin diamond membrane sense the stray fields from magnetic probes placed on the diamond surface. This technique has been used to study various 2D magnets , including for example VI_3 [29], $MnBi_2Te_4$ [58], twisted CrI_3 [12] and CrSBr [30]. While widefield magnetometry can operate in a wide temperature range, it is limited to spatial resolutions of a couple hundreds of nm (diffraction limit) and is thus not able to directly resolve spin structures smaller than 100 nm.

Scanning probe techniques, on the other hand, offer higher spatial resolution. Spin-Polarized Scanning Tunneling Microscopy (SP-STM), for example achieves atomic-scale resolution and has been used to investigate stacking order dependent magnetism in $CrBr_3$ [59]. This technique, however, is limited to operation with conductive substrates and extracting quantitative information on the magnetism is difficult, since SP-STM mostly measures qualitative contrast between regions of different magnetization and decoupling interactions from the tip with the sample can be complicated. Another scanning probe technique is Magnetic Force Microscopy (MFM), which is based on measuring the interactions between a sharp, magnetic scanning tip and a substrate. This technique has been employed to image magnetism in thick CrI_3 [60] and VSe_2 [61] and thin CrSBr [62]. While MFM operates in a large temperature range, from cryogenic environments to room temperature and provides $<$ 100 nm

spatial resolution [62], it is an invasive microscopy technique, as the magnetic tip can influence/perturb the magnetism of the measured sample. Furthermore, it is an indirect measurement of the stray field and it is difficult to extract quantitative magnetization information from MFM.

One of the most sensitive magnetometry probes are scanning SQUIDs (Superconducting Quantum Interference Device) [63], which have been used to image, for example, orbital magnetism in twisted bilayer graphene (SQUID on tip) [64] and magnetic textures in few-layer $Cr_2Ge_2Te_6$ (SQUID on lever) [65]. However, the SQUID sensitivity scales with the SQUID pick up loop size and therefore compromises spatial resolution. For small pick up loops of scanning SQUID on tips [66] or SQUID on cantilevers [67], spatial resolutions in the order of $50-100$ nm can be achieved. Since SQUIDS have to operate in the superconducting regime, they are limited to cryogenic applications.

Scanning NV magnetometry, in contrast, combines high spatial resolution (<50 nm) with non-invasive measurement capabilities in a variable temperature regime, making it a versatile tool to study 2D magnets. In the following sections we discuss the fundamentals of scanning NV magnetometry.

2.3. Scanning Nitrogen-Vacancy magnetometry

Scanning NV magnetometry is a powerful technique for detailed nanoscale magnetic imaging of 2D materials, including vdW magnets, even under cryogenic conditions [14]. This method utilizes the NV center spin in diamond as a sensitive, magnetic quantum sensor. NV centers are highly responsive to magnetic fields and can be precisely controlled and read out using optical and microwave (MW) techniques [15]. In scanning NV magnetometry, a diamond tip with a single NV center at

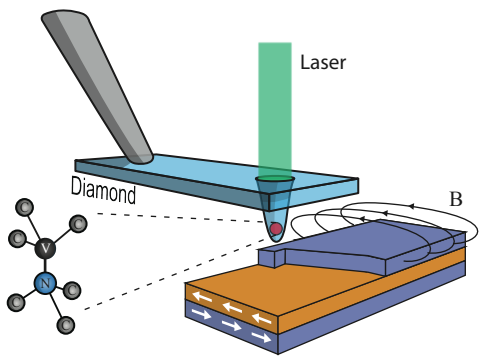

Figure 2.2.: Illustration of a scanning NV magnetometer measuring the stray field of a 2D magnet. Schematic of an all diamond scanning probe, hosting a Nitrogen-Vacancy (NV) center at the apex of the tip for magnetic stray field imaging. The NV center can be optically excited (green laser light) and read out. Due to the NV's spin dependent fluorescence the magnetic stray field of a sample (denoted with B, black arrows) can be measured. Illustration adapted from [9].

its apex is brought close to the sample surface, as illustrated in Fig. 2.2. Green laser light excites the NV center, and the resulting red fluorescence is detected. By scanning the diamond tip across the sample and measuring shifts in the NV center's spin resonance, a high-resolution magnetic stray field map is generated. The technique's non-invasive nature, combined with high spatial resolution (< 50 nm [16]) and magnetic field sensitivity on the order of $\mu\mathrm{T}/\sqrt{\mathrm{Hz}}$ [17], makes scanning NV magnetometry an excellent tool for probing magnetic properties and phenomena in 2D magnets.

In the following sections we will first describe the nature of NV centers in diamond and their ability to sense magnetic field, section 2.3.1. Afterwards, in section 2.3.2, we discuss the measurement techniques and schemes, which were used to record the magnetic stray field maps presented in this thesis.

2.3.1. Magnetic field sensing with Nitrogen-Vacancy centers

As stated above, the Nitrogen-Vacancy (NV) center in diamond is a paramagnetic defect whose spin can be optically prepared and read out, enabling the detection of local magnetic fields [68, 69]. This solid-state spin system is highly suitable for high-precision quantum sensing due to its non-perturbative nature [70, 71].

Formation and Structure: An NV center is formed when two carbon atoms in the diamond lattice are replaced by a nitrogen atom and an adjacent vacancy, as illustrated in Fig.2.3a. In magnetometry, the negatively charged NV^- center is studied. This configuration includes six electrons: five electrons from the dangling bonds of three carbon atoms and the nitrogen-vacancy pair and one additional, sixth electron captured from the lattice [72]. For simplicity, we refer to NV^- as the NV center in this thesis.

Electronic and Spin Properties: The NV center's localized electronic states feature a ground state spin $\mathrm{S} = 1$, which can be initialized and read out via optical transitions. Both the ground state (GS) and excited state (ES) of the NV center have three spin sub-levels: $\mathrm{m}_s{=}0$ and $\mathrm{m}_s{=}\pm1$, as depicted in the NV level scheme in Fig. 2.3b. The zero-field splitting of the GS (ES) is 2.87 GHz (1.42 GHz) [15], which results from spin-spin interactions.

Optical Excitation and Fluorescence: The NV spin can be optically excited with 532 nm laser light into the ES, which has a lifetime of about $\sim$ 13 ns [72]. Spin-preserving decays to the GS occur through the emission of a 637 nm photon in the zero-phonon line (ZPL) or through the emission of phonons and photons in the phonon-sideband (PSB) extending from $\sim$650 nm to $\sim$750 nm. The majority of the NV luminescence is measured in the PSB and only $\sim$ 3% of the emission is detected in the ZPL [73, 74]. For NV magnetometry the photons from the full NV emission spectra are collected, in contrast to quantum entanglement applications, which rely on indistinguishable photons from the ZPL. The non-spin-conserving decay channels are crucial for the NV spin state's readout and initialization. These decays primarily occur from the ES $\mathrm{m}_s{=}\pm1$ states via metastable singlet states with longer lifetimes than the triplet ES (142 ns at 450 K, 462 ns at 4.4 K [75]). These pathways are mostly non-radiative, leading to spin-dependent fluorescence. The $\mathrm{m}_s{=}\pm1$ states couple more strongly into the dark, long-lived metastable states, inhibiting immediate re-excitation. Since the non-radiative decays are not spin-conserving and mainly occur from the ES $\mathrm{m}_s{=}\pm1$ states, optical pumping into the $\mathrm{m}_s{=}0$ GS is possible.

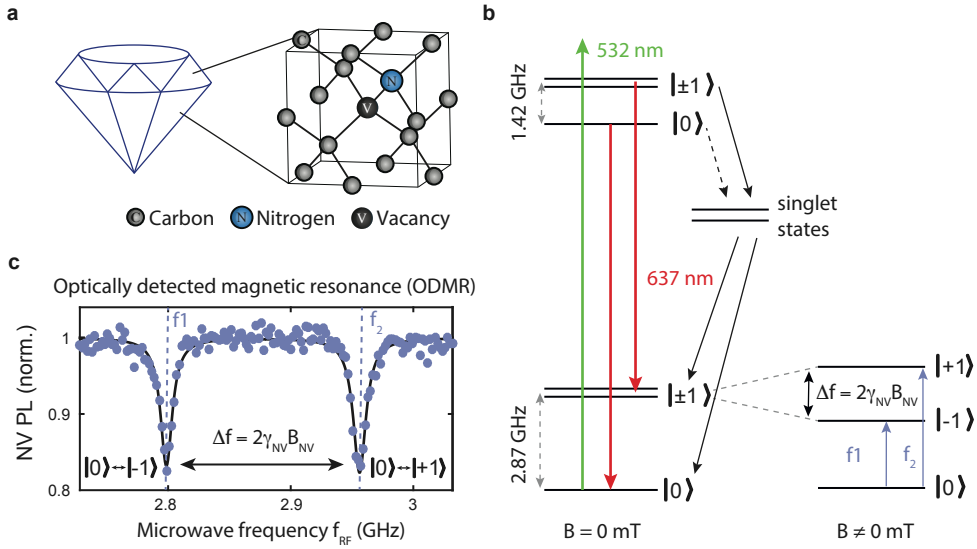

Figure 2.3.: Quantum sensor based on Nitrogen-Vacancy (NV) centers in diamond. a Illustration of an NV center in diamond, consisting of a Nitrogen atom (blue) and a Vacancy (black) within the carbon (gray) lattice of diamond. **b** Level diagram of the NV's ground state and excited state. The spin states split in the presence of an external magnetic field (depicted for the GS), which allows for optically detected magnetic resonance, **c**, where the NV photoluminescence (PL) is recorded while applying a microwave (MW) field. A reduced NV PL is measured (dips in ODMR trace) whenever the MW is on resonance with one of the NV GS spin transitions, therefore the splitting of the ODMR peaks is proportional to the local magnetic field B_{NV} projected along the NV-axis.

By illuminating the NV center with 532 nm laser light the system can thereby be initialized into the m_s=0 GS with an 80% yield [75].

Magnetic Field Sensing: A magnetic field along the NV axis (from the nitrogen to the vacancy) shifts the NV spin sub-levels due to the Zeeman effect [15]. By driving the spin transition between the GS m_s=0 and m_s=±1 levels with MW at frequencies, the magnetic field projection along the NV can be measured via optically detected magnetic resonance (ODMR), shown in Fig. 2.3c: Illuminating the NV center with above-resonance laser light and recording the photoluminescence while varying the MW frequency allows for the detection of the local magnetic field. When the MW frequency matches a spin transition from GS m_s=0 to m_s=±1 (denoted as frequency $f_{1,2}$ in Fig. 2.3), the system populates the m_s=±1 states. Via laser illumination, the system is then excited into the ES m_s=±1 states, from where relaxation back to the GS via non-radiative pathways occurs, resulting in a reduced NV fluorescence. These "dips" in photoluminescence in an ODMR measurement occur each time the MW frequency is on resonance with the NV spin transition. The splitting Δf of the two

ODMR dips is proportional[1] to the local magnetic field projected onto the NV axis B_{NV} [15]:

$$\Delta f = 2g\mu_B \cdot B_{\mathrm{NV}}, \tag{2.4}$$

with $g\mu_B = \gamma_{NV} = 28\,\mathrm{MHz\,mT^{-1}}$ being the gyromagnetic ratio. By measuring the splitting of the ODMR dips, i.e. Δf, we therefore directly determine the local magnetic field along the NV symmetry axis. For more details on the NV's response to magnetic fields, see Appendix A.1.

The NV center is a sensitive magnetic field sensor. We can determine the NV sensitivity as follows [15, 76]:

$$\eta \approx \frac{1}{\gamma_{\mathrm{NV}}} \frac{\Delta\nu}{\mathrm{C}\sqrt{\mathrm{I}_0}}, \tag{2.5}$$

where C is the optical contrast, I_0 is the NV fluorescence rate and $\Delta\nu$ is the width of the ODMR Lorentzian. In our experiments, we typically achieve a magnetic field sensitivity of several $\mu\mathrm{T}/\sqrt{\mathrm{Hz}}$, which is sufficient to image stray fields of intrinsically magnetic vdW materials with typical magnetization of a couple of μ_B per unit cell[2].

Having discussed the basic principles of NV centers for magnetic field imaging, we turn to the discussion of different measurement schemes for measuring DC[3] magnetic stray fields with NV sensors in the following section.

2.3.2. Magnetic field imaging techniques

In this section we describe the DC NV magnetometry techniques used to record the data presented in this thesis. We primarily capture magnetic field images by recording the full ODMR spectra, c.f. Fig. 2.4a, at each pixel in a 2D plane above the sample. For this the laser and microwaves are continuously on and we record the ODMR spectra of one NV transition. We extract the NV frequency (and hence the local magnetic field, c.f. eq. 2.4) by fitting the ODMR spectra at each pixel to a Lorentzian function. We can also turn to pulsed ODMR measurements, which reduces the effect of MW heating and laser illumination and prevents laser-induced line broadening effects [76]. In a pulsed ODMR sequence we first initialize the NV into the GS $\mathrm{m}_s{=}0$ by applying a green laser pulse. Afterwards, during the free evolution time, we apply a π-rotation MW pulse when on resonance with the transition. A second, subsequent laser pulse is used to optically read out the NV state and reinitializes the NV back into the GS $\mathrm{m}_s{=}0$ state. The advantage of measuring the full ODMR spectrum at each pixel is the quantitative determination of the local magnetic stray field over a large bandwidth and the robustness to systematic errors. This measurement technique, however, is very time consuming and leads to scan duration of multiple days for magnetic flakes in order of a couple of μms in size, with a rastering of $50 - 100$ nm.

An alternative, faster imaging technique is (dual) iso-magnetic field imaging ("iso-B"), where changes of magnetic field are recorded as changes in NV fluorescence. For

[1] Equation 2.4 is valid provided transverse magnetic fields can be neglected (threshold at 5 mT for transverse fields). We can neglect the effect of transverse fields in our experiments, where we apply the external field parallel to the NV axis.

[2] For more sensitive measurements the NV sensitivity can be pushed to several $\mathrm{nT}/\sqrt{\mathrm{Hz}}$ by using pulsed sequences [77].

[3] In this thesis we focus on DC magnetic field sensing only. The NV center can also detect AC magnetic fields, more details can be found in [78, 79].

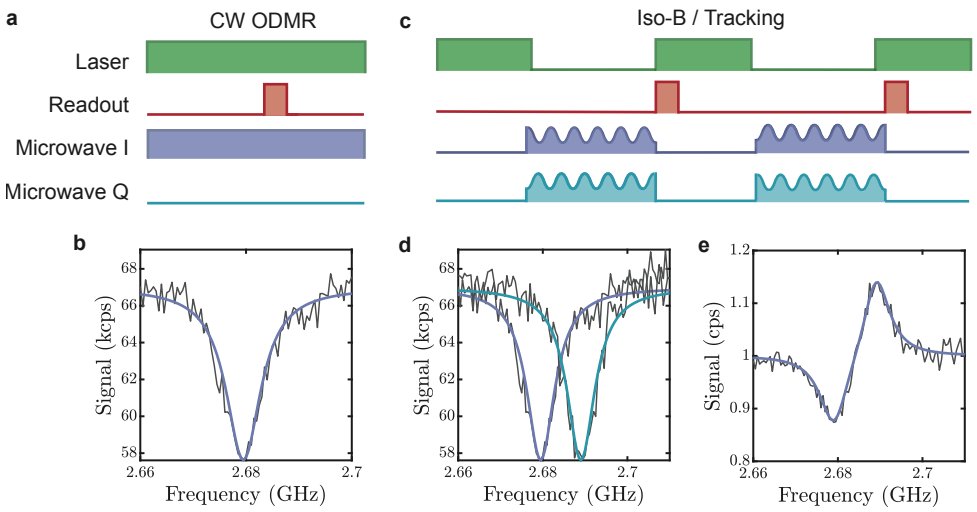

Figure 2.4.: Measurement techniques. **a** Continuous wave (CW) ODMR where the NV is excited (and initialized) using 532 nm laser light and microwaves are continuously applied. **b** Exemplary ODMR spectrum (black) with Lorentzian fit (blue) recorded by sweeping the MW frequency across the resonant NV transition. **c** Illustration of the pulse sequence used for frequency modulated tracking. An IQ-modulator is used to combine frequencies such that the applied frequency is shifted between each readout by a frequency Δf. **d** Exemplary ODMR spectra using the frequency modulation (black) with Lorentzian fits (blue and teal). **e** Normalized signal from **d**, which is used for Iso-B imaging and for frequency tracking, where a PID loop maintains a normalized signal of 1.

iso-B imaging, the applied MW field is modulated to shift the frequencies by Δf to higher and lower values. An example of such a modulated frequency sequence is shown in Fig. 2.4c. With this sequence we measure two ODMR traces, which are centered around the MW frequency $f = f_{isoB}$, as depicted in Fig. 2.4d. Normalizing the two ODMR spectra via $S = \frac{\mathrm{ODMR}_1}{\mathrm{ODMR}_2}$ yields a single spectrum as shown in Fig. 2.4e.

For a fast measurement routine (multiple hours for μms sized flakes, measured with $50 - 100$ nm pixels), we do not perform a full MW sweep but simply measure the NV fluorescence change at the modulated frequency around $f = f_{isoB}$, which we choose such that when away from the sample the magnetic signal is zero (meaning we normalize the signal $S = \frac{ODMR_1}{ODMR_2} = 1$ for $f = f_{isoB}$). Any changes in magnetic field will then introduce a frequency shift of the NV, which will be reflected in a change of the signal. While this imaging method is faster compared to the full 2D ODMR method, described above, quantitative magnetic field information can only be obtained for signal changes in the linear regime of the signal, i.e. for changes of the magnetic field which are smaller than the frequency splitting Δf. Beyond this, the magnetic field measurements are only qualitative.

Such an iso-B sequence can, however, be turned into a fully quantitative imaging mode by introducing a PID loop to lock on the zero point signal to track the central

frequency of the NV throughout the measurement (quantitatively) [80]. This tracking however, requires longer integration times per point compared to the iso-B imaging, in order to minimize effects from the PID loop lagging behind the signal.

In summary, for quantitative magnetic field imaging we either record the full ODMR spectra at each point in a 2D plane above the sample to determine the NV transition frequency and hence compute the local magnetic stray field projected on the NV axis - or we track the central frequency of a frequency modulated sequence (Fig. 2.4c-e) with a PID loop. Both methods obtain quantitative stray field maps of the magnetic sample but require multiple hours (to days) of measurement time for μms sized flakes, measured with $50-100$ nm pixels. We can switch to a faster, but qualitative imaging technique, (dual) iso-B imaging where we only differentiate between the presence (or absence) of a magnetic stray field of a set value, and where we do not quantitatively assign a value to the measured stray field at each pixel of the scan. This technique reduces the overall measurement time to a few hours per scan (for μms sized flakes, measured with $50-100$ nm pixels) and is suitable for example to image the evolution of phase boundaries as a function of applied external field, such as discussed in section 4.4.1.

Having discussed the basic principles of scanning NV magnetometry, we now turn to the practical demonstration of this technique by investigating magnetism in the 2D magnetic chromium-trihalides on the nanoscale in the following sections.

2.4. Scanning Nitrogen-Vacancy magnetometry of 2D chromium-trihalides

In this section we focus on practical examples of studying CrX_3 (X = {I, Br, Cl}) down to monolayers with single spin NV magnetometry.

The magnetic CrX_3 family has been one of the first discovered vdW magnets [6]. The crystal structure of this material class is depicted in Fig. 2.5a. The magnetic Cr atoms are bound to their respective halides in a honeycomb structure. While the crystal structure of the CrX_3 members are similar, they differ in their magnetic order, c.f. Fig. 2.5b-d [81]. All three materials exhibit FM intralayer coupling but show different interlayer coupling: CrI_3 is FM in its bulk form and AFM in the thin limit with an out-of-plane spin orientation. $CrBr_3$ is also an out-of-plane ising type FM in its bulk form and can be exfoliated into AFM or FM configurations in the thin limit [82]. In $CrCl_3$ on the other hand, the magnetic spins align within the xy-plane, making this material a candidate for observing quasi long range magnetic order in the 2D-XY phase [43].

All chromium-trihalides materials undergo structural transitions from a high temperature, monoclinic structure to a "low"-temperature rhombohedral structure in their bulk form at different temperatures of $T = 210$ K (CrI_3), $T = 420$ K ($CrBr_3$), $T = 240$ K ($CrCl_3$) [41, 81]. It has been shown that the magnetic order in the CrX_3 is stacking order dependent, i.e for CrI_3 the interlayer exchange coupling is FM if the crystal is arranged in the rhombohedral structure and AFM for the monoclinic structure [18]. This stacking order dependent magnetism can be exploited to create magnetic moiré materials: by twisting two layers of CrX_3 and thus locally altering the

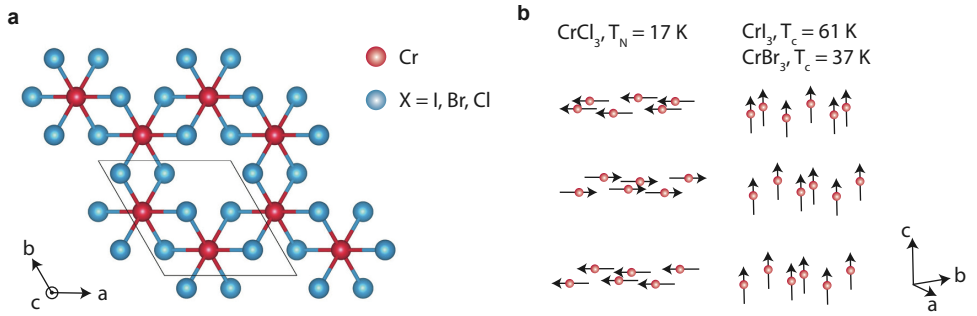

Figure 2.5.: Magnetic properties of CrX_3 ($X = \{I, Br, Cl\}$). **a** Crystal structure. Cr atom (red) bound to six halogen atoms (blue, X = I, Br, Cl) in an approximate honeycomb lattice. Black box indicates one unit cell. **b** Magnetic order in bulk CrX_3. Recreated in analogy to [81].

stacking order and therefore the magnetic coupling, it is possible to create a magnetic moiré [10].

In the following sections, we will show how scanning NV magnetometry can give insight into (stacking dependent) magnetic order in CrI_3, section 2.4.1. Afterwards, we explore the possibility of imaging magnetic moirés in $CrBr_3$ in section 2.4.2 and in $CrCl_3$ in section 2.4.3.

2.4.1. CrI_3

This section is adapted from[4]:

L. Thiel, Z. Wang, M. A. Tschudin, D. Rohner , I. Gutiérrez-Lezama, N. Ubrig, M. Gibertini, E. Giannini, A. F. Morpurgo and P. Maletinsky
"Probing magnetism in 2D materials at the nanoscale with single-spin microscopy"
Science, Vol. 364, pp. 973-976 (2019)

CrI_3 was among the first discovered vdW magnets [6]. Initial experiments on CrI_3 revealed unexpected AFM interlayer exchange coupling at low temperatures, contrary to the FM order observed in bulk crystals. In the MOKE experiments presented in [6], a net magnetization has only been observed for odd layers of CrI_3, while the signal was vanishing for even layered flakes (commonly termed as the "even-odd effect"). While MOKE is susceptible to magnetic order, it was not possible to extract quantitative evidence of the even-odd effect in CrI_3 and the spatial resolution of the optical probe is diffraction limited.

In this section, we present quantitative studies of imaging atomically thin CrI_3 on the nanoscale, using scanning NV magnetometry. To assess the interlayer exchange

[4]The data presented here has been recorded by L. Thiel and M. A. Tschudin. This work has been conducted as part of L. Thiel's PhD studies, M. A. Tschudin's Master thesis and the early stages of her PhD studies.

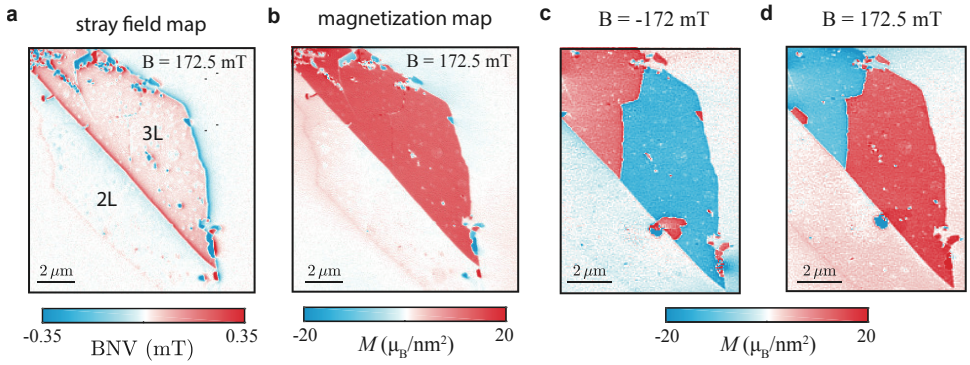

Figure 2.6.: AFM order in few-layer CrI_3. **a** Magnetic stray field map of bi- and trilayer CrI_3 recorded at $B_{ext} = 172.5$ mT with scanning NV magnetometry. **b** Corresponding magnetization map, assuming an out-of-plane magnetization direction for CrI_3, calculated with the Fourier reverse propagation method [14]. **c** Imaging two opposite magnetic configurations in trilayer CrI_3 at $B_{ext} = -172$ mT after saturating the flake in a positive field ($B_{ext,z} = 495$ mT) and conversely in **d** at $B_{ext} = 172.5$ mT after saturating the flake in a negative field ($B_{ext,z} = -495$ mT).

coupling in few-layer CrI_3 we image a bi- and trilayer flake at 4 K, which is well below the Curie temperature of CrI_3 ($T_c = 60$ K for bulk, 40 K for monolayer), as shown in Fig. 2.6a. We observe a magnetic stray field arising at the edges of the trilayer region and a vanishing signal from the bilayer part[5]. The prominent positive (negative) stray field contributions observed along the edges of the flake result from the projections of the stray field along the NV-symmetry-axis. From the magnetic stray field data, we can calculate the underlying magnetization map using the Fourier reconstruction method, described in section A.1. The resulting magnetization map is plotted in Fig. 2.6b. We find a magnetization of $13.0 \pm 2.4\,\mu_B\,/\,\mathrm{nm}^2$, which is comparable to the magnetization of one fully polarized monolayer CrI_3 sheet of $14.7\,\mu_B\,/\,\mathrm{nm}^2$ [81]. Throughout all the samples investigated (from monolayer, to max. nine layer flakes, see [14] for complete data sets), we consistently and quantitatively find AFM interlayer coupling in few-layer CrI_3.

We investigate the formation of domains in trilayer CrI_3, by imaging the flake as a function of external applied magnetic bias field. Fig. 2.6c,d show the co-existence of positively and negatively magnetized regions within the trilayer flake at nagtive (positive) external bias field. To obtain such a multidomain magnetic state, we first polarize the trilayer in a positive field along the z-axis, $B_{ext,z} = 495$ mT, and subsequently decrease the field and apply it along the NV axis. At sufficiently negative fields, parts of the flake change their magnetic orientation, as shown in Fig. 2.6c, imaged at $B_{ext} = -172$ mT along the NV axis. Similarly, when initializing the flake in a negative field along the z-axis, $B_{ext,z} = -495$ mT, and subsequently increasing the field to $B_{ext} = +172.5$ mT along the NV axis, shows the inverse magnetic

[5]The small remanent magnetic field along the bilayer edge could be due to a protruding monolayer stripe or canting of the spins in bilayer at the edges as an effect of the external bias field.

configuration, as shown in Fig. 2.6d.

It is notable that the two magnetic regions are split at the exact same location within the flake and follow a distinct line throughout the sample. The same line can be observed in the magnetic field image of the trilayer flake, c.f. Fig. 2.6a. It is therefore highly likely that defects or even local lattice disruptions split the tirlayer flake into two regions, of which one requires a lower external field to flip the spin arrangement. In this scenario, the interface of the two opposing magnetic regions is not due to the formation of a domain wall, but rather an abrupt end of a flake.

Another finding of our studies includes the effect of interlayer exchange coupling in CrI_3: we observe evidence of stacking dependent order in few-layer CrI_3 (see [14] for details). By now it has been well established, that CrI_3 indeed exhibits different magnetic interlayer coupling depending on the crystalline stacking structure [18, 45, 46]. In the next chapter, we will discuss potentials of imaging moiré magnetism based on this stacking dependent magnetic coupling.

2.4.2. $CrBr_3$

In this section we discuss the creation of magnetic moiré patterns and the possibility of imaging such domains with scanning NV magnetometry.

The stacking order dependent magnetism in CrX_3, allows for the creation of magnetic moiré structures: by twisting two magnetic layers, c.f. Fig 2.7a, spatial variations in stacking order are created. As discussed before, the magnetic order in CrX_3 compounds depends on the stacking configuration [14, 18], and therefore a modulation of AFM and FM lattice is created by introducing variations in stacking order. If the twist angle is small ($< 0.4°$), a moiré wavelength above 50 nm emerges, which can be resolved by scanning NV magnetometry [11].

In vdW twistronics, moiré stacks are usually fabricated with the "tear-and-stack" technique, where a top hBN flake picks up only half of the flake of interest, which is

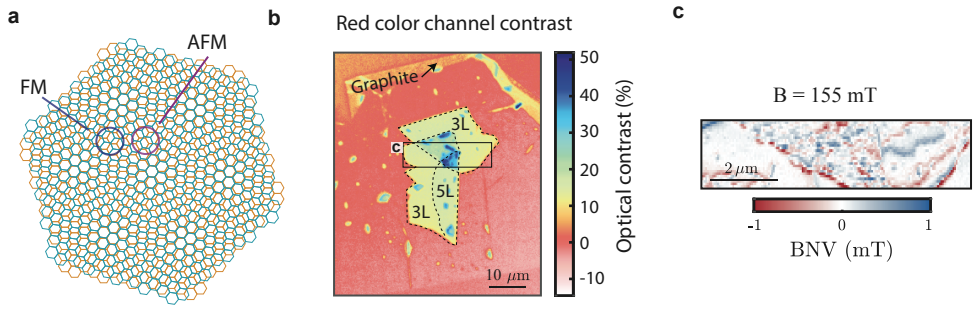

Figure 2.7.: Towards imaging magnetic moirés in twisted $CrBr_3$. **a** Twisting two layers of CrX_3 creates a magnetic moiré due to the local modulation of stacking order and the associated magnetic order. **b** Optical contrast (red color channel) of twisted $CrBr_3$ flakes (3L + 3L,5L with aligned edges, aiming for a twist angle close to 0°) encapsulated with graphite. **c** Magnetic stray field map containing the twisted region in the middle of the scan, recorded at $B_{ext} = 155$ mT.

then placed on top of the remaining second half with a twist angle of choice. The advantage of this method is the precise control over the twist angle between the two flakes, as they both originate from the same crystal orientation. The disadvantage for 2D magnets is, that the tear-and-stack method leaves an exposed edge behind, which is detrimental for air-sensitive materials. These stacks therefore require double encapsulation during the stacking procedure, which in principle can be achieved inside a glovebox by choosing appropriate stacking techniques, but during subsequent stacking the risk of introducing more contaminants into the heterostructures increases. Alternatively, it is possible to stack two magnetic flakes from the same crystal orientation (which can usually be determined from the shape of the flakes after exfoliation) with aligned edges, i.e. with 0° misalignment. In practice, the imperfection of this stacking procedure should induce a small twist angle and thus create a moiré.

In order to image magnetic moiré patterns, we investigate twisted $CrBr_3$ stacks, as shown in Fig. 2.7b. Two 3-layer flakes were stacked with aligned edges and encapsulated in thin (< 10 nm) graphite. We image the twisted area of the flake at 4 K in an external field $B_{ext} = 150$ mT, as shown in Fig. 2.7c. The twisted region shows small changes in magnetic order on a length scale smaller than 100 nm. In contrast, the non-twisted, adjacent $CrBr_3$ regions show larger domains, in the order of μms in size. While this data set is too noisy to extract a meaning full periodicity in the observed domain pattern, it does reveal an effect of different magnetic coupling in the twisted region, possibly due to the altered exchange couplings. Unfortunately, this sample was destroyed after an accidental crash with the scanning NV tip and could therefore not be studied further.

2.4.3. $CrCl_3$

In this section we discuss our efforts towards imaging a magnetic moiré pattern in $CrCl_3$. We fabricated twisted bilayer $ClCl_3$, by stacking two monolayers with the same crystallographic orientation with a twist angle of $\sim 0.1°$, as shown in Fig. 2.8a. The sample was encapsulated in graphite.

Imaging the stack at 2.3 K after zero field cooling, reveals a magnetic pattern in the twisted region, as shown in Fig. 2.8b. The data set is recorded at $B_{ext} = 150$ mT. The magnetic pattern does show a trend to exhibit a periodicity, especially within the first third of the scan region. If indeed this pattern stems from a moiré, it could be possible that due to local variations in the twist angle (due to imperfect stacking), the moiré wavelength could only be resolved in parts of the flake. However, it is difficult to confidently extract moiré parameters from this data quality and to disentangle them with the possibility of measuring magnetic structures due to random disorder within the stack.

Unfortunately, upon cooling the stack back down in a second cooldown, one week apart, the stack had degraded, as shown in Fig. 2.8d. Taking a magnetic field image of the flake at $B_{ext} = 200$ mT reveals that the material has degraded into individual magnetic puddles. Correlating the magnetic field map to the height map recorded with our scanning diamond tip, Fig 2.8e, confirms that the material has merged into local bubbles filled with magnetic material and possibly dirt and contaminants. While such bubbles can already form during stacking [83], it has also been shown that during degradation, CrX_3 merges into islands [84]. It remains to be understood, however, why

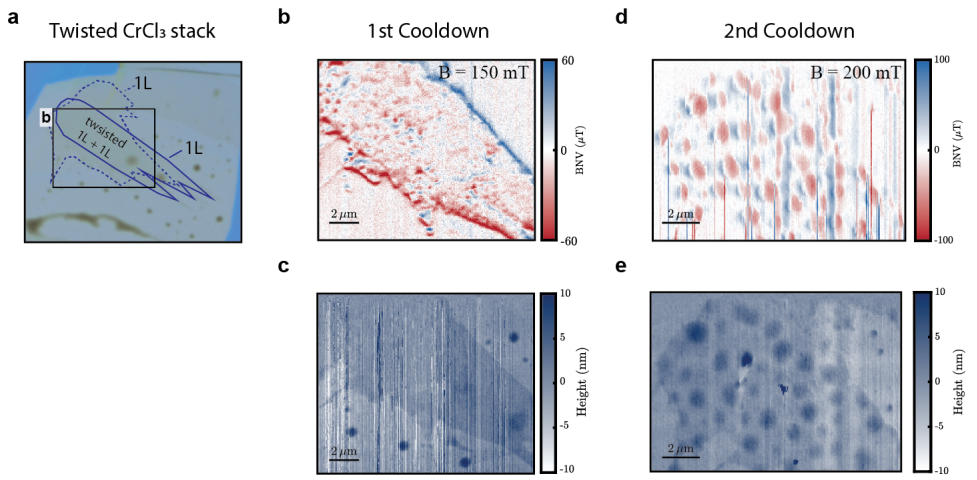

Figure 2.8.: Towards imaging moirés in twisted $CrCl_3$. **a** Optical microscope image of twisted (1L + 1L) $CrCl_3$. The blue outlines represent the two monolayer $CrCl_3$ flakes, which where exfoliated along the same crystal orientation and stacked with a twist angle of 0.1°. **b** Magnetic stray field map of the twisted region, as indicated with the black box in **a**. Field map recorded at $B_{ext} = 150$ mT. **c** Corresponding height map recorded with our scanning NV diamond pillar. **d** and **e** same as **b,c** but data recorded during a second cooldown at $B_{ext} = 200$ mT, one week apart from image **b**. The flake has degraded into magnetic puddles during the second cooldown.

these remaining magnetic bubbles, as observed in Fig. 2.8d, order almost periodically. One hypothesis is that similarly to buckling of G/hBN stacks [85], the stack degrades into periodic bubbles.

Our results on imaging magnetic order in twisted $CrCl_3$ shows the delicate interplay between magnetic moirés and structural disorder, which can be linked to the degradation of these materials. For future research, it is therefore crucial to investigate cleaner stacks with long periodicity moiré wavelengths and more air-stable 2D magnets, which are less prone to defects.

2.5. Conclusion and Outlook

In this chapter, we discussed the advantages of 2D vdW materials, particularly 2D magnets, which offer a rich platform for discovering new physics through their combination into vdW heterostructures.

To investigate magnetism in vdW materials, sensitive magnetic imaging probes are required. We showed that single spin scanning NV magnetometry is a powerful tool to quantitatively assess magnetism in 2D materials on the nanoscale. We discussed the basic principles of NV based quantum sensors for magnetic field imaging and showed their application to imaging magnetic order in the 2D magnets CrX_3 (X = {I, Br, Cl}). With our scanning magnetometer, we have quantitatively observed AFM interlayer exchange coupling in few-layer CrI_3.

The twist degree of freedom when stacking vdW materials allows for the creation of magnetic moirés. Recent work on magnetic moirés in CrI_3 have recently shown periodic patterns of AFM and FM domains in twisted trilayer CrI_3 by scanning NV magnetometry [11] and the presence of domains and fluctuations by widefield NV magnetometry [12]. However, imaging a homogeneous magnetic moiré on μms length scale and in vdW heterostructures different to CrI_3 remains to be demonstrated. Here, we presented our efforts on imaging magnetic moirés in twisted $CrBr_3$ (3L + 3L,5L) and twisted $CrCl_3$ (two twisted monolayers). While we find a correlation of local variation of the magnetization in the twist areas in both samples, our data quality is limiting the reliable extraction of a moiré periodicity and it is difficult to differentiate between the observation of local magnetic disorder and moiré physics. Furthermore, in the case of $CrCl_3$ we found the flake to degrade into periodically aligned magnetic dirt bubbles upon a second cool down. These findings highlight the delicate interplay between magnetic (dis)-order, interlayer coupling and degradation in CrX_3 compounds.

For further advances in the field of 2D vdW magnets, especially with respect to magnetic moirés, it is necessary, to discover and study more air-stable magnetic materials. While we have demonstrated that the CrX_3 family offers a large variety of interesting phenomena to study, their poor air-stability leads to an inhomogeneous magnetization, which is prone to defects. Such disorder can mask (and alter) underlying spin textures, such as moiré patterns, in these materials. Additionally, the low critical temperatures of CrX_3 (below 70 K), limit their readiness to be incorporated in applications with vdW materials.

To address these shortcomings, we will study a new, emerging 2D magnetic material, CrSBr. CrSBr shows air-stable magnetism down to monolayers and has a higher critical temperature of 140 K, which makes this material a promising platform to study magnetic spin textures in 2D. Our results on investigating nanomagnetism and AFM domain walls in CrSBr are presented in chapter 4 and chapter 5 of this thesis.

Lab tools © Gina Folly

3. Experimental Approach

In this chapter we discuss the experimental approach of fabricating 2D magnetic samples and the setup components for investigating them via low-temperature scanning NV magnetometry. We first discuss the fabrication of 2D magnetic van der Waals (vdW) samples via exfoliation of bulk crystals and a polymer based stacking technique for vdW heterostructure assembly. Since many vdW magnets are air-sensitive they require fabrication under an inert atmosphere. We will describe how 2D magnetic samples can be fabricated in a nitrogen filled glovebox, equipped with 2D stacking facilities. In the second part of this chapter, we focus on the sensing parts of our experiments: we will give an overview on the scanning NV-sensors and the cryostat components required for low-temperature scanning NV magnetometry measurements.

3.1. Van der Waals assembly of 2D magnets

The possibility to isolate and combine crystals in the thin, 2D limit opens new avenues for exploring quantum phenomena [6, 27, 86]. Assembling individual layers of 2D materials into heterostructures, however, requires dedicated fabrication techniques and environments adapted to prevent air-sensitive vdW crystals from degrading. The following two sections will discuss the basic aspects of fabricating vdW heterostructures in the lab, including their assembly under an inert glovebox atmosphere.

3.1.1. Exfoliation and stacking

VdW materials are composed of 2D sheets of covalently bound atoms, which are layered and held together by weak vdW bonds. This allows for peeling individual layers apart and reducing a vdW crystal to a single, atomic monolayer. In this section we will describe the basic principles of mechanical exfoliation, a technique used to isolate few-layer vdW flakes from their bulk counterparts via exfoliation with adhesive tape. Since the successful isolation of graphene from graphite via "scotch tape" in 2004 (Nobel Prize in Physics in 2010), mechanical exfoliation became a standard method for obtaining single, atomic layers of 2D materials [4, 87].

In order to exfoliate 2D materials, we start by placing thin bulk crystals on an adhesive tape, as shown for the example of the 2D magnet $CrCl_3$ in Fig. 3.1a. Afterwards, a clean piece of tape is lightly pressed on top of the bulk crystals and peeled off consecutively. The crystals will cleave apart, leaving vdW material on both tape stripes. This process is repeated until the two tapes are covered with thin crystal

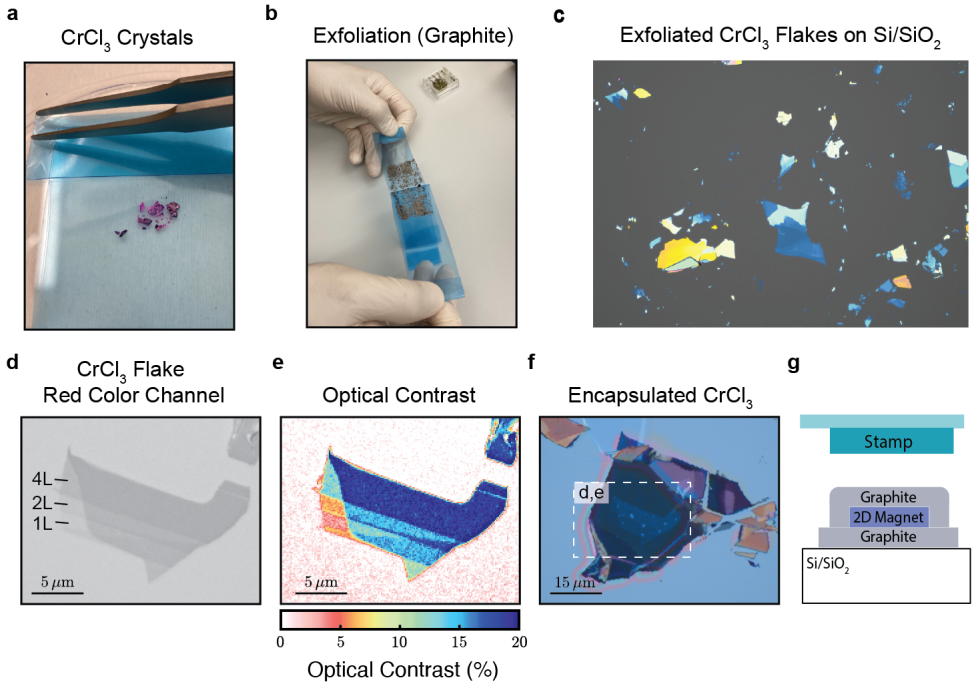

Figure 3.1.: Exfoliation and optical contrast of 2D materials. **a** Bulk crystals of the antiferromagnet $CrCl_3$. **b** Exfoliation of bulk crystals (here shown graphite) using adhesive tape. **c** Optical microscope image of exfoliated $CrCl_3$ flakes on a Si/SiO_2 substrate. **d** Red color channel contrast of a few-layer a $CrCl_3$ flake on a 90 nm Si/SiO_2 wafer. **e** Optical contrast extracted from the microscope image (red color channel) to determine the layer thickness of the flake. The contrast of $CrCl_3$ increases in increments of $\sim 3\%$ per layer in our microscope. The thinnest region of the flake is a monolayer section ($\sim 2-3\%$ contrast). **f** Microscope image of an encapsulated (in graphite) $CrCl_3$ flake. Image taken before PC removal. **g** Schematic of vdW assembly via polymer stamp based stacking.

pieces, as shown in Fig. 3.1b for graphite[1]. The tapes are then gently pressed onto a substrate of choice, most commonly a Si/SiO_2 wafer, and slowly peeled off. Thereby we obtain thin vdW flakes (typically ranging from ~ 100 nm to monolayer < 1 nm thicknesses) of various shapes and sizes, as illustrated in the optical microscope image of exfoliated $CrCl_3$ in Fig. 3.1c. The thickness of individual flakes can be determined via their optical contrast between the material and the Si/SiO_2 substrate: the interference colors of thin flakes exfoliated onto a Si/SiO_2 wafer change compared to an empty Si/SiO_2 surface [4]. This contrast is dependent on the illumination wavelength

[1] We chose to show graphite tapes to illustrate this step because most 2D magnets, such as $CrCl_3$, have to be exfoliated in an inert glovebox environment due to their air-instability, which makes it trickier to nicely capture this step on camera. The exfoliation process is identical. Note that for the chromium-trihalide exfoliation, less pressure is applied when combining the two tapes (compared to i.e. graphite) to prevent the soft crystal from breaking and shattering into small pieces.

and thickness of the SiO_2 layer [88, 89]. For 2D magnets, we typically work with ~ 90 nm thick SiO_2 layers[2], which allows distinguishing single layers, as illustrated in Fig. 3.1d for the 2D magnet $CrCl_3$ (red color channel is plotted). All the 2D magnets explored in this thesis, specifically chromium trihalides and CrSBr, have an optical absorption for visible light of around a few % per layer. For the example of $CrCl_3$, we find an optical contrast of $\sim 2-3\%$ per layer (Fig. 3.1e).

Once suitable flakes have been identified, we integrate them into 2D heterostructures via a commonly used dry-transfer assembly technique [90], where we pick up individual flakes onto a stamp and release the final stack on a substrate of choice [91]. An example of an encapsulated 2D magnetic flake, $CrCl_3$ encapsulated in graphite[3], is shown in Fig. 3.1f. A schematic of the dry-transfer is shown in Fig. 3.1g. First, we fabricate stamps for picking up vdW flakes. The stamp consists of a small piece ($\sim 2\,\mathrm{x}\,2$ mm^2) of polydimethylsiloxane (PDMS), which is placed on a glass slide and covered by a polycarbonate (PC)[4] film. This stamp is then used to pick up the first 2D flake of a stack, in our experiment this typically corresponds either graphite or hexagonal boron nitride (hBN), which acts as inert capping layer for the air-sensitive 2D magnets. By engaging the stamp on the flake at moderate temperatures ($\sim 80-100$°C), the flake can be released from the Si/SiO_2 substrate and adheres to the bottom the polymer stamp. Subsequently another vdW flake of choice, in our case 2D magnetic materials, can be picked up by engaging the stamp with the top flake on the 2D magnet. Since the stamp (glass slide, PC and PDMS) is transparent, the top flake can be aligned with respect to the target flake. By engaging the two flakes, the bottom flake will pick up onto the stack due to vdW adhesion: the vdW forces between the two interfaces are stronger than the weak interaction of the bottom flake with the rough Si/SiO_2 surface. This step can be repeated to include any desired combination of vdW layers within one heterostructure. The samples discussed in this thesis typically consist of one magnetic flake encapsulated by graphite or hBN on both sides to prevent them from degrading when exposed to ambient conditions (as illustrated in Fig. 3.1f). Once a stack is complete, it can be released on a substrate of choice by melting the PC around ~ 150°C[5]. Afterwards, the sample is soaked in cholorform or dichloromethane to dissolve the PC film.

While graphene, hBN and other air-stable materials can be stacked and processed in ambient conditions, most of the 2D magnets are air-sensitive and require processing under an inert atmosphere, such as a glovebox. In the following section we will discuss the fabrication of vdW heterostructures in an inert glovebox environment.

3.1.2. Glovebox environment for air-sensitive 2D materials

In order to handle air-sensitive 2D materials, we set up a glovebox (MBraun, Unilab Pro SP) with an inert N_2 atmosphere, as illustrated in Fig. 3.2a. The concentration

[2] We work with $001-.005$ ohm-cm 525 ± 25 μm thick SSP prime grade Si wafers with two semi-std. flats, $900\,\mathring{A}\pm5\%$ dry thermal oxide on both sides from NOVA, Electronic Materials.

[3] The optical microscope image shows the stack dropped onto a Si/SiO_2 wafer, before PC removal (hence the interference fringes along the graphite flake edges). Unfortunately this stack was destroyed during PC removal, as the top graphite layer peeled off, therefore we show the stack before PC removal.

[4] Polycarbonate dissolved in chloroform, see Appendix A.2.1 for details.

[5] See Appendix A.2.1 for details on vdW assembly parameters for stacking.

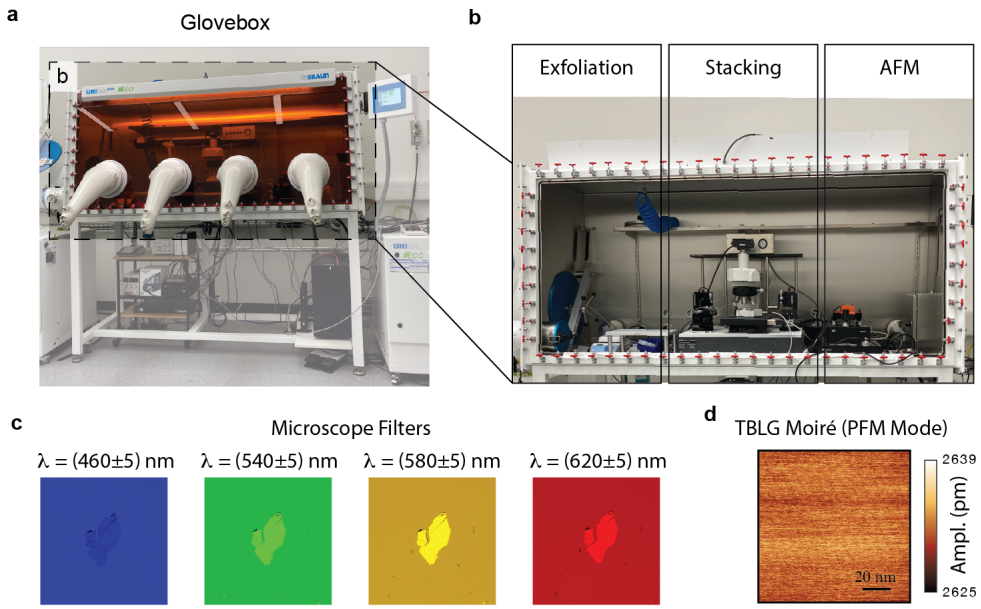

Figure 3.2.: Glovebox environment for working with air sensitive materials. **a** Glovebox providing an inert environment for working with air sensitive materials. Front panel is covered in yellow UV-filter foil to protect materials from blue light ($\lambda_{\text{filter}} \geq 520$ nm). **b** Inside of the glovebox (removed front panel) showing the three operation zones for vdW assembly: exfoliation, stacking microscope (Graphene Industries) and an AFM (NanoSurf Flex Axiom). **c** Filter options for microscope light to prevent materials from irradiation with specific wavelengths. **d** Visualization of a twisted bilayer graphene on hBN moiré pattern via PFM scanning. Sample was provided by Nanosurf and data was acquired with the Flex Axiom inside the glovebox, recorded by C. Bippes (Nanosurf) and M. Tschudin.

of water and oxygen in the box is kept below 0.1 ppm, by circulating and filtering N_2 gas. Four glove entrances allow for the manual manipulation of samples within the box. Our glovebox is connected to a second, previously installed glovebox, via a big antechamber, which allows to load bulky objects into the box or to transfer samples and/or equipment from one box to the other without exposing them to air. The box is additionally equipped with a small loadlock, which is used for bringing in all the utensils required for making vdW stacks, i.e. the 2D crystals, adhesive tape and Si/SiO_2 wafers for exfoliation and polymerstamps for stacking.

Since some 2D magnets are not only sensitive to air but also to light [92, 93], we added a yellow UV filter foil (Lithoprotect Self-Adhesive UV-Protection Yellow Foil, $\lambda = 520$ nm) to the front panel of the glovebox to filter out any UV-light components. Additionally, the microscope light is also equipped with various optical filters, which allows for blocking certain wavelengths form entering the glovebox or which can be used to optimize the optical contrast between the flake and the substrate [88]. Examples of a graphite flake illuminated with different light filters is shown in Fig. 3.2c.

Our box is divided into three different zones for vdW assembly as shown in Fig. 3.2b (picture of the opened glovebox with removed front panel). First, we installed an area for exfoliating 2D magnets inside the glovebox. The graphite or hBN flakes used for encapsulation are typically exfoliated in air and once loaded into the glovebox we heat the chips to above 100° C to bake off any contamination from the surface. After exfoliation, the vdW stacking assembly is done in a commercially available transfer microscope purchased from Graphene Industries. Stacking in the glovebox works identical to the process described in the section 3.1.1 above, with the difference that individual steps during the transfer need to be automated and controlled via external controllers outside of the glovebox. Therefore, most components of the glovebox transfer system can be controlled externally: The microscope objectives and focus, XY-stage of the sample (including rotation ability), camera settings, and transfer slide control tower can all be controlled from outside the box via joy-stick controllers. To characterize our 2D stacks, we installed an AFM (Nanosurf, Flex Axiom) in our glovebox. This allows for example for the determination of layer thickness (in addition to the optical contrast) or could be used for cleaning stacks from dirt bubbles [83] by scanning in contact-mode [94]. We are able to resolve monolayer steps within our magnetic probes (step height changes or $\sim 0.7 - 0.9$ nm). For more complex heterostructures, such as twisted devices, the AFM can be used to in-situ probe the underlying moiré structure [95], for example during device fabrication. For illustration, the moiré of twisted bilayer graphene on hBN can be visualized in Piezo-response Force Microscopy (PFM) mode with our glovebox AFM[6], as shown in Fig. 3.2d.

This section concludes the information required to understand the experimental fabrication process of the samples studied in this thesis. In the second part of this chapter, we will focus on the experimental realization of our quantum sensor and the cryogenic environment required to reach temperatures cold enough to study magnetism in vdW materials.

3.2. Scanning Nitrogen-Vacancy magnetometry at cryogenic temperatures

In order to study emergent phases of matter in condensed matter systems, often times a cryogenic environment is required to minimize thermal fluctuations which would otherwise obscure quantum effects. Especially in the scope of 2D magnetism, where many 2D magnets show critical temperatures below 200 K, low temperatures are necessary to probe magnetic signatures in these materials. To this end, we use a scanning NV magnetometry setup adapted to operate under cryogenic conditions, as discussed in the sections below. We first explain the experimental key components for realizing a scanning probe system based on NV centers in diamond and then discuss the two cryogenic setups (liquid He bath cryostat and closed-cycle He cryostat) used to achieve measurement environments in the range of a few K.

[6]Note that while recording this dataset the circulation in the glovebox had to be turned off to minimize any effect of vibrations during the AFM scan. When working with exposed 2D magnetic flakes, the imaging time should be kept minimal and ideally the circulation stays on because the materials can degrade even in glovebox environment. Further isolation of the AFM from vibrations within the box, for example by adding an enclosure, could therefore be helpful when working with 2D magnets.

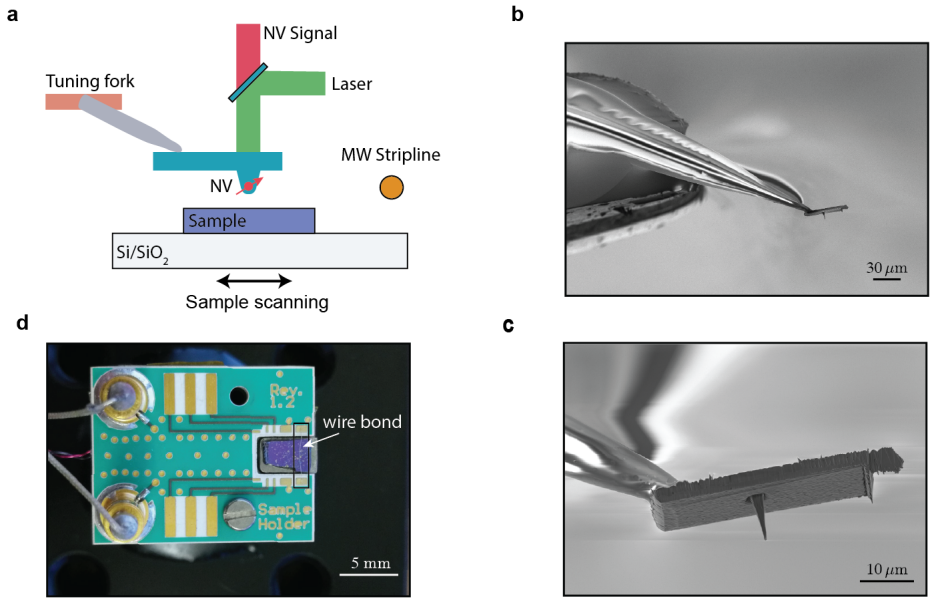

Figure 3.3.: Scanning Nitrogen-Vacancy magnetometry setup. a Schematic of a scanning NV-cantilever (blue) attached to a tuning fork (orange) via a quartz tube (gray). The magnetic sample (purple) is scanned beneath the NV center (red arrow). An optical path (free space) guides green excitation laser light to the NV center and a dichroic mirror allows for the separate detection of the emitted NV fluorescence (red). Illustration adapted from [9]. **b** Scanning electron microscope (SEM) image of a mounted NV scanning probe and **c** zoom in on the all-diamond cantilever with a nanopillar containing an NV center within the apex. Both images are shown with courtesy of J. Happacher. **d** Sample holder with integrated microwave lines. To drive the NV spin a gold wire is bonded across the sample, approximately $50-100\,\mu$m away from the 2D magnetic flake of interest.

3.2.1. Setup components

Our NV-scanning probe features an all-diamond tip with an NV center at its apex, mounted on a tuning fork for AFM-controlled scanning. The key components of a scanning NV magnetometry setup are summarized in Fig. 3.3a: a diamond scanning probe hosting an NV center at the apex of the tip (blue cantilever, red arrow NV spin), AFM control via a tuning fork allowing for close-contact scanning, optics for NV spin excitation and readout (green and red laser paths) and a MW antenna for spin manipulation of the NV center (orange circle, indicating the cross section of a wire bonded antenna). Additionally, an external magnetic field (B_{ext}) will be applied to the NV center during measurements. The following section provides an overview of these key features of our low temperature scanning NV setup, more details and references to the individual components can be found in Appendix A.2.

Tip: Our scanning probe tips consist of all diamond cantilevers, which host one or multiple NV centers a few tens of nm within the tip apex (typically ~ 20 nm for the

tips used in this thesis). The cantilever dimension a few tens of μm^2 in size and the pillars a few μm in length with a tip diameter of 200-300 nm, as shown in the scanning electron microscope (SEM) image of an all diamond cantilever in Fig. 3.3c. The tips used to record the data presented in this thesis were fabricated in house following standard diamond tip fabrication routines [96], or were purchased from Qnami, a company providing NV scanning probe tips and setups. The tip fabrication is achieved via nitrogen implantation and annealing of thin diamond membranes (creation of NV centers), e-beam lithography and diamond etching. Tip fabrication was, however, not part of this thesis and is described elsewhere in more detail [17, 96, 97]. A challenge when taking scanning NV magnetometry to cryogenic conditions is the reduced stability of NV centers: the negatively charged NV center (used for magnetometry) is less stable at low temperatures and can more easily convert to the neutral charge state. This phenomenon is not yet fully understood, but current hypothesis assume that changes in the diamond surface could lead to this instability of NV centers at low temperatures [98].

Once individual diamond cantilevers are fabricated, they are attached to a quartz capillary, which is glued on a commercially available tuning fork, as shown in Fig. 3.3b. The tuning fork AFM control allows for scanning the NV center at a fixed height above a sample.

AFM control: In order to scan our quantum sensor at a constant height above a sample and thus following its topography, we monitor the oscillation amplitude (or resonance frequency shift) of the scanning probe tuning fork. When bringing the tip into close contact to the sample surface, the tuning fork free amplitude drops (resonance frequency shifts) and a PID loop is used to maintain a fixed tip to sample distance. We typically operate at 80% of the free amplitude, which we found to be a good parameter to reduce the risk of the tip accidentally crashing into a sample surface when scanning[7]. The oscillation amplitude in height when scanning in contact are $\sim 1-2$ nm for both the liquid and the dry cryostat used for our low temperature measurements.

Optics: We use a confocal microscope setup to optically excite and read out the NV center spin state. A green laser (532 nm) is passed through an acousto-optic modulator and fiber coupled to the optical microscope head, which is mounted at the entrance of the cryostat (top loading). The laser path is free space coupled into a low temperature objective that is fixed at the bottom of the cryo stick insert and that focuses the laser onto the NV center within a diamond scanning probe. The emitted NV photoluminescence (PL) is collected through the same path and separated from the excitation light by an dichroic filter and recorded with an avalanche photo diode (APD). In our experiments we work close to the saturation power of the NV center, which is on the order of tens of microwatts for our scanning probes [97] (typically $50-100$ μW in our experiments). For all 2D magnets mentioned in this thesis, this laser power does not have a measurable effect on the measured net magnetization [14]. However, for metastable states in the 2D magnet CrSBr discussed in sections 4.4.3

[7]Such uncontrolled tip-sample interactions during AFM control happen rarely. In singular cases this can lead to interesting discoveries, as shown for our results on switching the interlayer exchange from AFM to FM in the 2D magnet CrI_3 upon puncturing the sample [14], but generally either the tip or the sample get damaged when uncontrollably crashing the tip, hence we operate at moderate tuning fork amplitude setpoints to reduce the risk of crashes.

and 5.2.2, we cannot rule out some influence of laser light affecting magnetic ordering at interfaces.

Microwave control: The MW control for spin manipulation of the NV center is achieved by applying MWs through a wire bond, which we bond across our samples. The two low temperature cryostats, which we used to conduct our measurements presented in this thesis, have inbuilt MW lines, which we couple to our sample holders. We mount our samples on printed circuit boards (PCB) and wire bond a gold (or aluminum) wire across, in $50 - 100$ μm distance to the NV center. Fig. 3.3d shows an example of a mounted Si/SiO_2 chip covered with 2D magnetic flakes and a MW antenna bonded across the chip. The samples are fixed with vacuum grease to the PCB, which will freeze upon cooldown and act as a glue. We use a small amount of silver paint to additionally glue the chip down on the PCB. The sample chip has to be properly fixed on the PCB holder to avoid detaching, shifting or lifting off during cooldown. The MW applied during our experiment can lead to local heating by a few degrees (measured via resistive temperature readout below the sample plate), as mentioned in section 4.5.2. Such MW heating is negligible when operating well below the transition temperature of most 2D magnets, but has a noticeable impact when studying materials such as $CrCl_3$, with a Néel temperature of only a few degrees above the base temperature of our cryostats.

External magnetic field B_{ext}: For quantitative magnetometry with NV centers the external magnetic field, B_{ext}, has to be applied along the NV axis [78]. Orthogonal fields will reduce the optical contrast of the NV due to spin mixing and thus only allow for measurements in fields of a few tens of mT [99]. The NV axis is defined by the crystal structure of the diamond host material. In our experiments we mostly work with NVs oriented along the $\langle 100 \rangle$ axis of diamond, resulting in an angle $\theta_{\text{NV}} = 54.7°$ away from the sample normal. Other orientations of NV centers exist as well, such as $\langle 111 \rangle$ tips with out-of-plane oriented NVs [100] and $\langle 110 \rangle$ tips with in-plane oriented NVs [101] (in-plane tips from Qnami were used for two data sets in this thesis, c.f. section 5.2.3). The accessible magnetic field range for low temperature magnetometry is further affected by NV excited state level anti-crossings and by the maximum MW frequency, which can be applied to drive the NV spin. The excited state anti-crossings lead to decreased NV contrast at certain magnetic fields as a function of local strain at the NV center [102]. Most importantly, this affects the NV operation quality as a function of temperature, where performance is worst in the regime of 20-60 K [103]. This, however, does not limit our measurements since we either operate below (at 2-4 K) or above (120-150 K) for the measurements presented in this thesis. In our setups we can apply MWs up to a few GHz (around 6 GHz) to the NV center, which currently limits us to operations in external fields up to ~ 300 mT along the NV axis.

Having discussed all the key components of a scanning NV magnetometry setup in this section, we will turn to the discussion of low temperature cryostat environments in the following section.

3.2.2. Cryogenic environment

In order to perform NV magnetometry measurements at low temperatures, we operate two different cryogenic systems: a liquid He bath cryostat with a base temperature of 4.2 K (AttoLiquid1000, described in [17]) and a closed-cycle dry cryostat with a

base temperature of 1.8 K (AttoDRY 2200), as illustrated in Fig. 3.4a. Both cryos are equipped with a vector magnet (liquid: 0.5 T, dry: 1 T), which allows for aligning the external magnetic field along the NV axis in our experiments. We use an optical microscope head (liquid: home build, dry: attocube) to send green excitation laser light down the microscope stick (free space) and collect the red NV fluorescence through the same path and guide it to an APD - see the representative schematic of the microscope insert in Fig. 3.4a. More details on the optical paths and the corresponding components are described in the previous section under "Optics" and summarized in Appendix A.2.2. Control over the position of the sample and the tip are achieved with two separate piezo stacks mounted at the bottom of the microscope stick, as depicted in Fig. 3.4b. These consist of coarse XYZ-positioners and XYZ-scanners. Our maximal scan range is $\sim 15\,\mathrm{x}\,15\ \mu\mathrm{m}^2$ at base temperature.

While the NV microscope part for the two cryogenic systems is very similar, the operation regimes vary a lot. The liquid bath cryostat is a very stable system, not prone to clogging but requires refilling of He every 5-6 days, which periodically interrupts ongoing measurements and thus prevents long, consecutive measurement times. Variable temperature measurements via locally heating the sample chip can be achieved in the range of 4-20 K, but the system is limited to measurements in this low-temperature regime as above 20 K the He boil-off prevents stable in contact

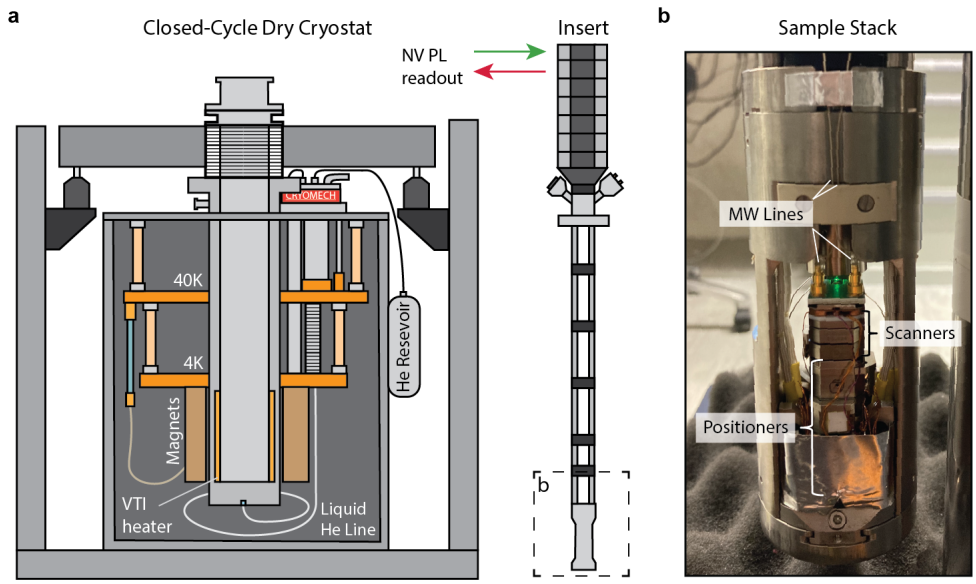

Figure 3.4.: Cryostat for scanning NV magnetometry measurements. a Schematic of a closed-cycle He cryostat (AttoDRY2200) with a base temperature of $\sim$ 1.8 K and variable temperature control (1.8-300 K). Sample stick insert with microscope head is depicted on the right. The sample and tip stacks are located at the bottom of the insert (outlined with a dashed box). **b** Image of the sample stack consisting of coarse positioners (XYZ), scanners (XYZ) and the sample holder with microwave line connections (to drive the NV spin for sensing).

scanning of the AFM. In contrast, the dry, closed-cycle cryostat can, in principle, operate at base temperature for several months[8] and allows for variable temperature control from 1.8-300 K.

The cooling mechanism of the closed-cycled cryo is based on two different He gas circuits. The primary circuit cools down a 40 K and a 4 K stage in the cryostat based on periodic compression and displacement of He gas in pulse tubes (c.f. cryo schematic in Fig. 3.4a). The secondary circuit moves He gas through a cold trap and condenses the He into a liquid He reservoir. Afterwards, the liquid He is pumped through a thin, stainless steel tube at the bottom of the cryostat, where it evaporates through a needle valve into the VTI chamber and hence cooling the VTI space down to sub 2 K. The He is then pumped back into the condenser line, to keep the circuit closed. In order to cool down the sample we use He exchange gas for thermal contact between the VTI space and the sample chamber. The VTI space is equipped with local heaters, which allows for variable temperature measurements from $\sim$ 2 K to 300 K. The low vibration when scanning in contact is achieved by isolating the microscope stick from the cold plates (i.e. pulse tubes) via free suspension of the stick within the sample tube.

3.3. Conclusion and Outlook

In this chapter we have shown the basic principles of vdW heterostructure assembly in an inert glovebox environment. While encapsulating air-sensitive 2D magnets in protective layers (such as graphite or hBN) prevents them from degrading[9] and thus allows for studying their magnetic properties, these samples do come with certain drawbacks. First, during the stacking process - even in an inert glovebox environment - contamination from the environment, such as polymer residues or hydrocarbons, can be trapped into pockets between the individual layers of a vdW heterostructure [83, 104]. Such dirt bubbles will locally distort the stack structure and can apply pressure and/or strain to the device. There are different ways of cleaning stacks form such contamination pockets, some of which include annealing the stack at high temperature, pushing the bubbles out via contact mode AFM or stacking at very high temperatures [94, 105]. While the AFM cleaning can in principle be performed on 2D magnetic stacks, the annealing and high temperature stacking are not an option since many of the 2D magnets will degrade if exposed to high temperatures (especially when not fully encapsulated). For future advances in the field it is therefore crucial to engineer and study more air-stable 2D magnets, such as for example the compound CrSBr, which will be discussed in the following two chapters. Another interesting route is the fabrication of vdW stacks in ultra-high vacuum, where contaminants from the environment are being reduced to a minimum [106].

On the sensor side, we have shown in this chapter how single NV centers can be incorporated into a scanning magnetometer compatible with operations in a cryogenic environment. For a more versatile scanning setup it would be beneficial to add the

[8] At the time of writing, however, the system is very prone to clogging, thus limiting the measurement time at base temperature to maximum a few weeks.

[9] In principle, a perfect encapsulation preserves the magnetic properties of air-sensitive materials. In practice, however, encapsulations can sometimes show folds and defects, which can then lead to degradation of the stacks.

option of twist and rotation functionalities of the sample: since many 2D magnets have specific magnetocrystalline anisotropy axes along which an external field (and hence the NV center) needs to be aligned, having an option of in-situ rotation of the sample with respect to the NV axis would allow for exploring various anisotropy directions with a single NV center within one cooldown.

For more long term perspectives, there is great effort in the field of NV magnetometry to push the spatial resolution to sub ten nm by implanting shallow NVs in the apex of a scanning tip. The challenge here is to stabilize the NV center into its negative charge state. Current efforts include surface treatment of the diamond structures [107].

While temperatures of a few K are typically low enough to study intrinsic magnetism in 2D vdW magnets, there are plenty magnetic phases in condensed matter physics, such as orbital ferromagnetism in twisted bilayer graphene [33, 108], which are most pronounced in sub K temperature ranges. To study these phenomena, scanning magnetometry can be adapted for mK temperatures, where precise MW heat control and NV stabilization become even more crucial. Proposed approaches for quantum sensing at mK temperatures include designing on-tip MW delivery lines or using MW-free, all optical sensing schemes with other vacancy centers, such as SiVs [109].

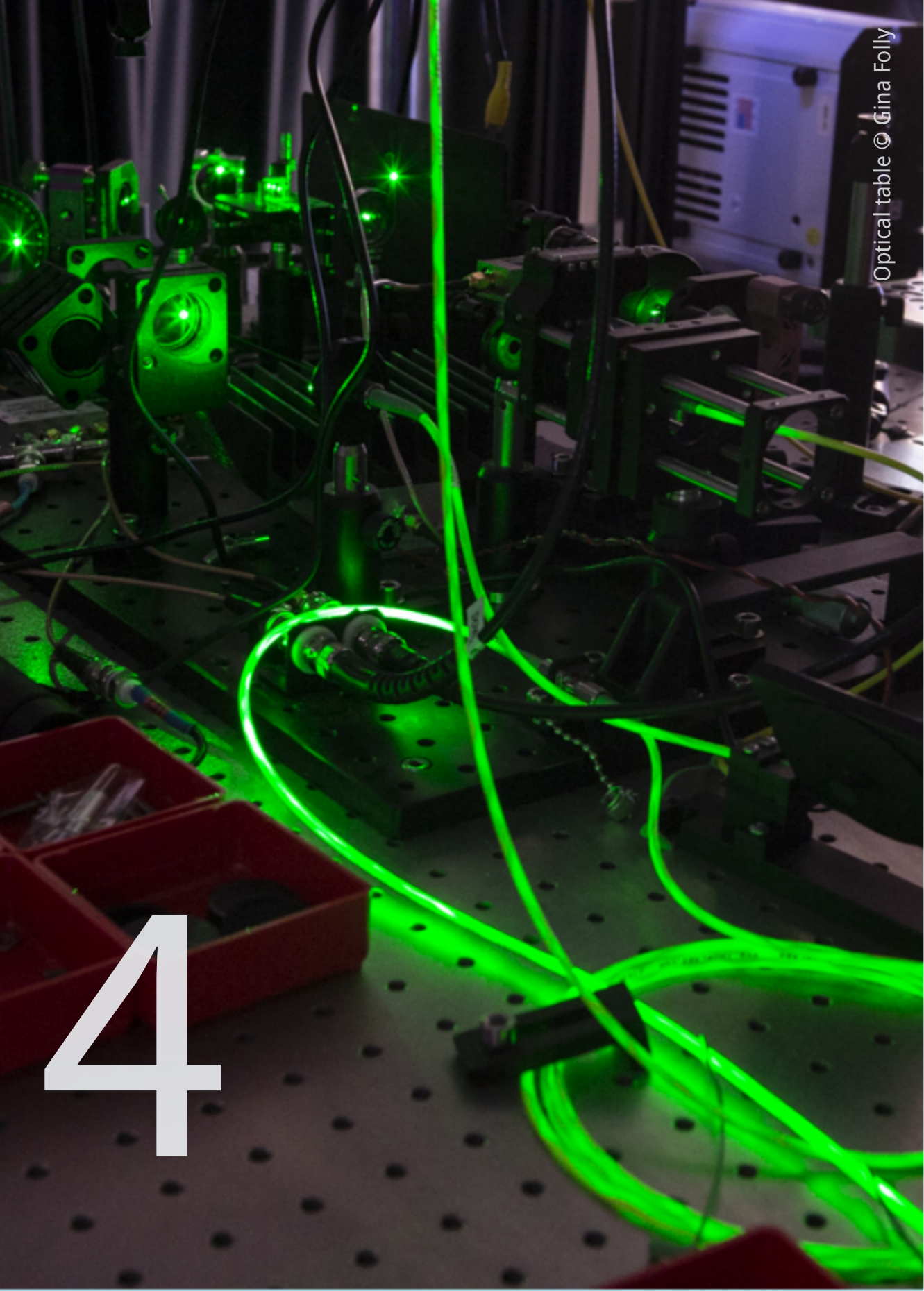

Optical table © Gina Folly

4

4. Nanomagnetism of CrSBr

Adapted from:

M. A. Tschudin*, D. A. Broadway*, P. Reiser, C. Schrader, E. J. Telford, B. Gross, J. Cox, A. E. E. Dubois, D. G. Chica, R. Rama-Eiro, E. J. G. Sanots, M. Poggio, M. E. Ziebel, C. R. Dean, X. Roy, P. Maletinsky
"Imaging nanomagnetism and magnetic phase transitions in atomically thin CrSBr"
Nature Communications, Vol. 15, pp. 6005 (2024)

4.1. Introduction

The first experimental discovery of 2D magnets in 2017 [6, 7] has created a significant interest in the scientific community. Many different applications in spintronics, quantum computing, and magnetic data storage have been suggested based on 2D magnetic materials ever since [51, 110, 111]. However, in order to advance current research to application ready tools, the community has been striving to find 2D magnets, which are more air-stable and have a higher critical temperature than the extremely fragile compounds such as CrI_3 ($T_c = 45$ K), which where among the first generation of 2D magnets that were discovered (see section 2.2).

Recently, a new 2D magnetic material has sparked wide interest in the field: the van der Waals (vdW) magnet CrSBr [53]. This material can readily be exfoliated down to monolayer, has a critical temperature above liquid nitrogen temperature ($T_N \sim 132$ K) and has demonstrated air stability down to few-layer stacks. CrSBr has attracted a lot of interest due to its unusual transport properties [112], an intriguing interplay between magnetic and optical properties [113], and a remarkable tunability of its magnetism by strain [38]. In order to fully exhaust the potential of CrSBr, however, it is crucial to understand its fundamental magnetic properties, which, to date, have not been studied with nanoscale resolution down to monolayer flakes.

In this chapter, we image the 2D magnet CrSBr down to monolayer flakes with a scanning NV magnetometer. Our imaging method allows for nanoscale insight into CrSBr's magnetic behavior at temperatures ranging form 2 K to 150 K. We study the spin-flip process in bilayer CrSBr and investigate anisotropy and magnetic ordering in the high temperature regime. Our results will help enable the engineering of novel electronic and magnetic phases in CrSBr and thus advance the realization of next generation nanomagnetic devices based on vdW materials.

4.2. The 2D magnet CrSBr

CrSBr is a vdW magnetic semiconductor (band gap ∼1.5eV [53]) with a Néel temperature of 132 K (∼ 140 K for thin flakes[1]) [114]. While the bulk material has already been studied in the 1990's [115, 116], CrSBr has recently gained significant attention in the scope of its vdW characteristics and the possibility of studying the 2D limit.

CrSBr can easily be exfoliated down to individual monolayers. The material preferentially cleaves into rectangular shapes, as shown in Fig. 4.1a. The magnetization in CrSBr, orientates along the easy-axis, *b*-axis, of the material, which corresponds to the short axis of the rectangle. Figure 4.1b illustrates the crystallographic structure of CrSBr, highlighting the magnetic easy-axis of the material (*b*-axis), the intermediate- (*a*-axis) and the magnetic hard-axis (*c*-axis). The uniaxial magnetic anisotropy, which aligns the spins along the *b*-axis of CrSBr, results from anisotropic exchange interactions [117].

CrSBr is an A-type antiferromagnet, which means that the magnetic moments within a plane order ferromagnetically and the coupling across two layers is opposite, i.e. antiferromagentic [53], as illustrated in Fig. 4.1b. The ferromagnetic interlayer coupling is caused by super exchange interaction between the Cr-S-Cr and Cr-Br-Cr paths: according to the Goodenough-Kanamori rules [118, 119], ferromagnetic alignment is dominating for bond angles of ∼ 90°, resulting in an overall ferromagnetic

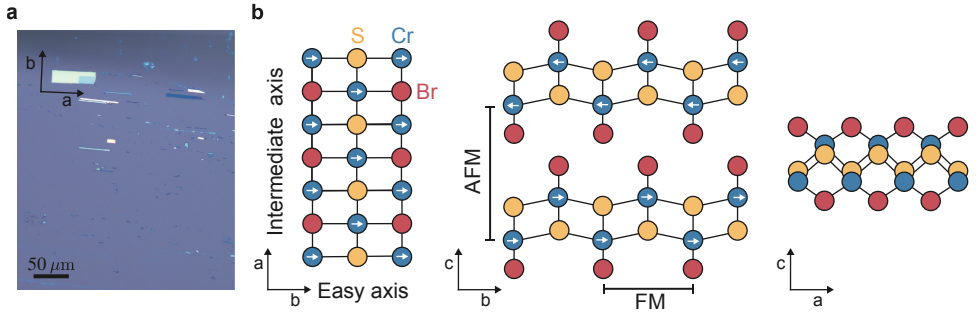

Figure 4.1.: The van der Waals magnet CrSBr a Optical microscope image of exfoliated CrSBr flakes showing the preferred cleaving direction of the material along the geometrical long axis, *a*-axis, of the material. **b** Crystallographic structure of CrSBr, where the magnetic easy axis is aligned with the *b*-axis of the crystal. The intermediate (strong) axis is aligned with the a(c)-axis of the material, and the magnetic coupling between two layers is antiferromagnetic and ferromagnetic within each of the layers.

[1]The interpretation of an increase in critical temperature for decreasing layer thickness in CrSBr results from the presence of an intermediate ferromagnetic state, *iFM*, where the stronger FM intralayer coupling persists but spin waves along the *c*-axis can disturb the weaker AFM interlayer coupling. Thinning down the system confines spin wave excitations along the *c*-axis, which in turn stabilizes the AFM interlayer order or in other words, the corresponding T_N interlayer approaches the higher T_c intralayer. [114]

intralayer coupling in CrSBr [2] [117, 120].

By applying external magnetic fields along the intermediate (hard axis) of CrSBr, the spins will start to cant away from the b-axis until saturating at fields of ~ 1 T (~ 2 T), along the a-axis (c-axis) at 2 K [121]. For bilayer or thicker structures, CrSBr will undergo a spin-flip transition (where spins align from AFM to FM), induced by applying magnetic fields along the b-axis. The external field required for such a spin-flip is around ~ 0.2 T for bilayer and ~ 0.6 T for bulk CrSBr [121].

The magnetization of a fully polarized monolayer CrSBr sheet is around 36 μ_B/nm^2, as each Cr atom contributes 3 μ_B and one unit cell contains two Cr atoms (lattice parameters $a = 3.5$Å, $b = 4.7$Å, $c = 7.9$Å) [117]:

$$M = \frac{2 * 3\,\mu_B}{0.35\text{nm} * 0.47\text{nm}} \approx 36\mu_B/\text{nm}^2. \tag{4.1}$$

Magnetic signals from CrSBr arise when cooling the material below its critical temperature: While AFM interlayer order forms below the Néel temperature of 132 K ($\sim$ 140 K for thin flakes) in CrSBr [114], the Curie temperature for the FM intralayer order is slightly higher, around 150 K [121]. There have been multiple studies suggesting a so-called *intermediate FM phase* emerging at temperatures between $T_\text{N} < T < T_\text{c}$ [114, 117], where FM intralayer ordering persists while AFM intralayer coupling vanishes. However, the origin of such a high temperature phase and its magnetic characteristic yet remain to be explored.

Whereas multiple studies have been done on characterizing the triaxial magnetic anisotropy in CrSBr [53], measuring magnetoresistance properties of CrSBr down to single layers [121, 122] and studying magnetic properties of thin CrSBr flakes on the microscale [30, 123], little is yet known about the magnetism of thin (< 5 layers, down to monolayer) CrSBr on the nanoscale. It remains an open question, for example, if the spin-flip in bilayer CrSBr occurs as a uniform rotation of all the spins within a layer, or if it is mediated by domain formations. Furthermore, no local imaging probe has yet explored the *intermediate FM phase* of CrSBr at elevated temperatures ($T_\text{N} < T < T_\text{c}$).

In the following sections, we will discuss nanoscale magnetization properties of few layer (< 5 layers) CrSBr flakes down to monolayers. The results are obtained by single spin scanning NV magnetometry measurements. We will discuss magnetic imaging of the AFM/FM spin-flip transition in bilayer CrSBr and study anisotropy and magnetic correlations in the high temperature regime.

4.3. Imaging magnetization of few layer CrSBr on the nanoscale

In order to study the magnetic properties of CrSBr on the nanoscale, we investigate various different CrSBr samples, as summarized in table 4.1. All the samples have been fabricated by our collaborators at Columbia University from the groups of Prof. Xavier Roy and Prof. Cory Dean.

[2] The bond along the Cr-S(Br)-Cr paths along the a-axis is $\sim 95°$ ($90°$). The Cr-S-Cr path between two Cr layers connect via $\sim 96°$ and the Cr-S-Cr path along the b-axis with $\sim 160°$. [117]

Sample #	Label	# of Layers	Encapsulated
1	$S1_{\mathrm{Air}}$	2, 3, 5	No
2	$S2_{\mathrm{Encap}}$	1, 2, 3	Yes
3	$S3_{\mathrm{Air}}$	1, 2, 4, 5	No
4	$S4_{\mathrm{Air}}$	1, 2	No

Table 4.1.: Description of samples used in this study.

The samples contain different layer thicknesses of CrSBr, ranging from monolayer to five layers. Figure 4.2 shows an overview of all four samples studied in this chapter. Samples $S1_{\mathrm{Air}}$, $S3_{\mathrm{Air}}$ and $S4_{\mathrm{Air}}$ were not encapsulated and were exposed to air for several hours to days before measurements. Sample $S2_{\mathrm{Encap}}$ was encapsulated with

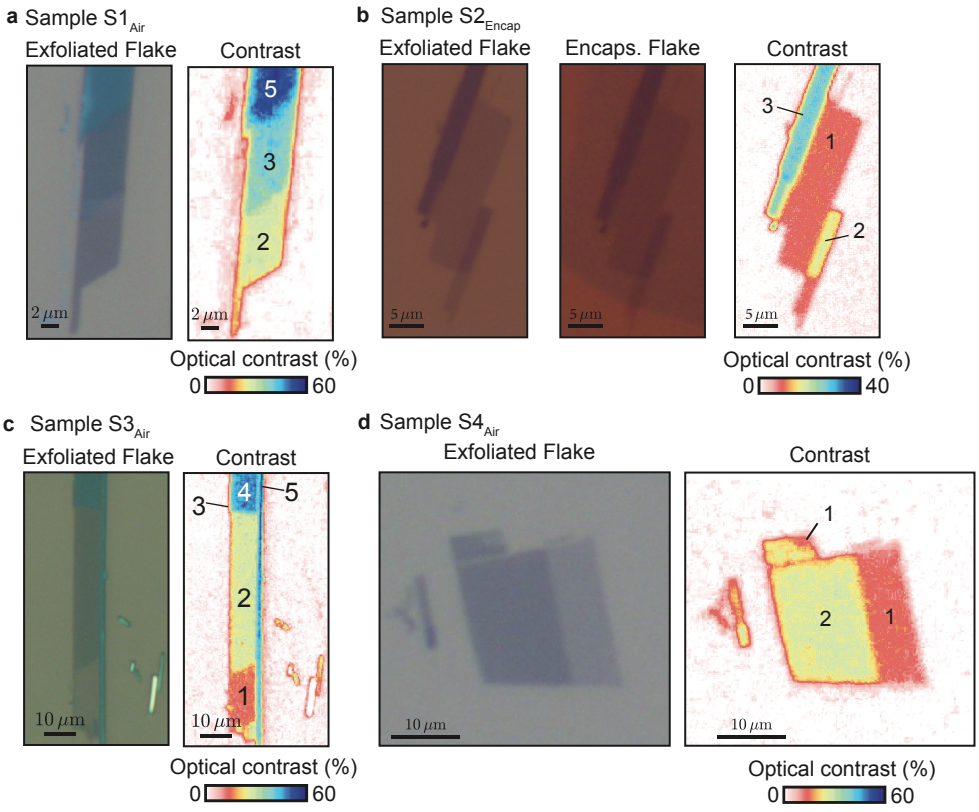

Figure 4.2.: Optical sample characterization of the CrSBr flakes. Panels **a** to **d** show the optical microscope images of samples $S1_{\mathrm{Air}}$ to $S4_{\mathrm{Air}}$ and the extracted optical contrast used to determine the layer thicknesses. For the sample $S2_{\mathrm{Encap}}$ the encapsulated flake is depicted as well in panel **b**.

hBN and served as a reference sample to examine the air stability of few layer CrSBr. The thickness of individual CrSBr flakes was determined by measuring the optical contrast between the flakes and the Si/SiO_2 substrate: as shown in Figure 4.2, the optical contrast for flakes thinner than five layers can easily be distinguished and serves as a good reference. A single layer of this material has an absorption of approximately 15% in our optical microscope. The absorption per layer scales linearly for thin layers (≤ 3) but reduces for thicker layers (≥ 5). More precise methods such as AFM measurements or magnetic characterization will additionally confirm a certain layer thickness.

In the next section we will present nanoscale magnetization studies of each sample obtained by single spin scanning NV magnetometry (c.f section 2.3).

4.3.1. Magnetization of CrSBr

We employ our single-spin scanning magnetometer based on an individual NV center in diamond (see Sec. 2.3.1) – a nanoscale imaging technique that is non-invasive and sensitive enough to image magnetism in vdW monolayers [14] – to explore magnetic order in CrSBr in a quantitative way.

The NV spin is situated at the tip of an atomic force microscope and scanned across the CrSBr flakes to quantitatively image magnetic stray fields generated by the CrSBr flakes. The NV thereby enables a quantitative determination of B_{NV} [78]– the projection of the total magnetic field onto the NV axis – which in turn allows us to determine CrSBr's sample magnetization down to the monolayer limit, see Sec. 2.3.1 for more technical details. Due to the AFM interlayer coupling the two-dimensional CrSBr flakes should only exhibit a magnetic stray field for odd number of layers.

We start by investigating few-layer CrSBr samples at $T \approx 4$ K and at low magnetic fields ($B \approx 5$ mT), where the CrSBr layers exhibit AFM interlayer alignment [53]. The recorded magnetic stray field map of a bilayer/trilayer CrSBr, sample $S1_{\mathrm{Air}}$, is shown in Fig.4.3a. The sample was first zero field cooled and subsequently measured at a temperature of around 4 K, which is well below the Néel temperature of CrSBr. The external magnetic field was applied along the NV axis (with $\theta_{\mathrm{NV}} = 53°$ tilted away from the c-axis), with the in-plane component approximately aligned along the b-axis of the CrSBr flake, as indicated by a black arrow in Fig.4.3a. The trilayer section exhibits a stray field only at the edges, which is expected for uniformly magnetized samples [124], whereas the bilayer shows no detectable magnetic stay field. This observation is in agreement with the expected antiferromagnetic interlayer coupling in few layer CrSBr, where, as a result only the trilayer section is expected to show a non-zero magnetic stray field.

The magnetic stray field map (Fig.4.3a) shows no defects within our spatial resolution, which is determined by the NV to sample distance and approximately ~ 50 nm for all the data shown in this chapter. The homogeneous magnetic nature of sample $S1_{\mathrm{Air}}$ is even more apparent in the magnetization map obtained via magnetization reversal (see section A.1 for details on reverse propagation), as shown in Fig. 4.3b. The magnetization value obtained for the trilayer is 36 ± 0.2 μ_B/nm^2, which is close to the expected value of 36 μ_B/nm^2 per fully saturated layer of CrSBr. In order to independently determine the magnetization of the trilayer flake, we took a linecut of the magnetic stray field, shown in Fig. 4.3c. Analytic fits to the stray field profile

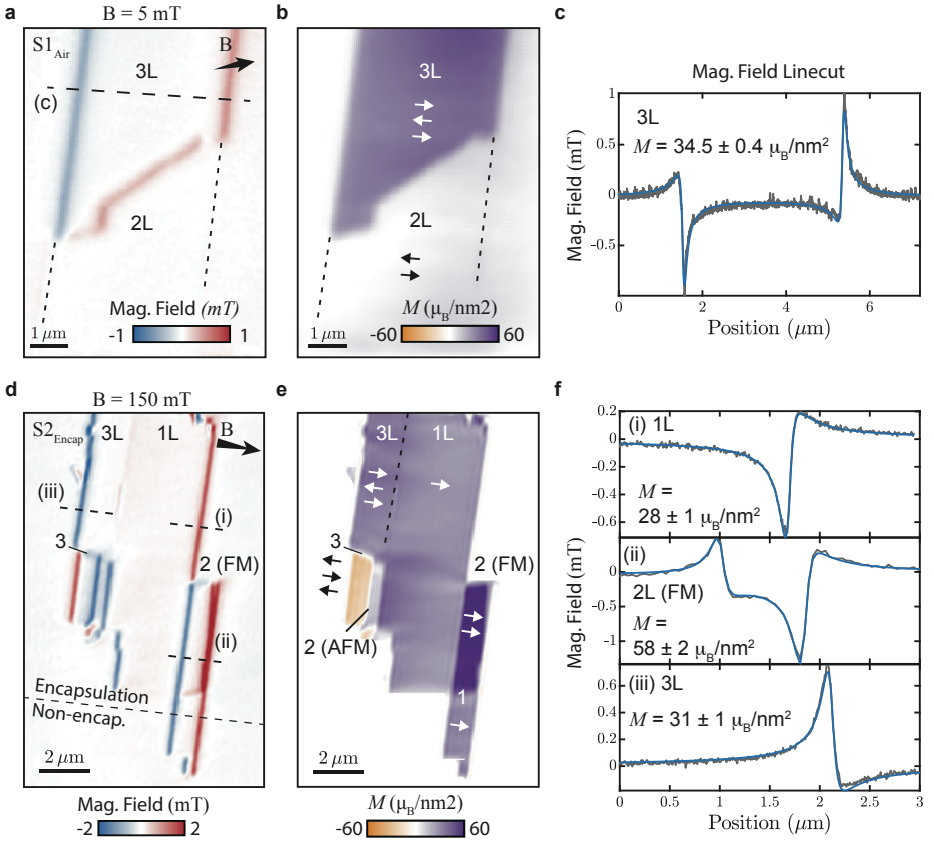

Figure 4.3.: Magnetization characterization of few layer CrSBr. **a** Magnetic stray field image of a non-encapsulated bilayer and trilayer flake (Sample 1, $S1_{\mathrm{Air}}$), obtained in a low bias magnetic field $|B_{\mathrm{ext}}| = 5$ mT. **b** Corresponding magnetization image showing antiferromagnetic coupling of the individual CrSBr layers (indicated by white/black arrows). **c** Magnetic stray field linecut through the trilayer section of sample $S1_{\mathrm{Air}}$, as indicated by dashed arrow in panel **a**. The extracted magnetization from a fitting routine described in section A.1 is around $34.5\ \mu_B/\mathrm{nm}^2$ **d** Magnetic stray field image of an encapsulated multi-layer flake (Sample 2, $S2_{\mathrm{Encap}}$), obtained in a bias magnetic field $|B_{\mathrm{ext}}| = 150$ mT strong enough to induce FM ordering in some bilayer sections. **e** Corresponding magnetization map obtained from the stray field data. **f** Linecuts of the magnetic stray field through 1L, FM coupled 2L and 3L as measured at locations indicated with dashed lines in **d**.

(compare section A.1 for details on the fitting routine), allow for extracting the sample's magnetization. We find a value of $M \sim 34.5 \pm 0.4\ \mu_B/\mathrm{nm}^2$, which is comparable to the result from the magnetization reversal.

Similarly, we examined an encapsulated CrSBr flake, sample $S2_{\mathrm{Encap}}$, which is shown in Fig. 4.3d-f. As with the previous sample, the flake was zero field cooled and subsequently measured around 4 K. We applied an external field of $B \approx 150$ mT along

the NV axis ($\theta_{\mathrm{NV}} = 53°$ tilted away from the c-axis), with the in-plane component approximately aligned along the b-axis of the CrSBr flake. As a consequence, we have a field component of several tens of mT out-of-plane, which we consider having a negligible effect on the magnetization orientation, as the field required to cant spins along the c-axis (out of plane) is very high $\sim$ 2 T [122].

We observe stray fields arising from the edges of all the different regions, 1L, 2L and 3L, of the flakes, see Fig. 4.3d. To address the question of why the bilayer section of this particular flake is magnetic, it is helpful to study the magnetization map (Fig. 4.3e) of sample $S2_{\mathrm{Encap}}$. This shows an increased magnetization in the bilayer section of roughly twice a monolayer magnetization. We thus conclude that the external field was strong enough to induce ferromagnetic alignment in the bilayer. As we will discuss later on in section 4.4, most CrSBr bilayer flakes require a slightly higher external field to induce FM order (B $\sim$ 200 mT). This discrepancy could be attributed to the encapsulation of the flake, as this could induce some local strain, which has shown to affect the critical field for inducing FM order [38], or to the influence of the adjacent, magnetic monolayer sections. Furthermore, we note that the one trilayer section was magnetized in the opposite spin configuration to the remaining regions of the flake, see orange trilayer region in Fig. 4.3e. This results from spontaneous magnetic ordering during zero field cooling and the region stayed magnetized along the negative b-axis since the external magnetic field applied ($B \approx$ 150 mT) was below the spin-flip field for trialyer CrSBr ($> 200\ mT$). Linecuts of the different layer thicknesses of sample $S2_{\mathrm{Encap}}$, see Fig. 4.3f, show a trend of increasing magnetization per layer with increasing layer thickness. To further investigate this trend, we compare the magnetization of different sample regions in the following section.

4.3.2. Layer dependent magnetism in CrSBr

In order to quantify if the interlayer FM coupling of CrSBr exhibits any layer dependence in the thin limit (N < 5), we compare the magnetization of various CrSBr flakes. We determine the average magnetization through histograms of the reconstructed magnetization maps, see Fig. 4.4 a,b. All the complete, reconstructed data sets can be found in the appendix A.3.1. Applying this approach to a series of CrSBr flakes with increasing layer numbers, we observe an initial increase in the magnetization per layer, independently of whether the sample is encapsulated or not, until reaching the saturation magnetization at $N \gtrsim 5$ layers, close to the expected bulk value of 36 μ_B/nm^2 (Fig. 4.4c), where μ_B is the Bohr magneton. To validate our findings, we independently determined CrSBr's sample magnetization by performing analytic fits to the measured magnetic field emerging from flake edges, as shown in Fig. 4.3c,f, which agrees with our initial approach (see appendix A.3.1 for a complete overview of all fitted values).

The observed increase of magnetization with the number of layers suggests that interlayer exchange coupling [125] plays an important role in stabilizing intralayer FM ordering. Indeed, the scaling of layer magnetization, M_l, with N fits well to an empirical model (black line in Fig. 4.4c) that assumes a magnetization reduction, ϵ, for the outermost layer of Cr atoms, but constant magnetization, M_0, for the remaining Cr layers $M_l = M_0(N - 2\epsilon)/N$. The model yields a bulk magnetization

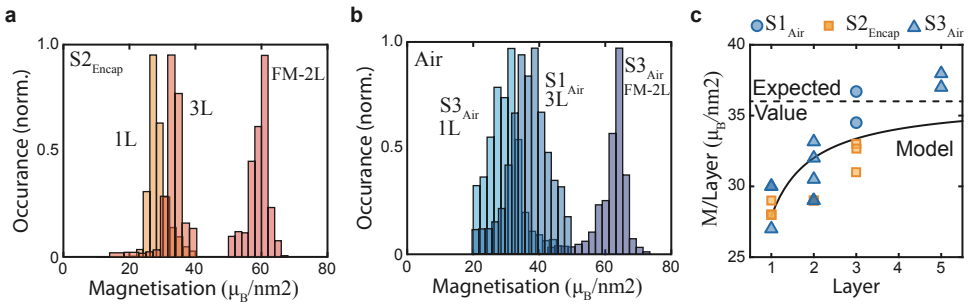

Figure 4.4.: Layer dependent magnetization of few layer CrSBr. **a** Magnetization histograms of encapsulated and non-encapsulated (**b**) flakes of different thicknesses taken from additional datasets, see Appendix A.3.1. **c** Extracted magnetization per CrSBr layer for encapsulated (orange) and non-encapsulated (blue) flakes as a function of the number of layers. The dashed line is the expected value (36 μ_B/nm^2) from bulk measurements and the solid black line is a simplified model fit, which is further described in the text.

$M_0 = 36.1(1)\ \mu_B/\mathrm{nm}^2$, and a reduction factor of 11(4)% for the outermost layers. We note that our findings are reproduced and near-identical whether we investigate encapsulated or non-encapsulated flakes. This attests to the remarkable air-stability of magnetism in CrSBr, which we observe down to monolayers that had been left exposed to ambient conditions for days. While we have not conducted an in-depth analysis of monolayer CrSBr's resilience to air, this already indicates that it has a notable improvement in ambient magnetic stability when compared to 2D magnets e.g. chromium and vanadium trihalides [29, 84].

4.4. Imaging the spin-flip transition in bilayer CrSBr

Magnetic anisotropy manifests as the magnetic field required to align the spins along a crystallographic axis [126, 127]. In materials with strong anisotropy the spins undergo a first-order spin-flip transition, where the magnetic spins of one antiferromagnetically coupled sublattice directly reorient along the external field. For low anisotropy systems, the spins align during a spin-flop transition, where the spins first flip perpendicular to the externally applied field before continuously canting towards the applied field and eventually arranging in an FM configuration.

In the presence of moderate in-plane magnetic fields, CrSBr undergoes such a metamagnetic transition from an interlayer AFM to an FM configuration. For fields applied along the *b*-axis, this corresponds to a sharp spin-flip transition, while for fields along the *a*-axis, a broad transition range indicates continuous canting of the spins [38, 122]. Past observations of non-symmetric hysteresis curves around the spin-flip transition [128], suggest the possibility that FM and AFM phases can coexist during the transition. However, whether such a mixed phase indeed exists and how the spin-flip transitions occur on the microscopic level in CrSBr remains unknown.

In this section we explore how the spins in bilayer CrSBr flip from AFM to FM interlayer ordering in the presence of an external field applied mainly along the *b*-axis, i.e. the magnetic easy axis of the flake. We find that the spin flip transition in bilayer is indeed accompanied by a movement of an AFM/FM phase wall through the flake. The phase wall is stable as a function of applied magnetic field and occurs for both transitions, from AFM to FM (increasing external field) and vice versa (decreasing external field).

4.4.1. Spin-flip transition in bilayer CrSBr

To address the physics of the spin-flip transition in bilayer CrSBr and the possibility of coexisting AFM/FM phases, we initialize a CrSBr bilayer into the FM configuration by applying a magnetic field $B_{\text{ext}} = 230$ mT along the NV axis, such that the in-plane projection of B_{ext} is approximately aligned with the sample's *b*-axis. The field's polar and azimuthal angles amount to $(\theta, \phi) = (53°, 16°)$, where $\theta = 0°$ corresponds to the sample normal and $\phi = 0°$ to the horizontal axis in all images. We subsequently decrease B_{ext} in 10 mT steps and perform qualitative magnetic imaging to identify the AFM to FM flipping field. The qualitative "dual-iso-B" imaging modality, which yields a magnetic field-dependent signal, allows for faster imaging compared to the fully quantitative method (see section 2.3.2 for more details on the imaging modality). This series of images (3 hours per image) is shown in Fig. 4.5. The image region consists of a bilayer and monolayer section with an adjoining thicker section (≥ 4 L), which remains in the AFM state throughout the series (Fig. 4.5 a). We observe that at $B_{\text{ext}} \approx 200$ mT, an AFM ordered region develops in the bilayer section of the flake. This AFM region grows with decreasing external magnetic field until the flake is fully AFM aligned at $B_{\text{ext}} < 160$ mT. The boundary between FM and AFM phases that we term a "phase wall" (PW) is stable and moves incrementally through the sample a the external B-field is decreased. The smoothness of this PW motion is evidence of

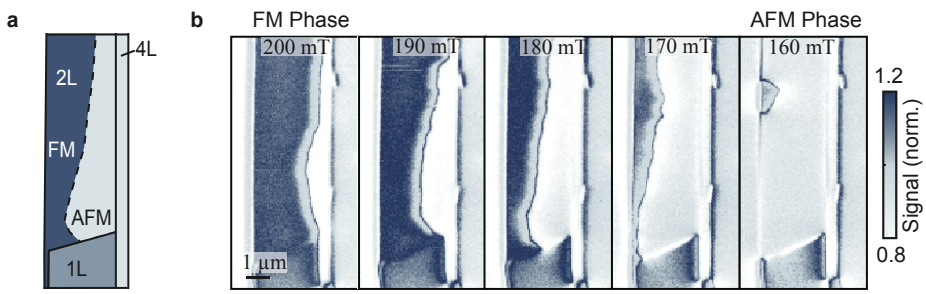

Figure 4.5.: Imaging the spin-flip transition from FM to AFM in bilayer CrSBr. **a** Schematic of the bilayer flake with adjacent monolayer and multilayer sections. Dark blue corresponds to the FM coupled state and gray-blue indicates AFM coupling. **b** Qualitative NV magnetometry images of the movement of the FM-AFM phase wall when demagnetizing the sample from the FM state at $|B_{\text{ext}}| = 200$ mT to the AFM state at $|B_{\text{ext}}| \leq 160$ mT. An additional series of the propagation of the FM to AFM phase wall can be found in Appendix A.3.2.

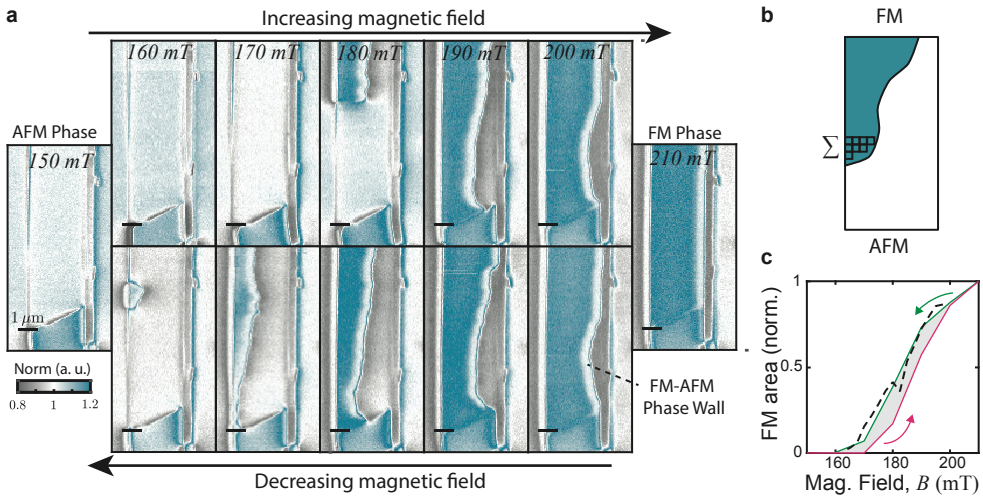

Figure 4.6.: FM to AFM phase wall hysteresis loop in bilayer CrSBr. **a** Measurement series of the phase wall movement through the material using a quantitative imaging technique for both increasing and decreasing fields. Turquoise corresponds to magnetic signal (i.e. FM coupling in bilayer) and white/gray corresponds to no magnetic signal (i.e. AFM coupling in bilayer). **b** Illustration of partially flipped state with thresholding to sum up the pixels in the ferromagnetic state. **c** Magnetic hysteresis extracted from the images in **a**. The dashed line corresponds to data points extracted from the measurement run depicted in Appendix A.3.2.

only weak magnetic pinning in CrSBr. A second data series of the PW evolution in bilayer, recorded with a finer spacing of external B-field, is shown in appendix A.3.2 and shows the reproducibility of the PW motion.

The PW appears both when moving from the FM phase into the AFM phase by decreasing the external field and vice versa for increasing the external field. We imaged this cycle in external magnetic fields to map out the hysteresis of the PW movement through the bilayer, see Fig. 4.6a. These images show a clear difference in the PW position with different magnetic sweeping directions. In order to calculate the hysteresis of the phase wall we sum the number of pixels that are in the ferromagnetic state, as illustrated in Fig. 4.6b, where the ferromagnetic state is define as pixels with a normalized signal greater than 1.05. We define the magnetic signal as the sum of the FM pixels normalized by the number of total pixels on the bilayer region, such that

$$M = \frac{\sum \text{pixels}_{FM}}{\sum \text{pixels}}. \tag{4.2}$$

While this is not a perfect estimation of the FM region it roughly approximates the percentage of FM alignment within the flake. The final result is normalized by the state when the flake is purely in the FM state to set this value to be 1. This results in the hysteresis curve shown in Fig. 4.6**c**. The resulting curve is consistent

with previous, macroscopic measurements [128] , which supports the notion that past hysteresis measurements in the CrSBr spin-flip transition indeed are explained by PW movement throughout the sample.

While we can conclude that the spin-flip process in bilayer CrSBr is a PW assisted reorientation of the spins as a function of external B-field (in contrary to a continuous canting of all the spins), the nature of the PW remains to be understood, i.e. the factors for why the PW can be stabilized in bilayer CrSBr and an estimation of the PW width. We will address these questions with additional measurements and micromagnetic simulations of CrSBr bilayer in the following section.

4.4.2. Analysis of the AFM/FM phase wall in bilayer CrSBr

Imaging the PW in opposite external bias fields, c.f. Fig. 4.7a, shows that the PW moves through the flake independently of the polarity of the external field.

To provide a deeper understanding of the mechanism behind the formation of the AFM-FM PW, we performed micromagnetic simulations, taking into account the known magnetic properties of CrSBr [129–131]. The simulations were performed by Dr. Boris Gross and more details can be found in the Appendix A.3.5.

The micromagnetic simulations cover the entire size of the imaged flake, i.e. $\sim \mu$m sized flake. Whereas atomistic simulations are in general better to account for the structure of layered CrSBr, they reach a computational limit for simulating such large flakes. In order to mimic the layered CrSBr structure in the micromagnetic simulations, we choose the cell thickness of the simulation mesh-grid to be of the height of one CrSBr layer, i.e. one cell spans over 4 nm x 4 nm x 0.8 nm. In the simulations we set the intralayer coupling within each layer to be FM and we set the out-of-plane interlayer exchange coupling to be AFM. The material parameters for the interlayer exchange coupling strengths are determined in an iterative process, where we first simulate bulk CrSBr (cube of 200 nm x 200 nm x 200 nm with periodic boundary conditions) and thereby adjust the parameters until the bulk values for the saturation fields along the main crystal axes and the spin-flip field [117, 121, 122] are roughly matched (see Appendix A.3.5 for more details).

For a homogeneous CrSBr bilayer, we are unable to stabilize a PW in our simulations, i.e. the flake immediately switches from FM to AFM (or vice versa) within one field step at 160 mT (195 mT). We conjecture that inhomogeneities in the sample contribute to the stabilization of the PW. We model these by imposing that the interlayer exchange coupling strength $A_{ex,z}$ exhibits a linear variation along the b-axis that amounts to 24 % across the flake width of 3.3 μm. While other inhomogeneities or pinning centers could also explain the stability of the PW, a variation of $A_{ex,z}$ appears plausible, as it can be induced by strain-gradients [38] that commonly occur in vdW structures [132]. Using literature values [38], we estimate that the variation in $A_{ex,z}$ we impose can be induced by a realistic 0.4% strain variation across the CrSBr flake. Furthermore, we introduce a nucleation point (defect) in the top left corner of the CrSBr flake, to initialize the PW. Figures 4.7b and c show the resulting simulated sample magnetization and stray field pattern in the presence of the PW, where the latter shows good agreement with our experimental data. In contrast to the experimentally observed PW, the simulated PW extends perfectly along the a-axis, which results from the linear gradient in exchange coupling introduced in the simulations.

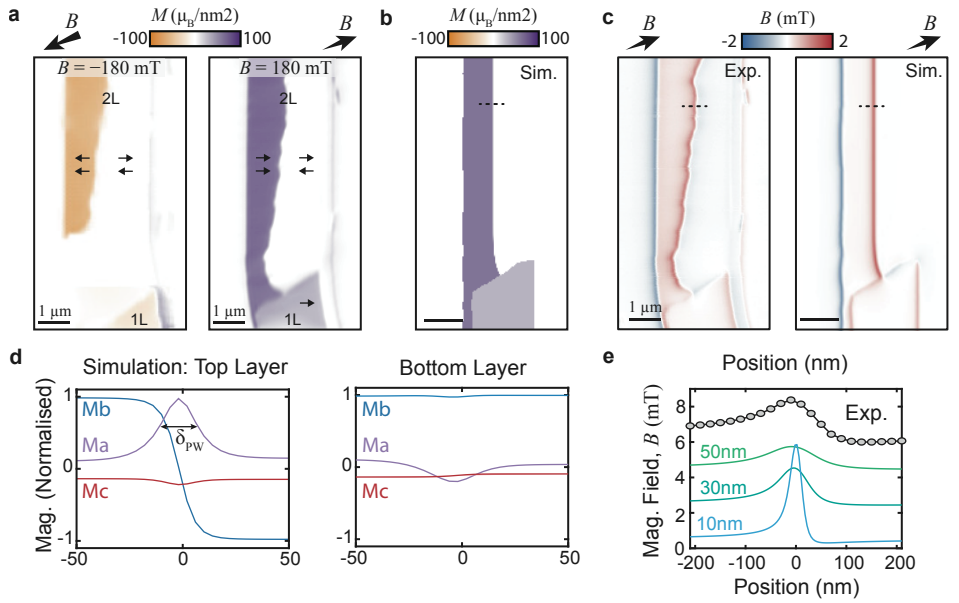

Figure 4.7.: Analysis of the phase wall in bilayer CrSBr. **a** Image of coexisting FM and AFM phases in a CrSBr bilayer obtained at $|B_{\text{ext}}| = \pm 180$ mT after demagnetizing the sample from higher fields, with a magnetic field axis oriented along $(\theta, \phi) = (53°, 16°)$. The images were obtained by magnetization reconstruction from raw $|B_{\text{NV}}|$ data . **b** Micromagnetic simulation of the phase wall under the same conditions as the right panel in **a**. **c** Experimental magnetic stray field image from the measurement in **a** and simulated magnetic field from **b**. **d** Cross sections of the magnetization vector across the phase wall (dashed line in **b**) resulting form the micromagnetic simulations for both the top and bottom layers. **e** Comparison of the experimental measured magnetic field line cut across the phase wall (dashed lines in **c**) and the simulation with various NV-sample standoff distances. The different lines are offset for clarity.

Our simulations further show that the magnetization rotation across the PW is largely confined to the a-b plane (Fig. 4.7d). By fitting the magnetization cross section $\mathrm{M_b}$ to a tanh function, we can extract the phase wall parameter Δ:

$$M_b = \tanh\left(\frac{b - b_0}{\Delta}\right), \tag{4.3}$$

where b_0 represents the PW center along the b-axis and Δ is the PW parameter. From this we can extract a phase wall width of $\delta_{PW} = \pi\Delta = 18$ nm (Fig. 4.7e), which is below the spatial resolution of our method. Yet, the experimental data show good agreement with the model and their comparison allows us to estimate the NV-sample distance (that sets the spatial resolution) to ~ 50 nm (Fig. 4.7e).

4.4.3. AFM/FM spin-flip in trilayer CrSBr

To investigate whether the spin flip transition in thicker flakes is also PW assisted, we image a trilayer section of sample $S2_{\text{Encap}}$, see Fig. 4.8a. The small trilayer section flips to an FM state in an external magnetic field of $B = 300$ mT applied along the NV axis, Fig. 4.8b. Reducing the applied field to $B = 290$ mT introduces AFM regions in the trilayer flake, Fig. 4.8c. Unlike in the bilayer case, these regions exhibit a time dependence, which we observe by re-imaging the flake at the same field ($B = 290$ mT) where with every scan the AFM regions extend further. These results are confirmed by initializing the trilayer flake in the FM state again (applied $B = 300$ mT) and subsequently reducing the field to $B = 250$ mT: AFM regions form and propagate through the flake, Fig. 4.8d. In contrast to the FM/AFM PW in bilayer CrSBr, which was stable for multiple hours to days under an external applied magnetic field, the boundaries of the AFM regions observed in trilayer rapidly change (snapping to new location within a line scan, t < 20 min). This could be explained by local influence of our measurement technique, such as laser light induced heating and therefore dragging of the phase boundary or spontaneous flipping of the magnetization ("jumps") induced by scanning across the flake in the meta-stable FM/AFM state. The fact that no stable PW is observed in trilayer could also relate to the specific geometry of a CrSBr flake , i.e. the trilayer flake we investigate is narrower (x 0.25) compared to the bilayer flake, which showed a stable PW during the spin-flip transition. Due to the reduced surface area of a potential PW along the *b*-axis in this specific trilayer flake, there is a lower energy cost of moving such a domain.

It remains to be identified how these phase walls propagate in thicker stacks. For instance, it is not obvious if in a spin-flip transition all layers of a CrSBr stack will flip at once or consecutively, or if within the stack the layers will split up in different AFM

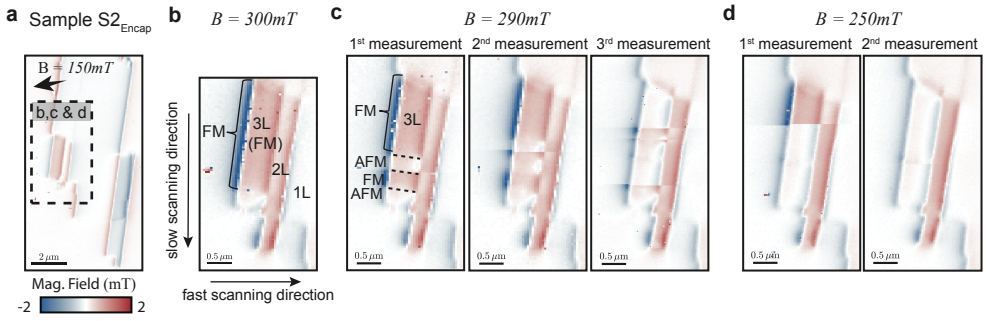

Figure 4.8.: Phase wall movement in trilayer CrSBr. **a** Magnetic stray field map of sample $S2_{\text{Encap}}$ measured in an external field of $|B_{\text{ext}}| = 150$ mT. Dashed box marks the region of the trilayer section shown in panels **b-d**. **b** Magnetic field map of completely FM ordered trilayer CrSBr measured in an external field of $|B_{\text{ext}}| = 300$ mT. Black arrow marks the extend of the FM 3L region. **c** Consecutive measurements of the formation of AFM regions in predominantly FM ordered trilayer CrSBr in a lower, external bias field of $|B_{\text{ext}}| = 290$ mT. The flake was measured consecutively for three times in a row (1st to 3rd measurement). **d** Analog to **c** but measured in a yet lower external B-field of $|B_{\text{ext}}| = 250$ mT.

coupled regions or not. Our current scanning NV magnetometry setup, however, is limited to measurements in fields $B \leq 300$ mT, due to the limit of MW frequency we can supply to drive the NV, and would need to be upgraded in order to image the spin flip for stacks with ≥ 4 layers.

4.5. Temperature dependent magnetism in CrSBr

There have been several studies suggesting that CrSBr enters an intermediate FM phase, iFM, above the Néel temperature and below the Curie temperature [114, 117], where the FM intralayer order within the individual CrSBr layers persists but without interlayer correlation. However, no local nanoscale imaging probe has been utilized yet to explore this magnetic phase and its spin configuration in few layer CrSBr. To gain further insight into the high temperature regime of few layer CrSBr, we perform a series of measurements between $120-160$ K, with the aim of extracting the in-plane anisotropy of the material and investigating the loss of long range order.

We study a monolayer/bilayer CrSBr sample, sample $S4_{\mathrm{Air}}$ (c.f. Fig. 4.2d), at elevated temperatures. In all measurements (unless otherwise stated) the temperature was measured by a resistive thermal couple located at the top of the piezo stack which held the sample. Due to the application of microwaves to drive the NV spin we expect some offset in the real sample temperature compared with that sensor temperature. This offset is MW power dependent and hard to calibrate for a large range of temperatures. As such, we reference the temperature that was measured by the sensor,

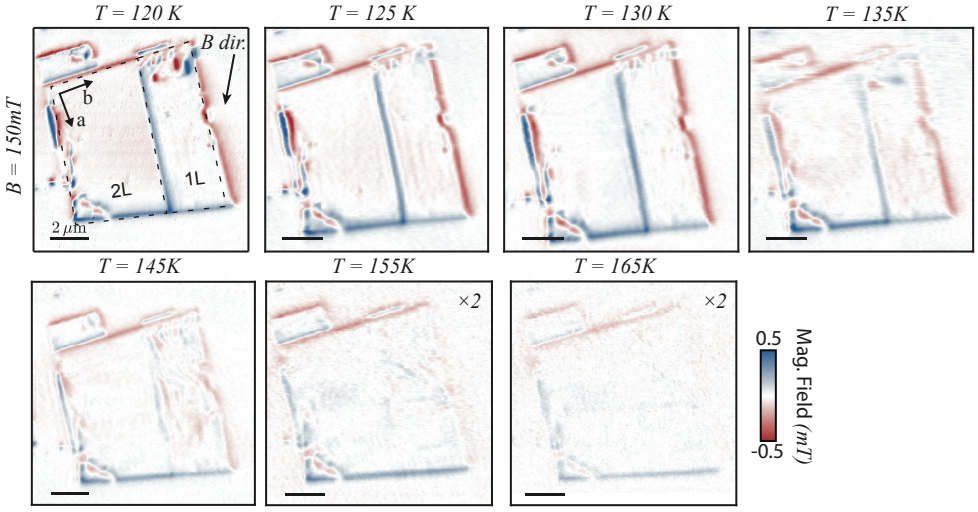

Figure 4.9.: Imaging mono- and bilayer CrSBr below and above the critical temperature. Full temperature series from $T = 120$ K to $T = 165$ K of sample $S4_{\mathrm{Air}}$. All data sets were recorded in an external bias field of $|B_{\mathrm{ext}}| = 150$ mT roughly aligned along the intermediate a-axis of the material with an out of plane angle of approximately 28°.

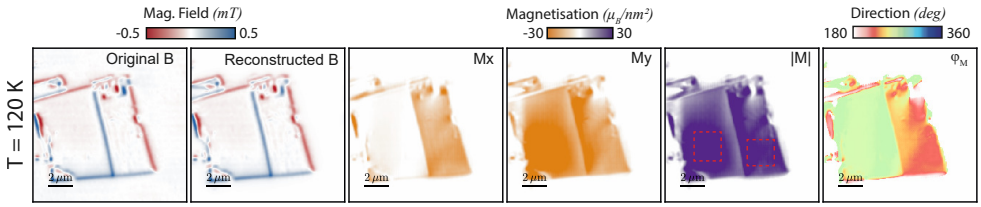

Figure 4.10.: Exemplary magnetization reconstruction of the stray field data at 120 K. The panels from left to right are: The original magnetic field, the reconstructed magnetic field by the neural network, the magnetization along the X-direction of the image (corresponds to the easy (b)-axis), the magnetization along the Y-direction (corresponding to the intermediate (a)-axis) of the image, the magnitude of the total magnetization, and the direction of the magnetization.

which means the real sample temperature is few degrees higher than the indicated temperature.

To investigate the transition from AFM to FM order at higher temperatures we applied a magnetic field along the intermediate a-axis of $S4_{\mathrm{Air}}$. We then maintained this magnetic field ($B = 150$ mT, $\phi = 262°$, and $\theta = 62°$) while increasing the temperature, mapping the stray magnetic field at each temperature. The resulting magnetic images are all shown in Fig. 4.9, with two main observations:

First, the magnetization orientation between the bilayer and the monolayer flake varies with different temperatures. At 120 K the bilayer is magnetized along the a-axis of the material, while the monolayer remains mainly polarized along the b-axis. With increasing temperature the monolayer magnetization starts to rotate towards the a-axis, which can be seen from an increase of the stray field at the bottom edge of the monolayer. We will show below how we can determine the magnetization rotation in our data sets. By quantifying this magnetization rotation at different temperatures, we can infer the anisotropy of monolayer CrSBr, which will be described in Sect. 4.5.1 below.

Second, we observe spatial variations of magnetization in the monolayer flake in a temperature range around $145\ K \pm 5\ K$. This could be an indication of loss of long-range order in the intermediate FM state of CrSBr. We will further discuss potential interpretations of these magnetic variations in monolayer flakes in Sect. 4.5.2 below. Additionally, we extend our discussion to more high temperature images of multilayer- and also encapsulated flakes to study these magnetic textures and to shed light into the intermediate FM state of few layer CrSBr.

4.5.1. Determining the anisotropy of monolayer CrSBr

In this section we will determine the anisotropy of monolayer CrSBr from our temperature dependent data series shown in Fig. 4.9 previously. By extracting the magnetization direction and magnitude for each temperature and applying the Stoner Wohlfarth model [133] for anisotropy, we can estimate the effective anisotropy for the monolayer flake.

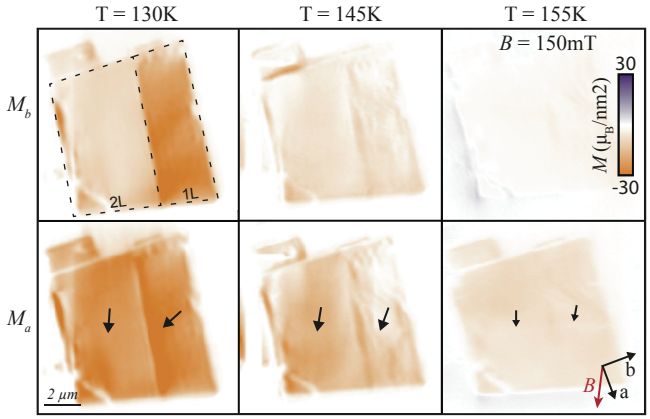

Figure 4.11.: Magnetization direction reconstruction at different temperatures. Reconstruction [134] of magnetization components along the CrSBr b-axis (M_b, top panels) and a-axis (M_a, bottom panels) for different temperatures, under a magnetic bias field applied roughly along the a-axis ($(\theta, \phi) = (65°, 265°)$). The black arrows indicate the overall magnetization direction within the different layered regions of the CrSBr flake.

First, we describe how we can determine the magnetization both along the a-axis (M_a) and b-axis (M_b) of sample $S4_{\text{Air}}$ simultaneously using a neural network based reconstruction method[3] (see section A.1). For our data analysis we modified the neural network reconstruction method to produce two maps, one for M_x and one for M_y, as shown in Fig. 4.10. The x-axis (y-) aligns with the easy, b- (intermediate, a-) axis of the CrSBr flake. The two respective magnetic fields are calculated independently and afterward combined to compare with the measured magnetic image. The reconstructed magnetization can be used to extract the total magnetization and the magnetization direction for each pixel. Where we determine the magnitude as

$$|M| = \sqrt{M_x^2 + M_y^2}, \tag{4.4}$$

and the direction as

$$\phi_M = \arctan\left(\frac{M_y}{M_x}\right). \tag{4.5}$$

To minimize the background noise, two techniques are used: For the lower temperature case, a mask is introduced to restrict the reconstruction to produce magnetization only inside the flake. The mask is introduced by edge detection of the magnetic field. In the case of the higher temperature data (T = 155 and 165 K), the signal is weaker so instead in the magnetization direction the images have a threshold applied such that if the total magnetization is smaller than 5 μ_B/nm^2, the pixel is treated as white background.

[3] Dr. David Broadway implemented all the analysis code for magnetization direction dependent reconstruction.

Here, we present three reconstructed data sets at $T = 130$ K, $T = 145$ K and $T = 155$ K in Fig. 4.11. The full reconstruction of all the temperature data is shown in the appendix A.3. The anisotropy would indicate that the spins in the bilayer (also in the AFM state) should be orientated along the b-axis of the material. However, we observe magnetism pointing along the magnetic field direction along the a-axis due to spin-canting, which tends to align spins in both layers towards the magnetic field direction. In contrast, the monolayer magnetization for our initial temperature $T = 130$ K is initially nearly aligned with the easy axis, indicating that the effective magnetic anisotropy energy, K^*, exceeds the Zeeman energy. As we increase T, the monolayer magnetization not only decreases in magnitude but also reorients towards the a-axis. This reorientation results from a reduction of K^* with increasing temperature [135]. At higher temperatures, the increased thermal-magnon density perturbs the magnetic spins, which results in a lower effective anisotropy K^* because the stability offered from magnetocrystalline anisotropy can now more easily be overcome with Zeeman energy.

For each temperature, we can determine the magnetization and canting angle of the monolayer flake, see Fig. 4.12. Using these parameters, we are able to quantitatively

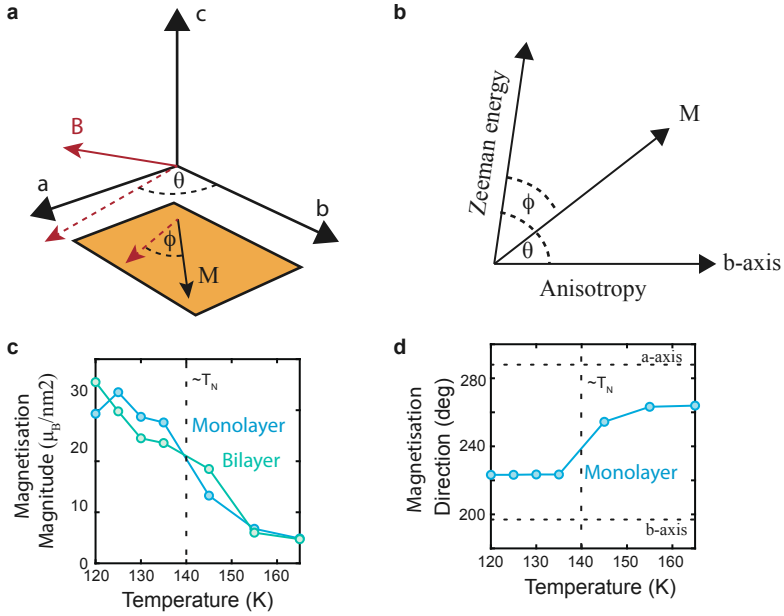

Figure 4.12.: Method for extracting anisotropy from NV measurements. a Illustration of a magnetic flake with an easy axis along the b-axis and a magnetic field at an arbitrary angle (red arrow, dashed for projection onto the a-b plane). **b** Illustration of different energy contributions, where the magnetization points along a direction that is given by the combination of Zeeman and anisotropy energy. **c,d** Magnetization strength (**c**) and direction (**d**) dependence as a function of temperature extracted from the measurement series shown in appendix A.3.3.

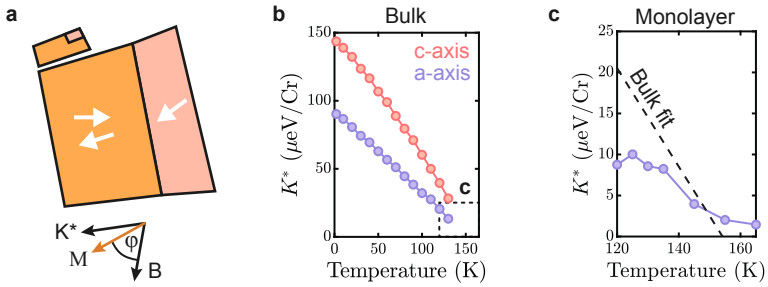

Figure 4.13.: Determination of magnetic anisotropy in a CrSBr monolayer. **a** Illustration of the two competing interactions: effective anisotropy (K^*) and Zeeman energy (B), and their effect on the magnetization direction of the material. **b** Effective in-plane and out-of-plane anisotropy of bulk CrSBr measured with vibrating sample magnetometry by our collaborators at Columbia University. **c** Extracted effective in-plane anisotropy (K^*) from the measurements in Fig. 4.11 and the extrapolated anisotropy from the bulk measurements in **b** assuming a linear trend. The dashed box in **b** indicates the range of **c**.

extract K^* for monolayer CrSBr based on the Stoner Wohlfarth model [133], which models the energy of a magnetic system under the influence of a magnetic field using the expression

$$E = KV \sin^2(\phi - \theta) - M_s V B_{ext} \cos\phi, \tag{4.6}$$

where K is the magnetocrystalline anisotropy, V is the magnet volume, M_s is the saturation magnetization, B_{ext} is the external magnetic field, ϕ is the angle between the magnetization direction and the external field, and θ is the angle between the applied field and the easy axis of the material. An illustration of this situation is shown in Fig. 4.12a,b.

The magnetization direction is in equilibrium if the torques which act on it are zero, which corresponds to the derivative of the energy with respect to ϕ being equal to zero:

$$\frac{\partial E}{\partial \phi} = 2KV \sin(\phi - \theta)\cos(\phi - \theta) - M_s V B_{ext} \sin\phi = 0. \tag{4.7}$$

We extract the anisotropy by rearranging the equation above to solve for K:

$$K = \frac{M B_{ext} \sin\phi}{2\sin(\phi - \theta)\cos(\phi - \theta)}. \tag{4.8}$$

Using this equation we determine the anisotropy of the monolayer using the measured magnetization M (Fig. 4.12c) and direction ϕ, (Fig. 4.12d).

The resulting single spin anisotropy energy as a function of temperature is shown as the purple points in Fig. 4.13c. To compare our results to reference values, we turn

to bulk measurements of anisotropy in CrSBr[4] plotted in Fig. 4.13b. Extrapolating the bulk anisotropy measurement to higher temperatures (Fig. 4.13c, dashed line) yields qualitative agreement with our results and indicates that the primary source of magnetic anisotropy for the monolayer is magnetocrystalline anisotropy.

4.5.2. Imaging magnetic texture in CrSBr near the critical temperature

From our high temperature data series, c.f. Fig. 4.9, it is evident that the FM order in monolayer persists well beyond the nominal bulk Néel temperature $T_N \approx 132$ K of CrSBr, consistent with earlier observations of intralayer correlations in CrSBr for $T > T_N$ [62, 122]. To further elucidate the still unclear nature of this intermediate FM regime [114], we investigate the monolayer region of sample $S4_{Air}$ in a temperature range slightly above T_N and in various external magnetic fields, shown in Fig. 4.14.

In the low field regime (B$<$ 10 mT), shown in the three most left panels in Fig. 4.14b, clear spatial variations of the magnetization are observed. As mentioned before, these inhomogenities are only present in a small temperature window, when $T_N < T < T_c$. It is notable that the adjacent bilayer does not show any spatial variation in magnetization. This is most likely due to the remaining AFM order in thin layers above T_N, which would compensate for the magnetic ordering. This observation is consistent with measurements of different CrSBr flakes at higher temperatures: An additional data series for sample $S1_{Air}$ is attached in the Appendix A.3.4, and shows magnetic variations appearing in trilayer CrSBr, whereas its bilayer part stays AFM. Additionally, we investigate an encapsulated device, sample $S2_{Encap}$, which will be described further below.

To explain the origin of the observed magnetization variations, we have to rule out any potential interference from our measurement technique: There is the possibility of our AFM tip interfering with the sample surface during scanning, which could alter the topography and induce folds, which would in turn lead to a variation in measured magnetization. Given that most of the magnetic texture disappears by applying a larger external field (B $\geq$ 200 mT), see right panels in Fig. 4.14b, and a mostly uniform magnetization is restored, we can most likely assume that there was no correlation or damage induced by our tip. However, to rule out any potential tip induced alternation of the CrSBr flake, we image an encapsulated CrSBr, where the top encapsulation layer will protect the CrSBr flake from any tip induced uncontrolled damage.

To this end, we take magnetic images of sample $S2_{Encap}$ at elevated temperatures. We initialize the flake through cooling below the critical temperature in zero magnetic field. At $T = 120$ K we apply a small magnetic field $B = (\theta, \phi, |B|) = (55°, 80°, 5\text{ mT})$ and image the flake (Fig. 4.15, left panel). As expected for the AFM coupled ground state of CrSBr at $T = 120$ K, the odd layer (1,3) regions exhibit stray magnetic fields at their respective edges and the sample is homogeneously magnetized. This

[4]The bulk anisotropy measurements were obtained by our collaborators at Columbia University, NY. They have measured the saturation magnetization and saturation field at different temperatures for external fields along either the a-, b- or *c*-axis. By using the difference between the a- (c-) axis saturation field and the *b*-axis saturation field they calculated the effective magnetic anisotropy energy (K^*) for the a and c axes based on the Stoner-Wohlfarth model. More details can be found in the supplementary material of [9].

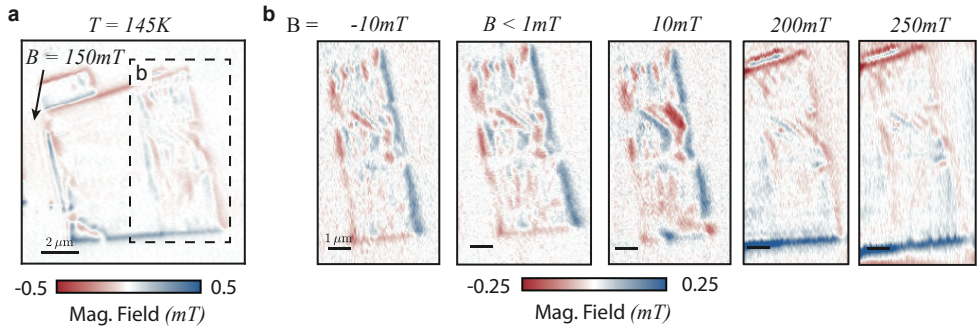

Figure 4.14.: Imaging monolayer CrSBr near the critical temperature. **a** Magnetic stray field image of sample $S4_{\mathrm{Air}}$ at $T = 150$ K, identical to Fig. 4.9. Dashed box indicated monolayer section of the flake. **b** Magnetic stray field images of monolayer CrSBr taken at $T = 150$ K in various external magnetic fields, ranging from < 1mT to 250mT, highlighting the appearance of magnetic textures in the sub micron range.

configuration is maintained up at $T = 130$ K without evidence of deviation. However, at $T = 138$ K we observe a notable shift, where magnetic features appear in the previously pristine mono- and trilayer regions. Increasing the temperature further to $T = 140$ K removes many of these features, illustrating the very small temperature window ($\delta T \sim 10\ K$) that this effect is observable.

In this measurement series, one can observe a gradient in the stray magnetic field strength across the sample, particularly at higher temperatures (Fig. 4.15, right panels). We attribute this to a temperature gradient that is induced across the sample due to joule heating from the MW antenna, which is used to drive the NV spin and is located to the right of these images, approximately 80 μm away from the flake. Additionally, during this measurement series, the temperature readout to the main sensor was lost. As such, the temperature quoted was measured further away compared to the other high temperature scans at therefore the sample temperature is several degrees warmer than the stated temperature.

We have consistently observed a variation in magnetization in odd layered CrSBr, for both encapsulated and non-encapsulated samples close to the transition temperature. Our experimental observations help us identify the most likely origin of the inhomogeneities in the intermediate FM phase. First, we note that the inhomogeneities appear completely static over the timescale of our experiments of several days. This excludes critical spin fluctuations near T_{c}, or the appearance of unbound meron/anti-meron pairs [136] as their origin. Second, a near-homogeneous monolayer magnetization can be restored by increasing B_{ext} to around 200 mT (see Fig. 4.14), indicating that the saturation magnetization is nearly constant across the sample. Given that the magnetic anisotropy K^* is near-vanishing for $T \gtrsim T_{\mathrm{N}}$ variations in K^* appear unlikely as the origin for the observed inhomogeneities. This would leave local variations of intralayer exchange couplings as the most likely explanation for our observation. These local variations could originate from atomistic defects, strain variation, or other local disorders that could disrupt the regular crystallographic structure.

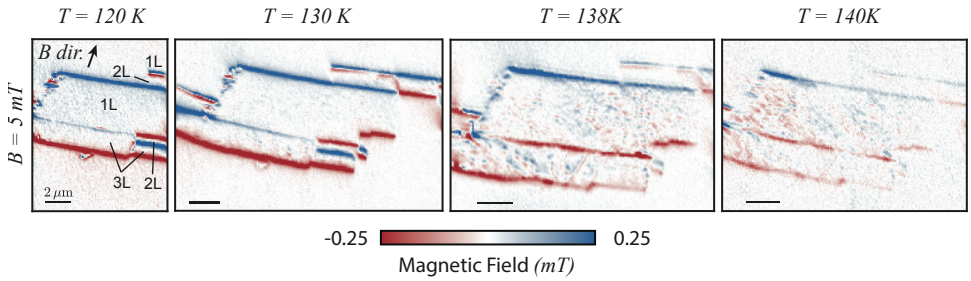

Figure 4.15.: Properties of CrSBr mono- and trilayer near $T = T_N$. Magnetic field images of Sample $S2_{Encap}$ at $T = 120 - 140$ K in a bias magnetic field $B_{ext} = 5$ mT applied along the b-axis (with an out-of-plane component of approximately 35°). The onset of short-range magnetic inhomogeneities at $T = 138$ K is apparent in regions with odd numbers of layers.

To further elucidate the nature of magnetic ordering in the intermediate magnetic phase of CrSBr, we turn to measurements on bulk crystals[5]. In Fig. 4.16a, we show the real part [6] of the zero-field AC susceptibility χ_{AC} of a bulk CrSBr crystal. Within the probed parameter range, χ_{AC} is frequency independent and displays a single cusp at $T_N = 132$ K. The absence of an additional higher temperature feature in χ_{AC} indicates that, despite the presence of FM correlations persisting to temperatures $T > T_N$, no additional short- or long-range intralayer order emerges in CrSBr above T_N at zero-field. However, in the presence of applied bias magnetic fields, a field-dependent maximum in $\chi_{AC}(T)$ emerges (Fig. 4.16b). The magnetic field dependence of this high-temperature feature can be used to extract critical exponents for magnetic ordering in CrSBr [137, 138]. Intriguingly, the extracted values of $\beta = 0.22(2)$ and $\gamma = 2.28(2)$ are close to the values expected for the 2D-XY model ($\beta = 0.231$ and $\gamma = 2.4$ [43, 139]). The value of β we determined aligns with values previously determined by a range of experimental techniques [117, 140] and earlier conclusions that CrSBr follows 2D-XY-like behavior above T_N [136].

Our combined findings indicate that easy-plane behavior of single, FM layers of an odd-layered CrSBr flake (e.g. 1L, 3L, ..., etc) could exist in a narrow temperature range above T_N and below T_c, in which 2D-XY-like physics could thereby be observed in CrSBr. However, in our present samples, this behavior is likely masked by the inhomogeneities in intralayer exchange coupling, as discussed earlier. Future advances in material purification [141] and isolation from the substrate could therefore offer exciting perspectives for observing 2D-XY spin physics[142] with its accompanying topological spin textures [136] in monolayers of the CrSBr family.

4.6. Conclusion and Outlook

In this chapter, we provided a quantitative, nanoscale study of magnetization strength and anisotropy in few layer CrSBr samples and addressed two key magnetic phase

[5]There experiments were conducted by our collaborators at Columbia University, NY.
[6]The imaginary part of χ_{AC} remains ≈ 0 over the entire temperature range studied here.

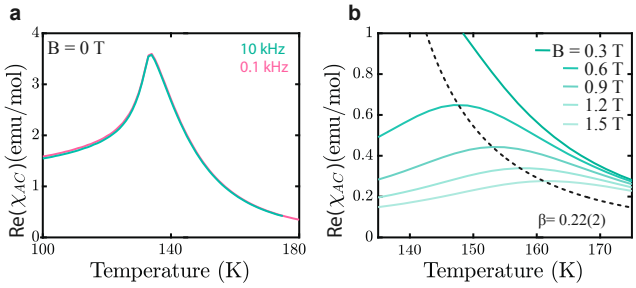

Figure 4.16.: AC susceptibility of bulk CrSBr at elevated temperatures. **a** Real part of the zero-field, AC magnetic susceptibility χ_{AC} of bulk CrSBr. The data indicate a lack of additional magnetic phase transitions for $T > T_N = 132$ K. **b** Same as **a** obtained in nonzero bias magnetic fields B_{ext}. From these data, we extract critical parameters $\beta = 0.22(2)$ and $\gamma = 2.28(2)$, both approaching the expected values for an ideal 2D-XY spin model ($\beta = 0.231$ and $\gamma = 2.4$ [43]). AC susceptibility data were collected with B parallel to the a-axis with an oscillating field of 1 mT by our collaborators at Columbia University.

transitions by direct magnetic imaging using single-spin magnetometry. We observed that the magnetization per CrSBr layer decreases monotonically with layer number, but remains nonzero even for monolayers, which we find magnetically stable even in the absence of encapsulation. We further investigated the AFM-FM spin-flip transition in bilayers and found them to be driven by the nucleation and subsequent propagation of a phase wall, rather than a coherent rotation of the layer magnetization. Finally, we addressed the evolution of magnetization near CrSBr's critical temperature and directly evidenced the reduction of anisotropy when approaching T_N. Near T_N, we observed the onset of magnetic inhomogeneities in odd-layer flakes, which we attributed to local disorder in intralayer exchange couplings that currently mask a native 2D-XY behavior of CrSBr monolayers.

Future experiments on CrSBr could include the study of the potentially present 2D-XY phase at intermediate temperatures of $\sim$ 145 K. In order to observe 2D-XY like physics in CrSBr, the local disorder in interlayer exchange coupling needs to be reduced/removed. One route would be to fabricate and examine suspended CrSBr sheets, to mitigate any interaction with the substrate. Alternatively, different fabrication techniques for producing monolayer CrSBr could be explored, in order to avoid or minimize any strain induced by mechanical exfoliation, which could affect inhomogeneities in the flake.

In order to study exotic magnetic phases and anisotropy effects in 2D magnetic systems, it could be interesting to examine orthogonally twisted bilayer CrSBr [143]. The authors of [143] have found via transport measurements that by twisting two monolayer CrSBr sheets with an 90° twist angle, they can create an interesting spin configuration where they have observed field induced mutlistep switching. They hypothesize that the observed multistep switching could be due to domain formation in the twisted region. It would be worthwhile to locally probe the domain formation with single spin magnetometry and verify if such domains exist. Furthermore, nanoscale

magnetic imaging could give insight into the flipping process of the spins when external fields are aligned in between the a- and *b*-axis, for example at an 45° angle. It is not known yet, which magnetic field and anisotropy contributions would dominate in such a scenario and how it would affect the flipping or canting of the spins. Studying such twisted 2D magnetic heterostructures could open the path for observing and manipulating exotic magnetic structures, such as skyrmions and merons [144, 145].

To summarize, our results on nanoscale investigations of magnetism in CrSBr underline the material's significant potential for the development of novel technologies based on 2D magnets. In particular, the air stability, and large-range uniformity of magnetization across tens of microns evidence robustness and scalability of this material, while the highly stable magnetic phase wall we discovered suggest potential interesting functionalities in the context of spintronics and racetrack memory devices [146].

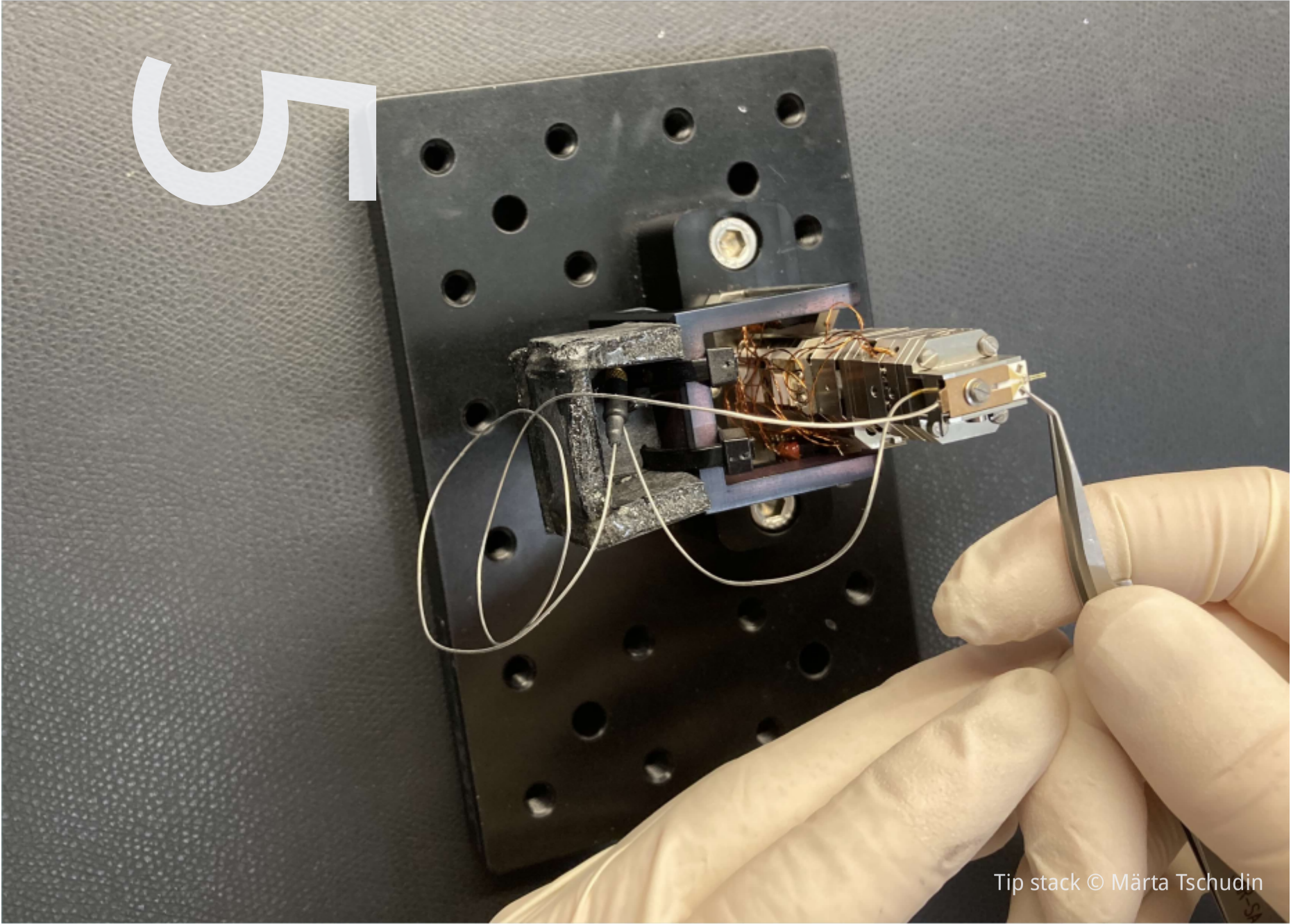

Tip stack © Märta Tschudin

5. Domain Walls in Bilayer CrSBr

This chapter is based on unpublished data recorded in the Quantum Sensing Lab, University of Basel, Switzerland[1].

5.1. Introduction

Domain walls are fundamental concepts in condensed matter physics, defining boundaries between adjacent regions within a material where magnetic moments align differently. These interfaces, termed domain walls, manifest gradual changes in spin orientation from one domain to another. Studying such domain walls gives insight into a material's magnetic properties and dynamics, such as exchange interactions [44, 147], and is crucial for technological advances in areas such as spintronics, magnetic memory, and quantum computing [148].

In condensed matter physics and material science, antiferromagnetic (AFM) domain walls have gained a lot of interest due to their inherent stability against external magnetic fields, which makes them promising candidates for spintronic applications [149, 150]. Together with the recent development of two-dimensional van der Waals (vdW) materials, an exciting new playground emerged: The ability to observe and manipulate AFM domain walls in vdW materials opens up possibilities for exploring novel magnetic phenomena and developing next-generation spintronic and magnetic storage devices based on 2D materials.

While researchers have successfully observed AFM domain walls in thick vdW materials or thin films using various experimental techniques, including scanning tunneling microscopy (STM) [21], magnetic force microscopy (MFM) [23], X-ray spectroscopy [24] and NV centers in diamond [22], the observation of AFM domain walls in atomically thin vdW materials remains largely unexplored.

In this chapter we image the creation of an antiferromagnetic (AFM) domain wall in the 2D magnet CrSBr by single spin NV magnetometry. Based on micromagnetic simulations we show that the domain walls initiated in bilayer CrSBr most likely consist of an AFM core of spins with a lateral displacement in the spin rotation in the opposing layers, however, further theoretical and experimental work will be required to confirm this hypothesis. Furthermore, we find that the presence of an AFM domain in bilayer CrSBr induces the nucleation of a ferromagnetic "cusp"-shaped region during the spin-flip transition. Our results demonstrate for the first time the observation of AFM walls in an atomically thin vdW magnet and ultimately shed light into the underlying spin configuration of the magnetic moments within the individual layers.

[1]Data recorded by M. A. Tschudin, C. Pellet-Mary, D. Dutta, P. Siegwolf (Reiser), C. Schrader and D. A. Broadway under the supervision of P. Maletinsky. The samples described in this chapter were fabricated by J. Cox and E. Telford under the guidance of C. Dean and X. Roy and the micromagnetic simulations were done by B. Gross under the supervision of M. Poggio.

5.2. AFM domain walls in bilayer CrSBr

In the following sections we will discuss the observation of AFM domain walls in bilayer CrSBr, imaged via single spin microscopy based on NV centers in diamond.

5.2.1. Bilayer CrSBr flake

In order to study AFM domain walls in thin vdW magnets, we investigate a bilayer CrSBr flake, c.f. Fig. 5.1. CrSBr is an air stable 2D magnet with a Néel temperature of ~ 132 K [114], as discussed in section 4.2 of the previous chapter. Individual layers of CrSBr couple antiferromagnetically and the intralayer coupling is ferromagnetic (FM), i.e. within one layer all the spins align FM. The material has a magnetic easy-axis (b-axis) along the short, geometrical axis of the flakes, see Fig. 5.1a. More details on CrSBr, such as the crystallographic structure and origin of magnetism, are described in section 4.2.

The sample we study consists of a large bilayer section, interfacing mono- and trilayer CrSBr, as shown in the optical microscope image in Fig.5.1a. The layer thickness of the CrSBr flake is determined by plotting the optical contrast between the flake and the Si/SiO_2 substrate (Fig. 5.1b). Similarly to the CrSBr samples studied in the previous chapter (section 4.3, Fig.4.2), we find an absorption of approximately 15% for one single layer of CrSBr in our optical microscope.

For all measurements discussed in this chapter, the CrSBr samples have been zero field cooled and subsequently measured at around 4 K, except for the data presented

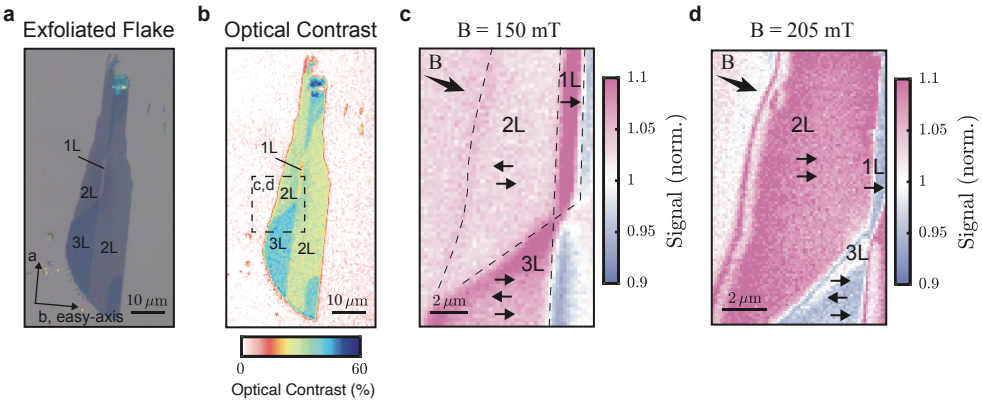

Figure 5.1.: Few-layer CrSBr flake a Optical microscope image of an exfoliated CrSBr flake with layer thicknesses ranging from one to three layers. **b** Optical contrast extracted from the microscope image to determine the layer thickness of the flake. **c** Magnetic field image (qualitative) at $|B_{\mathrm{ext}}| = 150$ mT, where bilayer CrSBr couples antiferromagnetically and stray fields only emerge from odd layers. The image was taken at a fixed NV-to-sample distance of 300 nm (out-of-contact scan). **d** Magnetic field image (qualitative) at $|B_{\mathrm{ext}}| = 205$ mT, where bilayer CrSBr flips to couple ferromagnetically. The data was recorded at a fixed NV-to-sample distance of 200 nm (out-of-contact scan).

in the high temperature section 5.3, where the flake was imaged at $T = 120 - 130$ K. For magnetic imaging we apply an external magnetic field along the NV-axis (defined by the angles ϕ, the azimuthal angle quoted here respective to the b-axis of CrSBr and θ, the angle away from the c-axis). We either image the flake in a qualitative "dual-iso-B" imaging modality (data plotted in pink/purple color scheme), which yields a magnetic field-dependent signal and allows for faster imaging compared to the fully quantitative method (see section 2.3.2 for more details on "dual-iso-B" imaging). Or we image the flake quantitatively (data plotted in red/blue color scheme), which requires more measurement time but in turn allows for the quantitative determination of CrSBr's magnetic stray field (see section 2.3.2 for more details).

At 4 K and low magnetic field, bilayer CrSBr does not exhibit a considerable magnetic stray field due to the AFM interlayer coupling, as shown in Fig.5.1c. Imaging the CrSBr flake in an external field of $|B_{\text{ext}}| = 150$ mT, shows stray field emerging solely from the odd layered regions, i.e. monolayer and trilayer, as indicated with the black arrows which denote the plausible spin alignment of the individual CrSBr layers. The spatial resolution of this data set is $\sim$ 300nm, which corresponds to the NV-to-sample distance (height), which was kept constant for this scan by scanning out-of-contact[2].

However, the bilayer CrSBr can be flipped to a FM configuration by passing through the spin-flip transition, which occurs around 200 mT along the b-axis of the material [9, 121], see Fig.5.1d (measured at a constant height of $\sim$ 200nm). We have shown in the previous chapter that the spin-flip is accompanied by the propagation of a FM-AFM phase wall through the sample, c.f. section 4.4. These results have shown that different spin configurations in CrSBr can be stabilized, which makes this material a promising platform for studying various spin textures. By studying spin textures in CrSBr in more depth, we unravel the presence of AFM domain walls in bilayer CrSBr in this chapter. We show that AFM domain walls induce specific morphologies of FM regions in the FM-AFM spin-flip transition and our results ultimately shed light into the underlying spin configuration of the magnetic moments in bilayer CrSBr, as described in the sections below.

5.2.2. Initialization of an AFM domain wall in bilayer CrSBr

We are able to induce a domain wall in AFM ordered bilayer CrSBr, as shown in the qualitative magnetic field image in Fig. 5.2a. This scan is recorded in with a NV-to-sample distance of $\sim$ $40-60$ nm. In order to induce the domain wall, we initialize the trilayer flake in an opposing spin configuration to the top part of the bilayer flake (by applying a negative field along the b-axis and then returning to positive field values) . To image the domain wall, we subsequently apply an external field of $|B_{\text{ext}}| = 190$ mT along the NV axis ($\phi = 340°$, $\theta = 53°$) to flip the bilayer in its FM configuration. Afterwards, by decreasing the external magnetic field to $|B_{\text{ext}}| = 170$ mT, we observe two AFM regions in the bilayer, which are separated by a domain wall.

The domain wall extends horizontally across the entire bilayer CrSBr flake, starting on the right side at the monolayer interface and merges into a remaining FM bilayer section, which has the shape of a cusp, on the left side. We find the domain wall to

[2]We determined the contact point with our AFM and retracted the tip by 300 nm afterwards to scan at a fixed height, out-of-contact.

be stable over multiple days, as we were able to perform multiple scans at various fields of the same domain wall. We attribute the small stray field arising at the left edge of the bilayer flake to spins canting at the edges.

In order to gain insight into the spin configuration of the AFM domain wall and the correlation to the FM cusp, we turn to micromagnetic simulations of the flake, implemented by Dr. Boris Gross. Similarly to section 4.4.2, chapter 4, the bi- and trilayer section of the flake has been implemented in the simulations over a μm sized range to resemble the actual flake size. The 2D nature of the material was implemented by choosing a simulation mesh-grid with the height of one CrSBr layer, i.e. one cell spans over 4nm x 4nm x 0.8 nm. The intralayer (interlayer) coupling was set to FM (AFM) and a strain gradient helped stabilize the FM phase during magnetic field sweeps in the simulations. More details on the simulation can be found in the Appendix A.4.

In our simulations we find a domain wall and cusp forming in bilayer CrSBr when sweeping from high external magnetic fields along the *b*-axis of the material (B > 250 mT) to fields below the spin-flip transition. A snapshot of the magnetiza-

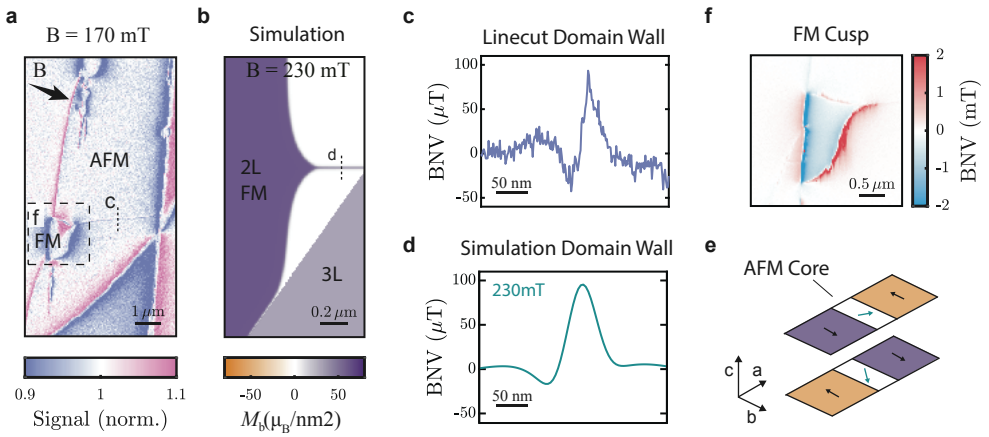

Figure 5.2.: Initialization of an AFM domain wall in bilayer CrSBr a Magnetic field image (qualitative) at $|B_{\text{ext}}| = 170$ mT showing the coexistence of an AFM domain wall and an emerging ferromagnetic region (FM) in bilayer CrSBr. **b** Simulation of the magnetization of the FM to AFM phase transition in a bi-/trilayer CrSBr flake showing the emergence of a cusp and domain wall. **c** Magnetic field linecut of the domain wall in bilayer CrSBr, location of linecut denoted as dashed line in **a**. **d** Linecut of the simulated magnetic stray field map of the domain projected onto the NV axis plotted at an NV-to-sample distance of 40 nm. Location of linecut denoted as dashed line in **b**. **e** Illustration of a domain wall in bilayer CrSBr with an AFM core, where the spins slightly tilt towards to *b*-axis as a result of lateral displacement of the domain wall rotation center within the two respective layers (see Appendix A.4.1 for more details). **f** Quantitative magnetic imaging of the FM region in bilayer, indicated with dashed box in **a**, revealing the shape of a cusp merging into the AFM domain wall.

tion at $B_{\text{ext}} = 230$ mT is plotted in Fig. 5.2b. Comparable to our measurements, a domain wall forms along the *b*-axis in the AFM bilayer section and merges into a FM cusp. Comparing a linecut of the measured magnetic stray field of the AFM domain wall, Fig. 5.2c, with a linecut extracted from the simulated stray field, Fig. 5.2d (see Appendix A.4 for full data set), yields qualitative agreement: the measured stray field is about ~ 140 μT, which is comparable to the stray field of ~ 110 μT from the simulation, when assuming a NV-to-sample distance of 40 nm. The discrepancy of $\sim$50 mT between the external field of the simulation and the one of the experiment stems from the fact, that the spin-flip field in the simulation depends on the input interlayer exchange values, which could be slightly adapted in future simulation series to better match our measured fields.

The spin configuration within the AFM domain core, which leads to the simulated stray field plotted in Fig. 5.2d, can be extracted from the simulations (see Appendix A.4) and is illustrated in Fig. 5.2e. From the simulation we find that our experimentally measured stray field profile fits best to an AFM domain wall with an AFM core, where the spin cores in the respective CrSBr layers are laterally displaced by a few nm, which leads to a measurable stay field on top of the domain wall, as illustrated with the teal arrows in Fig. 5.2e. Such lateral displacement could result from differential magnetic "pressure", wanting to maximize the regions of spins aligned with the external magnetic field along the *b*-axis. This would manifest in a dependence of the domain wall stray field strength as a function of externally applied field, which indeed can be reproduced with a simple toy model, see Fig. A.6 and section below.

We implement a toy model simulation where we construct a simplified bilayer flake with two opposite AFM regions split by an artificially imposed domain wall with either FM or AFM core, see Appendix A.4 for more details. We then let the simulation minimize the energy and assess the final spin arrangement which evolved within the different domains. For an FM (AFM) domain wall core, see Fig. A.6 for an illustration, in zero external bias field we find a stray field of ~ 450 μT (~ 12 μT) and for an AFM core with the presence of an external field (hence the spins will tilt towards the direction of the external magnetic field when rotating in the domain wall) the corresponding stray field is ~ 65 μT (all values extracted at 40 nm height). Though based on a very simplified system, these findings further support the likelihood of an AFM core with displaced cores in the respective CrSBr layers, being the internal structure of our observed AFM domain wall, as the corresponding stray field strength qualitatively matches our measurement of ~ 110 μT best.

From our experiments we find that another signature of the presence of an AFM domain wall is the creation of a "cusp" in the FM region during the FM-to-AFM spin-flip transition, which merges into the domain, see Fig. 5.2f. By creating two AFM regions separated by an AFM domain wall, the remaining FM bilayer forms into a cusp-like shape, with the pointy end merging into the domain wall. By in(de)-creasing the external magnetic field the FM region around the cusp grows (shrinks) accordingly. Whereas the cusp itself is stable over multiple hours to days in our experimental setup, its boundary is slightly changing with every scan line, visible as small strikes in the bottom right edge of the cusp. This could be attributed to laser induced dragging [151] of the phase boundary when scanning, as the effect predominantly appears along the fast scanning axis. The shape of the cusp possibly

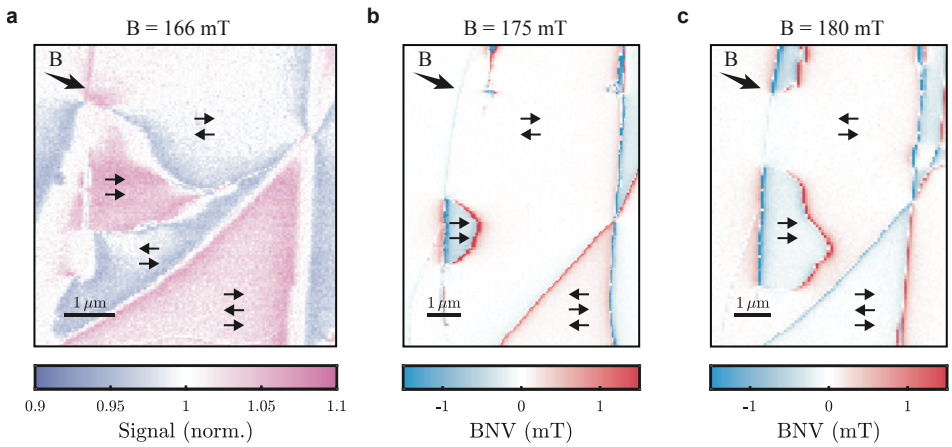

Figure 5.3.: Different FM puddle morphologies a Magnetic field image (qualitative) at $|B_{\mathrm{ext}}| = 166$ mT showing the formation of a cusp in the FM puddle merging into an AFM domain wall. Possible spin configuration of the individual CrSBr layers is denoted with black arrows. **b** Quantitative magnetic field image of a FM puddle forming in the absence of an AFM domain wall in bilayer CrSBr at $|B_{\mathrm{ext}}| = 175$ mT. **c** Same as **b** but recorded at $|B_{\mathrm{ext}}| = 180$ mT and with the trilayer having the same orientation as the the adjacent monolayer flake.

results from energetics between the domain wall and the FM/AFM phase boundary and remains to be studied in more depth.

When transitioning from the bilayer FM ordered state through the spin-flip into the AFM ordered state by reducing the external magnetic fields, the remaining FM region can appear in two different morphologies: either as a cusp connected to an AFM domain wall, Fig. 5.3a, or as an FM puddle with smooth boundaries in absence of an AFM domain wall, Fig. 5.3b,c. The creation of the FM puddles is independent on the relative orientation of the trilayer to the monolayer, compare Fig. 5.3b,c. However, the magnetic configuration of the trilayer with respect to the bilayer determines if an AFM domain wall is induced, which ultimately has an influence on the morphology of the FM region during the spin-flip transition. Our assumption is that in case of the bottom two layers of the trilayer region sharing the same, uniform spin configuration as the bilayer, no AFM domain walls are initialized and during the spin-flip transition the FM region shapes into a puddle with smooth boundaries. In contrast, if the trilayer is oriented opposite to the bilayer spin configuration in the top part of the flake (it is not clear yet, what pins the top part of the bilayer flake into certain spin configuration), we initialize an AFM domain wall in bilayer. In this case, the FM region forming during the spin-flip transition preferentially nucleates into the domain wall and exhibits a cusp.

Understanding the link between the AFM domain wall generation and morphology of the associated FM region during the spin-flip transition will ultimately give insight into the local spin configuration of the system. However, further theoretical and experimental work will be required to confirm this hypothesis.

5.2.3. Reproducibility of domain wall formation in bilayer CrSBr

To differentiate between the observation of an AFM domain wall versus any kind of defect within the spin lattice, such as a chain of spins canting along a prefixed defect line within the sample, we show the generation of various, spatially independent domain walls in bilayer CrSBr in this section.

An illustration of the domain wall and corresponding FM cusp is shown in Fig. 5.4a. For every measurement run the trilayer region is polarized with an opposite spin configuration with respect to the top region of the bilayer flake (see black arrows denoting the spin configuration in illustration Fig. 5.4a). This configuration either naturally occurs after zero-field cooling or is enforced by applying a large enough field to flip the trilayer into an opposite configuration. For the data presented in Fig. 5.4b, we first polarize the trilayer in a negative field roughly along the b-axis of the crystal and subsequently apply a positive field large enough ($B_{\text{ext}} \sim 200$ mT) to reset the bilayer in its FM state. The difference in spin-configuration within the trilayer and

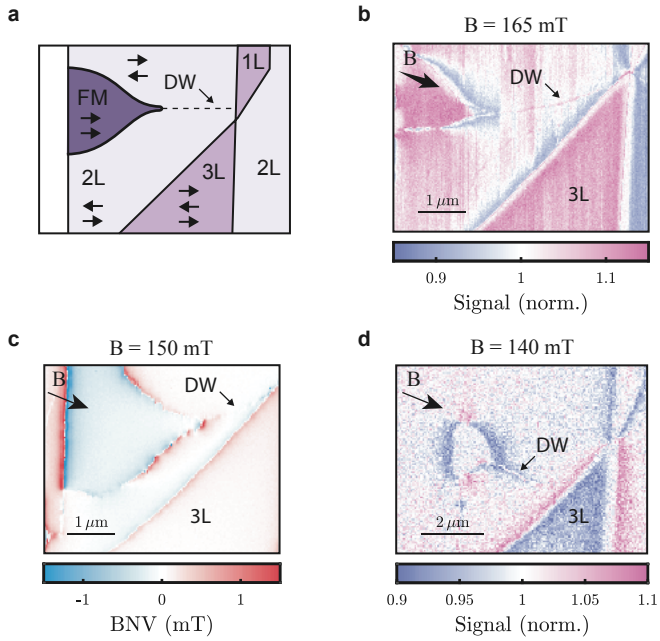

Figure 5.4.: Independent events of AFM domain wall creation in bilayer CrSBr. **a** Schematic of the coexistence of a domain wall (dashed line) and FM cusp region (dark purple) in bilayer CrSBr. Adjacent flake regions consist of mono- and trilayer CrSBr. **b** Magnetic image (qualitative) at $|B_{\text{ext}}| = 165$ mT showing the emergence of a DW and an associated FM cusp region forming in bilayer CrSBr. This data set was recorded with an NV oriented roughly along the b-axis and slightly out of plane ($\phi = 340°$, $\theta = 53°$). **c** Independent, quantitative magnetic field image of a domain wall and cusp at $|B_{\text{ext}}| = 150$ mT and similarly in **d** at $|B_{\text{ext}}| = 140$ mT (qualitative). Data sets in **c,d** were recorded with an in-plane NV ($\phi = 354°$, $\theta = 82°$).

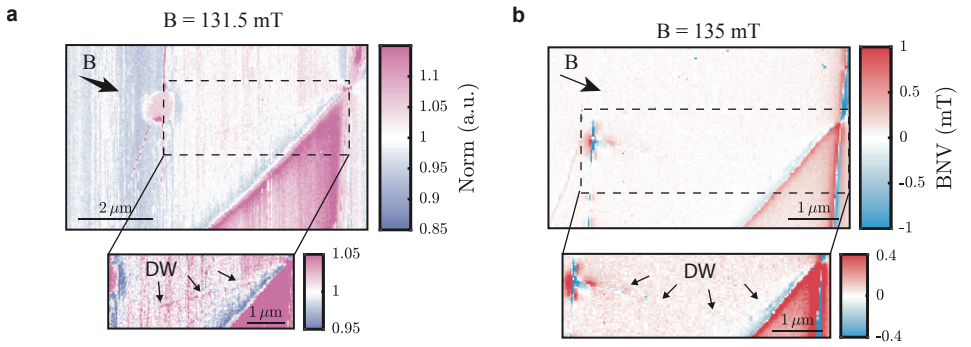

Figure 5.5.: Domain wall imaging below the spin flip transition a Magnetic image (qualitative) of the domain wall crossing the entire bilayer section at $|B_{\text{ext}}| = 131.5$ mT (NV orientation: $\phi = 340°$, $\theta = 53°$). **b** Independent, quantitative magnetic scan of the domain wall at $|B_{\text{ext}}| = 135$ mT recorded with an in-plane NV ($\phi = 354°$, $\theta = 82°$).

bilayer leads to the formation of an AFM domain wall. As previously observed, by reducing the external field thereafter, a FM region with a cusp shape merges into the domain wall in the FM-AFM spin-flip transition, as shown in Fig. 5.4b.

The FM cusp and associated FM region reduces (grows) with decreasing (increasing) external magnetic field, and always forms around the AFM domain wall, which possibly acts as an energetically favorably nucleation point for the FM region, as shown in Fig. 5.4c,d. Additionally, the initialization of the domain wall occurs for external fields aligned along an NV-axis with an out of plane component ($\phi = 340°$, $\theta = 53°$, where ϕ is measured from the positive b-axis and θ is measured from the c-axis), as well as for fields along NVs pointing in-plane ($\phi = 354°$, $\theta = 82°$), see Fig. 5.4c,d. We can therefore conclude that our observation of the domain wall is independent of an out-of-plane field induced when measuring with a NV axis pointing out of plane ($\theta = 53°$).

We are also able to image the domain wall extending over the entirety of the bilayer flake by reducing the external field further to $B_{\text{ext}} \sim 130$ mT, as shown in Fig. 5.5. Since the magnetic signal from the domain wall itself is smaller (x 2.5) compared to the magnetic signal originating from the CrSBr layer magnetization, for clarity, the domain wall region is plotted with a smaller magnetic signal range as an inset in both figures. Again, the domain wall is initialized over the entire bilayer flake independently of the out-of-plane field component being aligned at 53° away from the c-axis (Fig. 5.5a) versus almost completely in plane at 82° away from the c-axis (Fig. 5.5b).

While the AFM domain walls form independently at various locations throughout the sample, they always intersect into the same spot on the left edge of the bilayer flake, c.f. Fig. 5.4 and Fig. 5.5. This could be explained by local inhomogeneities, making it energetically favorable for the domain to pin to the same end location within the bilayer.

We conclude that the observed stray field in our measurements is attributed to a

domain wall (and not defects) because we were able to show various, independent initializations of AFM domain walls throughout the same bilayer flake (in contrast, a chain of spins canting along defects, for example, would always nucleate at the same location within the sample). Furthermore, the observation of a FM cusp (puddle) in presence (absence) of a domain wall further strengthens the assumption of our measurements capturing the stray field of an AFM domain wall. However, since the domain wall is always pinned to the same end point at the edge of the bilayer, the effect of defects cannot be completely ruled out. Additionally, the AFM domain walls are very stable over time (multiple hours to days) and do not move by varying the direction of the applied magnetic field, making it plausible that local defects could pin the domain.

In order to probe the presence of observable defects within our sample which could affect the domain wall formation, i.e. to assess the "cleanliness" of the bilayer CrSBr flake, we turn again to high temperature imaging in the intermediate FM phase, iFM phase, of CrSBr to gain insight into local disorder. It has previously been shown that spatial variations in magnetization appear in the iFM phase, which are most likely attributed to inhomogenities from local disorder within the samples [9].

5.3. Imaging the CrSBr bilayer in the iFM regime above T_N

In the previous section we have shown the initialization of AFM domain walls in a bilayer CrSBr flake. Since we have observed that individual AFM domain walls are all pinned to the same end point at the edge of the bilayer, we want to assess the local disorder within the bilayer flake in this section. To this end, we turn to high temperature imaging of the bilayer flake to unravel potential defect sources, as explained below.

Previous work on CrSBr has shown that intralayer correlations in CrSBr exist beyond the Néel temperature [9, 114]. The nature of this so called intermediate FM regime, iFM, is still under debate: AC susceptibility measurements (Fig. 4.16) suggest a 2D-XY nature for CrSBr in the iFM regime. In the last chapter, section 4.5.2, we have shown that spatial variations in magnetization appear in the iFM region, which we attribute to local variations of intralayer coupling originating from atomic defects, strain variations or other disorder [9]. This finding in turn implies, that imaging CrSBr in the iFM regime can give insight into the local disorder - an observation that we will here exploit to assess disorder in our CrSBr bilayer sample.

In this section we image the CrSBr sample in the iFM regime to gain insight in the underlying disorder structure. We expect to be able to distinguish between individually appearing defects, which could possibly pin the AFM domain walls but not hinder its formation, and between chains of defects forming a connected line, which could lead to an observation of a stray magnetic field if spins cant along the defect line.

For all the measurements shown in this section, the CrSBr flake was zero field cooled below T_N and subsequently imaged at various temperatures and in an external magnetic field of 5 mT, applied roughly along the a-axis of the material with a small out of plane component due to the alignment with the NV axis. The temperature

in our experiments was read out by a resistivity thermal couple located below the sample holder. An offset to the actual sample temperature is to be expected, since the applied microwaves used to drive the NV leads to additional heating. We therefore assume that the actual sample temperature was several degrees warmer.

Quantitative magnetic field images of the CrSBr sample below and above T_N are shown in Fig. 5.6. At 120 K (Fig. 5.6a) the CrSBr flake magnetically orders in its AFM ground state, as to be expected for temperatures below T_N. The mono- and trilayer regions are uniformly magnetized, in this particular cool down with opposite polarity. This can be concluded from the observation of opposite stray field contributions at the monolayer and trilayer edges, i.e. the right trilayer edge has a positive stray field projection whereas the right monolayer edge generates a negative stray field projection along the NV axis. Increasing the temperature slightly above T_N[3] shows magnetic variations appearing predominantly in mono- and trilayer CrSBr, see Fig. 5.6b, consistent with the observation of varying magnetization in the iFM regime described in the last chapter, section 4.5.

Additionally, we observe a defect line in the bilayer section of the flake, which is plotted in a smaller magnetic field range for clarity in Fig. 5.6c. We indeed see a small magnetic signal associated with this defect line in our low temperature scans, see Fig. 5.4b. We attribute this stray field to spins canting along the defect line. Such defects could result from atomic discontinuities in the CrSBr structure or from structural defects/changes in the underlying Si/SiO_2 surface. It is also apparent, that on the left side of the bilayer flake some local disorder appears and acts as a strong pinning site for the AFM domain wall endpoint (c.f. Fig 5.5). In the bilayer region of observed domain formation there are no observable defect lines.

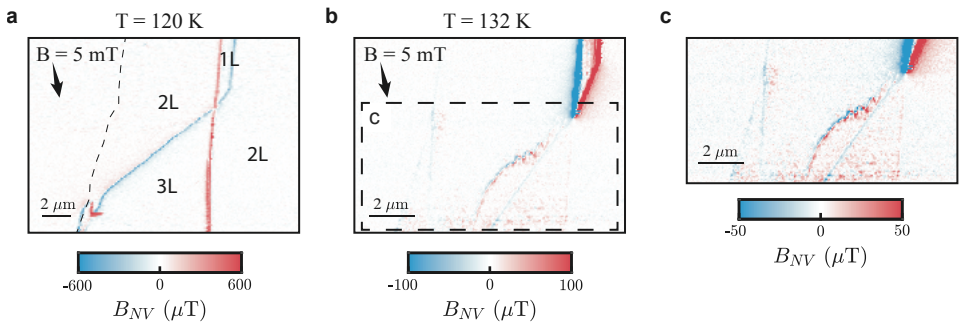

Figure 5.6.: Imaging magnetic inhomogeneities in few-layer CrSBr above T_N **a** Magnetic stray field image recorded at T=120 K in an external field of $|B_{ext}| =$ 5 mT roughly aligned along the intermediate (*a*-axis) of the material. **b** Magnetic imaging at $T \geq 132$ K revealing magnetic texture in the stray field close to and within trilayer CrSBr. **c** Same as **b** but plotted with a smaller magnetic field range to highlight features with stray fields below 50 mT.

[3]The recorded temperature for this scan is 132 K, but due to the microwave heating we expect the actual sample temperature to be several degrees warmer.

We conclude that the magnetic signal of the observed magnetic features extending mostly along the *b*-axis (see Sect. 5.2), which we attributed to domain walls, do not correlate with any observable disorder in the corresponding regime. There is still the possibility that local defects, which are below our detection limit, are pinning the AFM domain wall, such as the local disorder observed near the bilayer edge, which acts as a pinning site of the AFM domain wall endpoint.

5.4. Conclusion and Outlook

In this chapter we have shown the initialization of AFM domain walls in bilayer CrSBr. One signature of the creation of an AFM domain wall is the observation of a FM cusp shaped region which forms in the FM-to-AFM spin-flip transition. Our results show that the FM region appears in two morphologies: a cusp feature merging into an AFM domain wall or a FM puddle with smooth edges in the absence of AFM domain walls, consistent with the notion of presence (absence) of different (same) spin configuration within the bilayer flake. Comparing our experimental findings to micromagnetic simulations suggests that the observed domain wall consists of an AFM core, where the spins in the two CrSBr layers couple AFM but their rotation is slightly shifted with respect to each other and hence the domain wall exhibits a measurable stay field.

Studying the interface between the FM region of the FM-to-AFM spin flip transition and the trilayer flake could give insight into the spin configuration of the system: in the presence of different AFM spin configuration within the bilayer, there would be a spin mismatch at the interface of the bilayer to the trilayer flake on one side of the domain. It would be worthwhile to image this boundary, as its geometric shape could depend on the energy cost required to align (anti-align) the spins at the interface. In contrast, in the absence of AFM domains and under the assumption of a uniform spin configuration within the bilayer, the interface between FM bilayer CrSBr and trilayer is expected to show the same spin orientation to minimize the energy required to align the spins, which might create a distinguishable boundary shape to the anti-aligned case.

It still remains to be determined what causes the bilayer flake to split up into different AFM configurations. In our experiments, we initialized the domain via the control of the spin orientation between the trilayer and bilayer flake. Micromagnetic simulations, however, suggest the presence of AFM domain walls in isolated bilayer flakes with no neighboring layers. Since CrSBr can naturally exfoliate into isolated bilayer pieces, a follow up measurement would include to image spin textures in such samples and verify the presence (or absence) of AFM domain walls and examine the FM puddle morphologies in the FM-to-AFM spin-flip transition.

It is important to distinguish between the observation of an actual AFM domain wall versus a defect line with canted spins, since both features can lead to a measurable magnetic signature but imply profoundly different physics. By imaging multiple, spatially varying magnetic field lines within the bilayer CrSBr, which always correlate to the presence of a FM cusp region, we have strong evidence of assigning our observation to an AFM domain wall rather than just a line of defects. This statement could be reinforced by successful manipulation of the spin configuration within the

core of the domain wall. Our toy model simulations (Appendix A.4) show that by applying a field of $\sim$ 300 mT along the a-axis of the material upon the creation of the domain wall, the magnetic domain wall core will flip from a tilted AFM configuration to a completely FM core with alignment along the a-axis. Such a change of spin configuration will also alter the corresponding magnetic stray field. Since the simulations suggest that the domain wall remains stable upon lowering the external magnetic field, even below to spin-flip transition, our scanning NV magnetometer experiments should allow for the detection of different domain core formations. First, the AFM domain would need to be initialized and imaged by applying an external field along an NV with ϕ aligned along the b-axis of the material. Second, the spins within the domain would be flipped to $\pm$ along the a-axis, by changing the direction of the external applied field[4]. Afterwards, the external field can be re-aligned with the NV axis and decreased to any field suitable for measuring with the NV center. If indeed the core of the domain wall can be manipulated we would expect to see an increase in magnetic stray field for a FM domain wall core versus an AFM core and the sign should depend on the polarity of the external field.

Our results mark one of the first realization and observation of AFM domain walls in atomically thin vdW magnets. With our experiments we ultimately gain insight into the spin configuration of individual CrSBr layers and domain wall cores. These findings will help pave the way for spintronics applications based on AFM domain walls in vdW structures.

[4]From our simulations we conclude that a field of $\sim$ 300 mT along the a-axis is sufficient to flip the spins within the domain wall into a FM configuration. This field value is well below the field required to flip the entire bilayer flake by progressively canting the spins to point along the a-axis ($\sim$ 1 T [121]) and should hence only have a measurable effect on the spins within the domain wall.

Cryogenic lab © Märta Tschudin

6

6. Summary and Outlook

In this thesis, we explore the fundamental properties of 2D magnets using a quantum sensor based on single spins in diamond for nanoscale magnetic imaging. The study of magnetism in low dimensions is key for advancing applications based on these 2D magnets, which form promising building blocks for spintronics and quantum computing technologies. In our experiments we observe magnetic order in 2D magnets down to the monolayer limit and gain valuable insight into different magnetic phases.

Such 2D, vdW magnets are a newly discovered material class that have generated significant interest for their potential as a novel, atomic scale platform to host interesting magnetic phases and spin textures [2, 3]. The properties of atomically thin vdW materials show distinct features, not present in their bulk counterparts, which make them interesting for exploring novel, fundamental physics. The ability to combine various vdW materials into new heterostructures with atomically clean interfaces opens up avenues for generating unlimited combinations of novel materials with specifically, engineered properties. Furthermore, the twist degree of freedom between combined sheets of 2D materials allows for the creation of moiré phases, which has already led to groundbreaking novel discoveries in condensed matter physics [32–34] and will continue to offer a rich playground for exploring exotic phases in 2D systems.

Studying magnetism in vdW magnets requires precise measurement tools compatible with low temperatures down to a few K, as most of the currently discovered 2D magnets only exhibit long range magnetic order at cryogenic condition. In this thesis, we use single spin NV magnetometry, a powerful, non-invasive measurement technique with high spatial resolution (< 50 nm [16]), great sensitivity ($\mu\mathrm{T}/\sqrt{\mathrm{Hz}}$ [17]), and compatibility with cryogenic temperatures [152]. In scanning NV magnetometry, the spin dependent fluorescence from an atomic defect, the Nitrogen-Vacancy center, is captured to measure local magnetic fields due to Zeeman splitting [15]. The NV center is embedded in the tip of an all-diamond scanning probe and can be brought into close contact to a sample for nanoscale magnetic imaging.

We apply scanning NV magnetometry to study magnetism in the 2D magnet family of the chromium-trihalides CrX_3 (X = {I, Br, Cl}). With our sensing technique we achieve the first, quantitative study of AFM magnetic order in few-layer CrI_3 [14]. We consistently observe a magnetization for odd layered flakes, which is comparable to the magnetization of one fully polarized flake. We try to induce and image magnetic domain propagation in trilayer CrI_3. While we are able to flip half of the trilayer flake into an opposing magnetic configuration by applying an external field along the easy-anisotropy axis, z-axis of CrI_3, it is not possible to detect any domain wall propagation and we hypothesize that the trilayer flake has significant structural defects acting as a strong pinning site for the magnetization. The observation of phase wall propagation therefore remains to be explored. In CrX_3 the magnetic coupling is connected to the structural order of the material. This effect can be exploited to create magnetic moiré patterns: by twisting two CrX_3 layers with respect to each other,

local modulation in the interlayer coupling (FM versus AFM) are created due to the changes in stacking order, which forms a magnetic moiré. Such moirés have thus far been imaged directly in CrI_3 using single spin magnetometry [11] and globally using widefield NV magnetometry [12]. Here, we show our efforts towards imaging magnetic moirés in 2D $CrBr_3$ (3L + 3L, 5L) and $CrCl_3$ (twisted monolayers). While we do register a distinct variation in magnetization in the twisted areas of both samples, we are unable to extract meaningful moiré parameters from our measurements, as our magnetic signal is noisy and the material is prone to defects, disrupting any potential moiré. Furthermore, the unstable nature of the CrX_3 makes repetitive measurements on these systems difficult because they risk degrading, even if encapsulated[1]. We conclude that it is difficult to disentangle magnetic moiré signatures from local defects in thin CrX_3 devices and that it is challenging to realize long range magnetic moiré patterns ($> \mu$ms) in CrX_3 due to their structural and magnetic defects and inherent instability.

We therefore turn our studies to a novel 2D magnet with promising air-stability: AFM ordered CrSBr. We employ single spin NV magnetometry to assess the magnetism in CrSBr and find remarkably homogeneous magnetization down to monolayer flakes [9]. Additionally, our measurements confirm magnetic stability for both encapsulated and non-encapsulated flakes below the critical temperature of CrSBr. Furthermore, we study the spin-flip transition in bilayer CrSBr by applying an external field along the easy-anisotropy axis of CrSBr, the in-plane *b*-axis, which flips the spins from AFM to FM order with increasing external field. We find this spin-flip transition to be accompanied by the nucleation and propagation of a phase-wall through the sample, counter to all spins canting simultaneously. Comparing our results to micromagnetic simulations shows that a local variation in interlayer exchange coupling, possibly due to strain, helps stabilize the phase wall in this system. We then move on to image atomically thin CrSBr in the high temperature regime, near the critical temperature T_N=132 K. We find a reduction in anisotropy close to T_N and image local magnetization variation in odd-layered flakes in a temperature window slightly above T_N. The origin of this magnetic pattern is attributed to local inhomogeneities resulting from changes in intralayer coupling, which would mask features of a 2D-XY phase, predicted to appear in CrSBr at higher temperatures. We conclude that due to the air-stability and robust magnetization of CrSBr below the critical temperature, this materials forms a great platform for studying spin textures and offers potential interesting functionalities for novel technologies in the context of spintronics.

In the remaining part of this thesis, we investigate spin textures in few layer CrSBr and unravel the existence of AFM domain walls. The study of AFM domain walls is relevant for spintronics applications due to their robustness against magnetic perturbations. However, to date, the observation of AFM domain walls in atomically thin vdW materials remains largely unexplored. Using single spin NV magnetometry we image the initialization of AFM domain wall formation in bilayer CrSBr and characterize the magnetic configuration of the underlying flakes. By comparing our measurements to micromagnetic simulations, we conclude that the most likely spin texture within the domain wall core is of an AFM nature, where the domain cores

[1] In principle, a perfect encapsulation protects the magnetic material from degradation. However, in practice many contaminants are introduced during stacking and any imperfection in the encapsulation leads to degrading.

within the two bilayer flakes are slightly shifted with respect to each other. This local shift of the spin rotation centers leads to a measurable magnetic stray field on top of the AFM domain wall. We can decouple the observation of an AFM domain wall with signals arising from possible defects present in the sample, by demonstrating the repetitive initialization of various AFM domain walls throughout different locations within a bilayer sample and by imaging the flake in the high-temperature regime, which gives insight into local magnetic disorder [9]. Our results mark one of the first demonstrations of the detection of AFM domain walls in atomically thin 2D magnets and pave the way for developing spintronics applications based on vdW structures.

Overall, this thesis has presented nanoscale magnetic imaging studies of magnetism in 2D magnets using single spin magnetometry. Our results give insight into magnetic phases, anisotropies and spin textures, including AFM domain walls, in CrSBr, an emerging 2D magnet with promising air-stability. Future advances in the field rely on further engineering material properties in 2D magnets and combining different sensing techniques to map out the entire phase space of magnetism in vdW materials.

Outlook

Future advances in the field of 2D magnets rely on the fabrication of defect-free materials, which allow for the generation of clean, magnetic phases in such systems.

One promising route is the fabrication of 2D magnets samples under ultra high vacuum [106]. This technique exfoliates and stacks thin vdW material in an ultra high vacuum atmosphere, which maximally reduces contamination from the environment during fabrication. This stacking technique, however, requires a new generation of stacking stamps, since conventional polymer stacks would introduce too much contamination into an ultra high vacuum chamber. Researchers have therefore developed a cantilever based stacking procedure using silicon nitride membranes [106]. We have seen in this thesis that the material family of chromium-trihalides (CrX_3, X = {I, Br, Cl}) provides diverse physical phenomena to explore but suffers from many defects and structural disorder, possibly introduced during stacking and fabrication. Working with CrX_3 in ultra high vacuum could potentially create cleaner samples, which would be of particular interest for generating longrange magnetic moiré patterns.

Another important tuning knob for turning 2D magnets into versatile components for quantum applications is the control of magnetic coupling and anisotropy within the material. One way is designing new compositions by halogen substitution, i.e. through Cl alloying in CrSBr, which has shown that the magnetocrystalline anisotropy can be reduced and that chemical tuning of the interlayer coupling (AFM vs FM) can be achieved in such compounds [141].

In terms of future directions of employing NV magnetometry to study 2D magnets, a diverse spectrum of magnetic phases could be explored within those materials. It is for example possible to study spin waves using NV centers [153, 154]. Both the 2D magnets $CrCl_3$ [155] and CrSBr (near the critical temperature) [135] exhibit spin waves in the frequency regime close to the NV center transition frequency and are thus promising candidates for studying spin waves in the atomically thin limit. Furthermore, NV centers could give insight into skyrmionic structures and spiral spin textures in vdW materials [13, 156]. As these structures tend to emerge on

lengthscales below 50 nm, it is crucial to push the spatial resolution of scanning NV magnetometry down, which can be achieved by stabilization of shallow implanted NV centers in all-diamond scanning probes. While different imaging techniques exist to probe 2D magnetism, c.f. section 2.2.3, future advances in the field will improve by finding appropriate synergies between the individual platforms, as discussed with an example of investigating strain in the 2D magnet CrSBr below.

Strained CrSBr flakes

Here we present magnetic imaging of strained CrSBr flakes by using the complementary techniques of scanning NV magnetometry and scanning SQUID-on-lever. This section is based on unpublished data recorded in the Quantum Sensing Lab and the Poggio Lab, University of Basel, Switzerland[2]. Manuscript under preparation.

A key ingredient for turning 2D magnets into applications is gaining control over different magnetic phases. One way of achieving such control over the magnetic order is via applying in-situ strain: Recently, it has been shown that uniaxial tensile strain in CrSBr (20 nm thick) affects the interlayer exchange coupling [38], leading to FM exchange coupling at zero external bias field. In order to gain insight into the mechanism of strain induced magnetic transitions, we image strained CrSBr flakes. Strain has been applied by pushing a CrSBr flake with a graphene marker and thus bending the flake, as depicted in Fig. 6.1a and described in [157].

We employ scanning NV magnetometry to image a strained, 8 nm thick CrSBr flake, as shown in the topography image in Fig. 6.1b. Recording the magnetic stray field of the strained CrSBr flake at 4 K, in 150 mT after zero field cooling shows homogeneous magnetic order[3], with the exception of one magnetic dirt residue towards the middle of the scan area. We do not see any apparent effect of strain within this sample, possibly because the strain values are not high enough to perturb the AFM interlayer exchange coupling in the ground state. Imaging such strained devices during the spin-flip process would yield more insight into the effect of strain on the magnetization. Our scanning NV magnetometry setup is, however, limited to operations in fields below $\sim$ 300 mT, which is not enough to induce FM order in multilayer CrSBr [121]. Additionally, imaging full flakes with sizes of several μms is very time consuming and often times the flakes do not fit entirely in our maximal scan range of $15\,\mathrm{x}\,15\,\mu\mathrm{m}^2$. Therefore, we turn to scanning SQUID magnetometry of strained CrSBr flakes. We investigate a 18-layer, strained CrSBr flake, as shown in Fig. 6.1c. Using a SQUID-on-lever, in analogy to [67], we image the magnetization of the CrSBr flake as a function of increasing in-plane field along the easy-anisotropy axis (b-axis) within the material. We find that the magnetic switching from the AFM ground state to FM order is linked to the strain in the sample: as shown in Fig. 6.1d, the region with maximal

[2]NV Data recorded by M. A. Tschudin, C. Schrader and D. A. Broadway under the supervision of P. Maletinsky. Scanning SQUID data recorded by A. Vervelaki, K. Bagani, and D. Jetter under the supervision of M. Poggio. The samples described in this chapter were fabricated by A. Devarakonda under the guidance of C. Dean and X. Roy and the micromagnetic simulations were done by A. Vervelaki and B. Gross.

[3]The faint stray field lines crossing the CrSBr flake result from a thin ($\sim$3 nm) CrSBr flake which was stacked on top of the strained flake for creating a magnetic moiré. The twist angles are however too large ($> 5°$) to induce a moiré periodicity which could be resolved with scanning NV magnetometry.

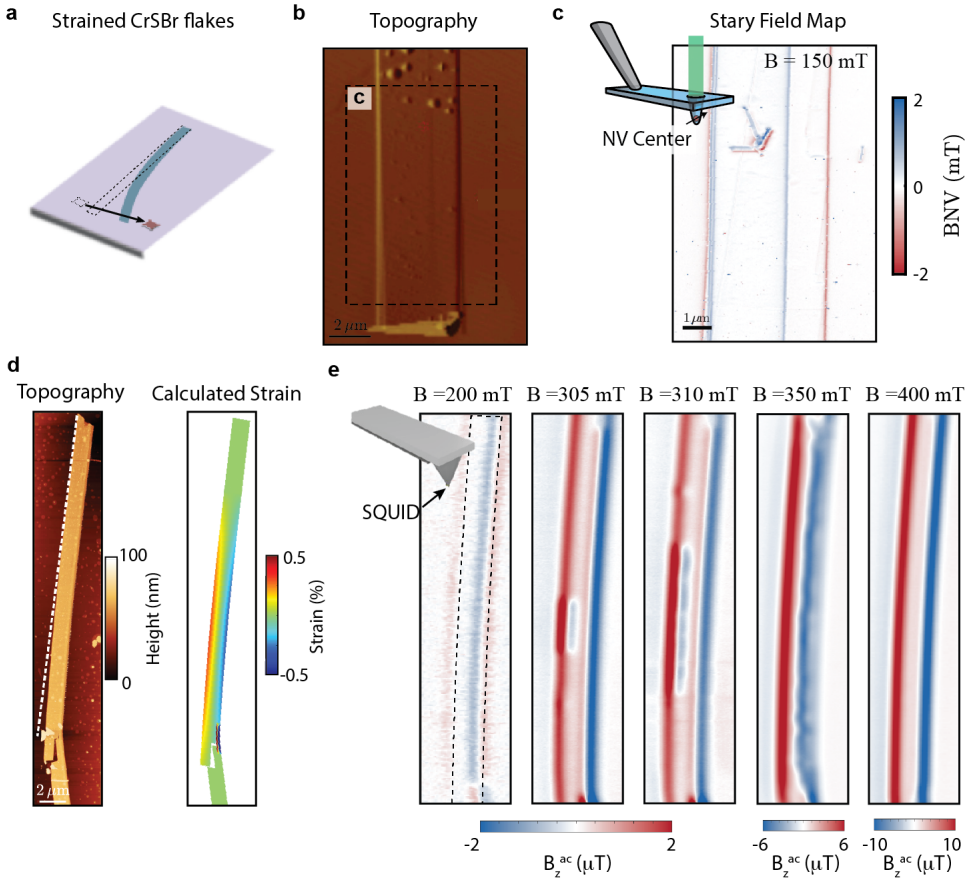

Figure 6.1.: Imaging magnetism in strained CrSBr flakes. **a** Straining CrSBr via AFM controlled bending of the flake using a graphite marker, similarly to as described in [157]. **b** Topography of a strained, 8 nm thick CrSBr flake (only bottom part of flake is shown). **c** Scanning NV magnetometry imaging of the flake in **b**, recorded at $|B_{\text{ext}}| = 150$ mT pointing roughly along the b-axis (geometrical short axis) of the flake and out of plane ($\theta_{\text{NV}} = 54°$) to align it to the NV axis. **d** Topography of a 18-layer thick CrSBr flake, strained using the same technique as depicted in **a**. The corresponding stain profile was calculated according to [157]. **e** Scanning SQUID-on-lever imaging of the flake shown in **d**, revealing a correlation between maximal strain and FM order during the spin-flip process in CrSBr. The external magnetic field is applied in-plane along the b-axis (geometrical short axis) of the flake.

strain (region of maximal bend) switches first and a phase wall progressively extends throughout the flake, similar to our observations in bilayer CrSBr, c.f. section 4.4. Eventually, all the layers flip into a FM configuration between $B = 350 - 400$ mT.

While scanning SQUID magnetometry has nicely outlined the correlation of strain and magnetic switching in multilayer CrSBr, this technique is not able to resolve the magnetic structures visible as "wiggles" in Fig. 6.1e, mainly occurring at $B = 350$ mT.

Micromagnetic simulations of this structure suggest the presence of AFM domain walls and corresponding FM cusp regions, similar to our observations of AFM domain walls in bilayer CrSBr, c.f. section 5.2. Therefore NV magnetometry can provide crucial information about underlying spin textures in such systems. This example illustrate the beneficial synergy between different sensing modes, which is required to fully map out the magnetic phases in 2D magnets.

There are various routes for combining different imaging and sensing techniques. One possibility is to combine Magneto-Optical Kerr Effect (MOKE) with scanning NV magnetometry: MOKE could allow for a fast overview scan, probing areas of different magnetic orientations, which is especially useful when studying larger 2D magnetic flakes. Additionally, the added optics could be used to probe excitons in 2D magnets [57]. Afterwards, scanning NV magnetometry can be applied to gain local, nanoscale magnetic resolution images of spin textures such as domain walls or skyrmions, which are typically below the spatial resolution of MOKE. Another possibility is the integration of an all-diamond scanning probe in a quantum twisting microscope (QTM) [158]. In such a configuration, the NV center could directly probe the local magnetic moiré of in-situ twisted stacks. Alternatively, a translucent tip, such as an all-diamond scanning probe, could be used as the base for an hBN capping layer with embedded hBN defects for sensing [159–161] in a QTM setup.

In conclusion, combining diverse imaging and sensing techniques is crucial for fully understanding and controlling the magnetic phases in 2D magnets, paving the way for advanced technological applications.

A. Appendix

A.1. NV ground state Hamiltonian and magnetization determination

Magnetic field response of NV centers
The NV's response to magnetic fields can be understood by looking at the NV's ground state Hamiltonian [15]:

$$\hat{\mathcal{H}}/h = \mathrm{D}_0\hat{\mathbf{S}}_z^2 + \gamma_{\mathrm{NV}}\boldsymbol{B}\hat{\mathbf{S}}, \tag{A.1}$$

where h is the Planck constant, D_0 is the zero field splitting between the m_s=0 and the m_s=±1 spin states (2.87 GHz), γ_{NV} = 28 MHz/mT is the gyromagnetic ratio, $\hat{\mathbf{S}}_{x,y,z}$ are the spin matrices for S = 1, and $\boldsymbol{B} = (B_x, B_y, B_z)$ denoting the magnetic field amplitudes defined by the NV coordinate system, where the z-axis corresponds to the NV symmetry axis. We neglect the contribution of the strain induced mixing of the m_s=±1 and hyperfine interactions with nuclear spins in diamond, as we typically do not resolve this in our measurements due to power broadening. Writing eq. A.1 in Matrix form yields:

$$\hat{\mathcal{H}}/h = \begin{pmatrix} \mathrm{D}_0 + \gamma_{\mathrm{NV}}B_z & \frac{\gamma_{\mathrm{NV}}}{\sqrt{2}}(B_x - iB_y) & 0 \\ \frac{\gamma_{\mathrm{NV}}}{\sqrt{2}}(B_x + iB_y) & 0 & \frac{\gamma_{\mathrm{NV}}}{\sqrt{2}}(B_x - iB_y) \\ 0 & \frac{\gamma_{\mathrm{NV}}}{\sqrt{2}}(\mathrm{B_x} + i\mathrm{B_y}) & \mathrm{D}_0 - \gamma_{\mathrm{NV}}B_z \end{pmatrix}. \tag{A.2}$$

For magnetic fields parallel to the NV axis ($B_x, B_y = 0$), the NV ODMR frequencies are linearly shifted, which leads to the Zeeman splitting of $\Delta f = 2\gamma_{\mathrm{NV}} \cdot B_z$, between the two m_s=±1 states, as stated in eq. 2.4 before. Orthogonal fields will induce spin mixing, where the m_s=0 and m_s=±1 states will no longer be good eigenstates. Such spin mixing will decrease the NV fluorescence and ODMR contrast, which makes quantitative magnetic field sensing impossible for orthogonal fields above ∼ 10 mT (however, qualitative sensing is still possible in this regime) [99]. For the measurements in this thesis we apply the external fields along the NV-axis and we operate in transient fields below 10 mT.

Magnetization determination
The magnetic stray field maps of 2D magnetic samples, recorded with our scanning NV magnetometer, can reveal information about the underlying source magnetization. While a magnetization source leads to a well defined magnetic stray field (forward problem), the inverse calculation, i.e. determining the magnetization corresponding to a given stray field map has no unique solution (reverse problem) and can thus only be solved, if certain assumptions about the system, such as the magnetization direction, are given [162]. With reconstruction methods, it is possible to link a magnetic

stray field of a 2D magnetic system map to a corresponding magnetization [79]. The magnetic field $\boldsymbol{B}(\boldsymbol{r})$ at a position $\boldsymbol{r}$ induced by a magnetization is defined as [29, 162]:

$$\boldsymbol{B}(\boldsymbol{r}) = \frac{\mu_0}{4\pi} \int_{\mathrm{d}V'} \left(\frac{3\boldsymbol{M}(\boldsymbol{r}')(\boldsymbol{r}-\boldsymbol{r}')}{|\boldsymbol{r}-\boldsymbol{r}'|^5} (\boldsymbol{r}-\boldsymbol{r}') - \frac{M(\boldsymbol{r}')}{|\boldsymbol{r}-\boldsymbol{r}'|^3} \right) \mathrm{d}V'. \tag{A.3}$$

Assuming the stray field is measured at a fixed height above a 2D magnetic source with a magnetization M pointing along θ_M away from the z-axis and φ_M within the x-y-plane, the stray field arising at the edge (x=0, magnetization y extending to infinity) is given by [14, 44]:

$$\begin{aligned} B_x &= -\frac{\mu_0 M}{2\pi} \cdot \left(\frac{z}{z^2+x^2} \cos\theta_\mathrm{M} + \frac{x}{z^2+x^2} \sin\theta_\mathrm{M} \cos\varphi_\mathrm{M} \right), \\ B_y &= 0, \\ B_z &= +\frac{\mu_0 M}{2\pi} \cdot \left(\frac{x}{z^2+x^2} \cos\theta_\mathrm{M} - \frac{z}{z^2+x^2} \sin\theta_\mathrm{M} \cos\varphi_\mathrm{M} \right). \end{aligned} \tag{A.4}$$

In scanning NV magnetometry, the measured stray field is a projection along the NV-axis:

$$B_{NV}(x,y) = \sin(\theta_{NV})\cos(\phi_{NV}) \cdot B_x + \sin(\theta_{NV})\sin(\phi_{NV}) \cdot B_y + \cos(\theta_{NV}) \cdot B_z \tag{A.5}$$

In our experiments, we determine θ_{NV} and ϕ_{NV} by iteratively sweeping the external magnetic field (vector field) along θ and ϕ and determining the maximal splitting of the two ODMR peaks (i.e maximal alignment of the external magnetic field). Assuming a certain orientation of the magnetization (for example $\theta_M = 90$ and $\varphi_M = 0$ for in plane magnetization measured along the anisotropy axis of the magnetic system) allows for fitting linecuts to the stray field profiles measured along the edge of a 2D magnetic flake, and hence determining the corresponding magnetization M.

To reconstruct the magnetization corresponding to an entire stray field map of a 2D magnetic sheet, the following correlation in Fourier space can be used (Fourier reconstruction method):

$$\boldsymbol{B}(\boldsymbol{k}) = \boldsymbol{D}(\boldsymbol{k}) \cdot \boldsymbol{M}(\boldsymbol{k}), \tag{A.6}$$

where D is the dipolar tensor [17, 153, 163]:

$$\boldsymbol{D}(\boldsymbol{k}) = \frac{\mu_0}{2} k e^{-kz} \begin{pmatrix} -\left(\frac{k_x}{k}\right)^2 & -\frac{k_x k_y}{k^2} & -i\frac{k_x}{k} \\ -\frac{k_x k_y}{k^2} & -\left(\frac{k_y}{k}\right)^2 & -i\frac{k_y}{k} \\ -i\frac{k_x}{k} & -i\frac{k_y}{k} & 1 \end{pmatrix}. \tag{A.7}$$

It is apparent from eq. A.6 that the magnetic field can be determined from a given magnetization, but the inverse problem is ill defined. However, the reconstruction of the magnetization from a stray field map is possible, if enough constraints are introduced, such as fixing the magnetization direction and applying suitable filters. The magnetization data presented in this thesis were obtained via the Fourier reconstructed method mentioned above and as described in more details in [14, 17] or via a neural network approach [134], which determines an inversion transformation matrix to produce a magnetization image from a stray field scan based on a machine learning neural network (more details can be found in the supplementary of [9]).

A.2. Experimental Setup

In this section we list details of the vdW assembly (section A.2.1) and of the low temperature scanning NV magnetometry setups (section A.2.2).

A.2.1. VdW assembly fabrication parameters

Table A.1 summarizes the optical contrast measured in our microscope for the chromium-trihalides (CrX_3) exfoliated on 90 nm Si/SiO_2. For the vdW assembly of these materials, we typically encapsulate the magnetic flakes in thin (<15 nm) graphite. The graphite flakes are exfoliated outside of the glovebox on 285 nm Si/SiO_2 wafers and then transferred into the glovebox. Before picking up the flakes for stacking inside the glovebox, the Si/SiO_2 chips containing the graphite flakes are heated on a hot plate ($\sim 120°C$) for a few min to evaporate any remaining water molecules from the surface. When picking up the CrX_3 flake, we keep the temperature below 70°C at all times to prevent the non-encapsulated flake from degrading. Once the flake is fully encapsulated in graphite (or hBN) we release the stack by melting the PC film at $\sim 160°C$.

Material	Contrast 1L (red color channel)	Contrast 2L (red color channel)
CrI_3	$7-8\,\%$	$16\,\%$
$CrBr_3$	$5\,\%$	$8-9\,\%$
$CrCl_3$	$2-3\,\%$	$5-6\,\%$

Table A.1.: Optical contrast in our microscope (100x) for CrX_3 exfoliated on 90 nm Si/SiO_2.

The sources of the 2D materials used in this thesis are summarized in table A.2 below.

Material	Source 1	Source 2
CrI_3	Dr. Enrico Giannini, University of Geneva	HQGraphene
$CrBr_3$	2Dsemiconductors	
$CrCl_3$	HQGraphene	
CrSBr	Group of Prof. Xavier Roy, Columbia University	
G	NGS Flaggy Flakes, graphit.de	

Table A.2.: Crystal sources for the 2D materials presented in this thesis.

PC transfer slides: The following recipe explains, how we fabricate the polymer stamps (PC slides) used for vdW stacking.

- take PDMS (Gel-Pak DGL-20/17-X4) and fine tip tweezers (sharp tip end)

- use fabrication wipes as surface to work on
- get PC solution[1] (6%)
- get clean micrscope holder glass slides (can clean them with acetone and IPA)
- use a plastic pipette to put a line of PC droplets on a glass slide, put another glass slide on top, slightly press down and slide off the upper glass slide
- let PC film dry[2]
- prepare new glass slides, take tape (double sided, we use scotch double sided tape) and punch a hole through the tape with a hole puncher. Put the tape with the hole centered on the top of the glass slide, cut off edges of remaining tape with a razor blade
- cut out PDMS stripes with a new, clean razor blade, put the stripe on a glass slide and cut out small squares (only use clean material!). PDMS square size: $\sim 2\,\mathrm{x}\,2\ \mathrm{mm}^2$
- Place the PDMS square on the glass slide, in the hole of the double sided tape
- Punch a hole into a new stripe of tape (single sided, we use scotch magic tape) and place it on a clean area on the PC film (hold slide against the light to clearly see clean areas)
- Press the tape down on the PC film, cut off the edges of the PC film along the tape and peel off the tape. Now you should have a thin PC film spanning across the hole in your tape.
- Place the tape with the PC film on the PDMS square: align the PC film to span across and around the entire PDMS square
- Gently press down the tape with the PC film onto the double sided tape and remove trapped air bubbles using tweezers. Be careful to keep the delicate PC film/PDMS stamp area clean and free from damage.
- Extra: in case your stamp blows up when bringing into the glovebox (during vacuum pumping), puncture the PC film next to the PDMS square with a razor blade before transferring.

A.2.2. Setup specifics

This section is adapted from the supplementary material of [9] and lists the key components of the two low temperature scanning NV magnetometry setups used to record the data presented in this thesis.

[1] Polycarbonate (PC) was dissolved in chloroform: 1.74 g of PC in 20 ml of chloroform ($\rho_{ChCl_3} = 1.49\mathrm{g/ml}$, $\mathrm{V} = 20\,\mathrm{ml}$, concentration $c = \frac{m_{PC}}{m_{ChCl_3}}$).

[2] avoid making PC slides in a dry environment because it will get too sticky. One can take a fabwipe, dip it in water and place the wet towel next to the PC films when drying to provide some extra humidity.

The magnetic images shown in this thesis were taken using two different Attocube cryostats, an attoLIQUID 1000 for measurements around $T = 4$K and an attoDRY 2200 for variable temperatures $T = 2 - 300$K measurements. The NV electronic spin is excited using a 532 nm laser (attoLiquid - Laser Quantum 532 Gem, and attoDry - Laser Quantum 532 Torus). The green laser light passes through an acousto-optical modulator (AOM), which we control via an arbitrary waveform generator (AWG) (Spectrum instrumentation DN2.663-04). The photoluminescence (PL) of the NV spin is separated using a dichoric mirror which is detected with an avalanche photodiode (Excelitas SPCM-AQRH-33). The microwave control is performed using a signal generator (attoLIQUID - SRS SG384, attoDry - Rhode Schwartz SMBV100B) and the AWG. To maintain the optical readout of the NV spin, the sample is scanned while the diamond tip remains static.

A.3. Nanomagnetism in CrSBr

A.3.1. Histograms

To determine the magnetization of the CrSBr flakes we use two separate methods: The first method is fitting the magnetic stray field of a 1D line cut across the edge of a flake and the second method is taking a histogram of the reconstructed magnetization image of a CrSBr flake. Details on the fitting routines are described in section A.1. In the following paragraph we show the histograms of the studies CrSBr used for extracting the magnetization and we summarize all the results, including all values from analytical 1D linefits in table A.3. Comparing these results shows that both methods for determining the magnetization give a similar value of magnetization for a specific layer thickness of CrSBr.

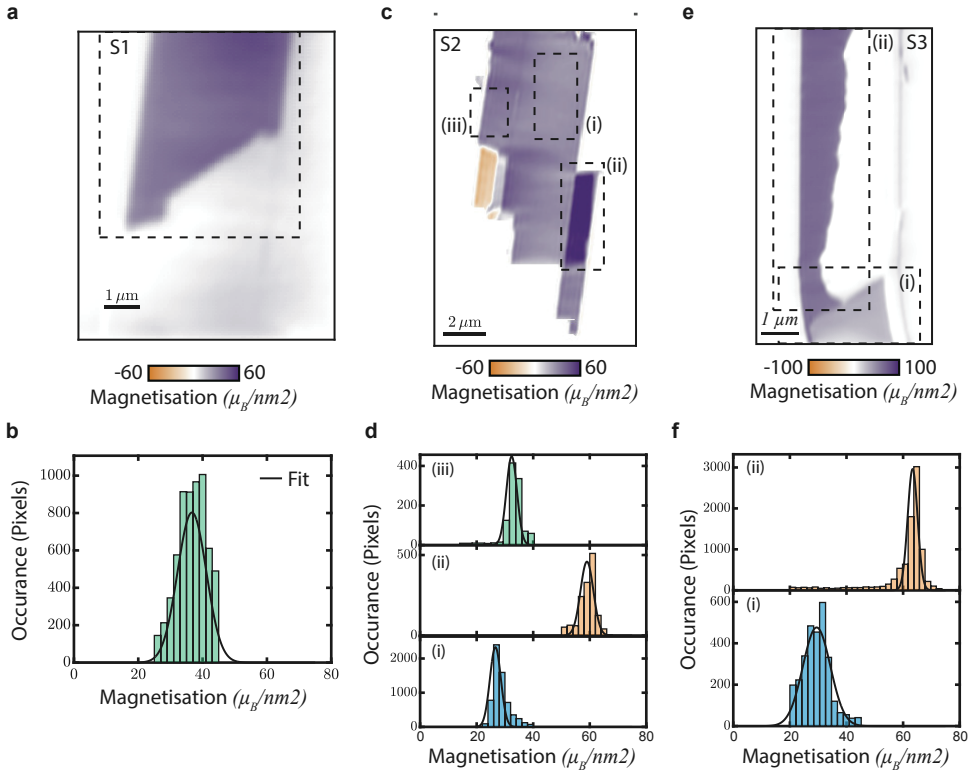

Figure A.1.: Histograms of the magnetization reconstruction for layer dependent magnetization determination. **a** Magnetization reconstruction for sample $S1_{\mathrm{Air}}$ with region for where histogram is taken. **b** Histogram from **a**, where the fit to the histogram is shown in black. **c** Magnetization reconstruction for sample $S2_{\mathrm{Encap}}$. **d** Histograms from **c**, where blue is monolayer, orange is (FM) bilayer, and green is trilayer. **e** Magnetization reconstruction for sample $S3_{\mathrm{Air}}$. **f** Histograms from **e**, where blue is monolayer and orange is (FM) bilayer.

$\#L$	Sample	State	M (μ_b/nm^2)	M/ layer	B (mT)	Height (nm)	Method
1	$S2_{\text{Encap}}$	AFM	28 ± 1	28 ± 1	150	63 ± 1	Line cut
1	$S2_{\text{Encap}}$	AFM	29 ± 2	29 ± 2	150	66 ± 4	Line cut
1	$S2_{\text{Encap}}$	AFM	28 ± 3	28 ± 3	150	70	Histogram
1	$S3_{\text{Air}}$	AFM	30 ± 1	30 ± 1	230	48 ± 2	Line cut
1	$S3_{\text{Air}}$	AFM	27 ± 2	27 ± 2	150	60	Histogram
1	$S3_{\text{Air}}$	AFM	30 ± 6	30 ± 6	230	60	Histogram
2	$S2_{\text{Encap}}$	FM	58 ± 2	29 ± 1	150	70	Line cut
2	$S2_{\text{Encap}}$	FM	58 ± 3	29 ± 1.5	150	70	Histogram
2	$S3_{\text{Air}}$	FM	64 ± 3	32 ± 1.5	180	55 ± 2	Line cut
2	$S3_{\text{Air}}$	FM	61 ± 8	30.5 ± 4	170	100	Histogram
2	$S3_{\text{Air}}$	FM	63.3 ± 0.2	31.6 ± 0.1	180	60	Histogram
2	$S3_{\text{Air}}$	FM	58 ± 7	29 ± 4	230	60	Histogram
2	$S3_{\text{Air}}$	FM	58 ± 2	29 ± 1	230	46 ± 2	Line cut
3	$S1_{\text{Air}}$	AFM	34.5 ± 0.4	34.5 ± 0.4	150	63 ± 1	Line cut
3	$S1_{\text{Air}}$	AFM	36.7 ± 0.2	36.7 ± 0.2	5	60	Histogram
3	$S2_{\text{Encap}}$	AFM	31 ± 0.7	31 ± 0.7	150	69 ± 2	Line cut
3	$S2_{\text{Encap}}$	AFM	33 ± 3	33 ± 3	150	70	Histogram
3	$S2_{\text{Encap}}$	FM	98 ± 5	33 ± 2	300	73 ± 5	Line cut
5	$S3_{\text{Air}}$	AFM	37 ± 3	37 ± 3	172.5	111 ± 10	Line cut
5	$S3_{\text{Air}}$	AFM	38 ± 3	38 ± 3	170	100	Histogram
5	$S3_{\text{Air}}$	AFM	37 ± 2	37 ± 2	160	100	Histogram

Table A.3.: Measurements of the magnetization of different layer thicknesses at a temperature of approximately 4 K. Blue color highlights data points used in Fig. 4.4c.

A.3.2. FM to AFM spin-flip

A full Iso-B imaging series of the phase wall movement in bilayer CrSBr is shown below.

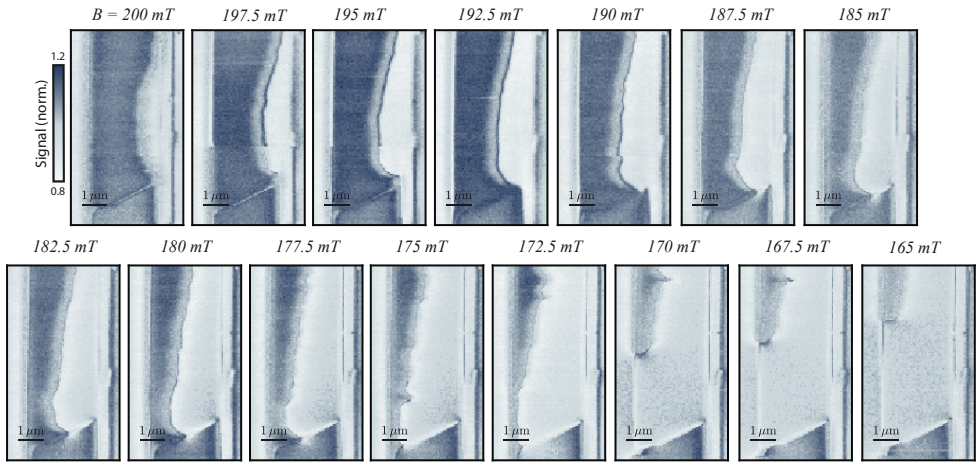

Figure A.2.: Measurement series of phase wall movement through bilayer CrSBr going from high field (200 mT) to low field (165 mT). Measurements were taken with single point "Iso-B" imaging, method described in Section 2.3.2.

A.3.3. Magnetization reconstruction at different temperatures

The results from the magnetization reconstruction using a neural network approach, implemented by Dr. David Broadway, are shown below.

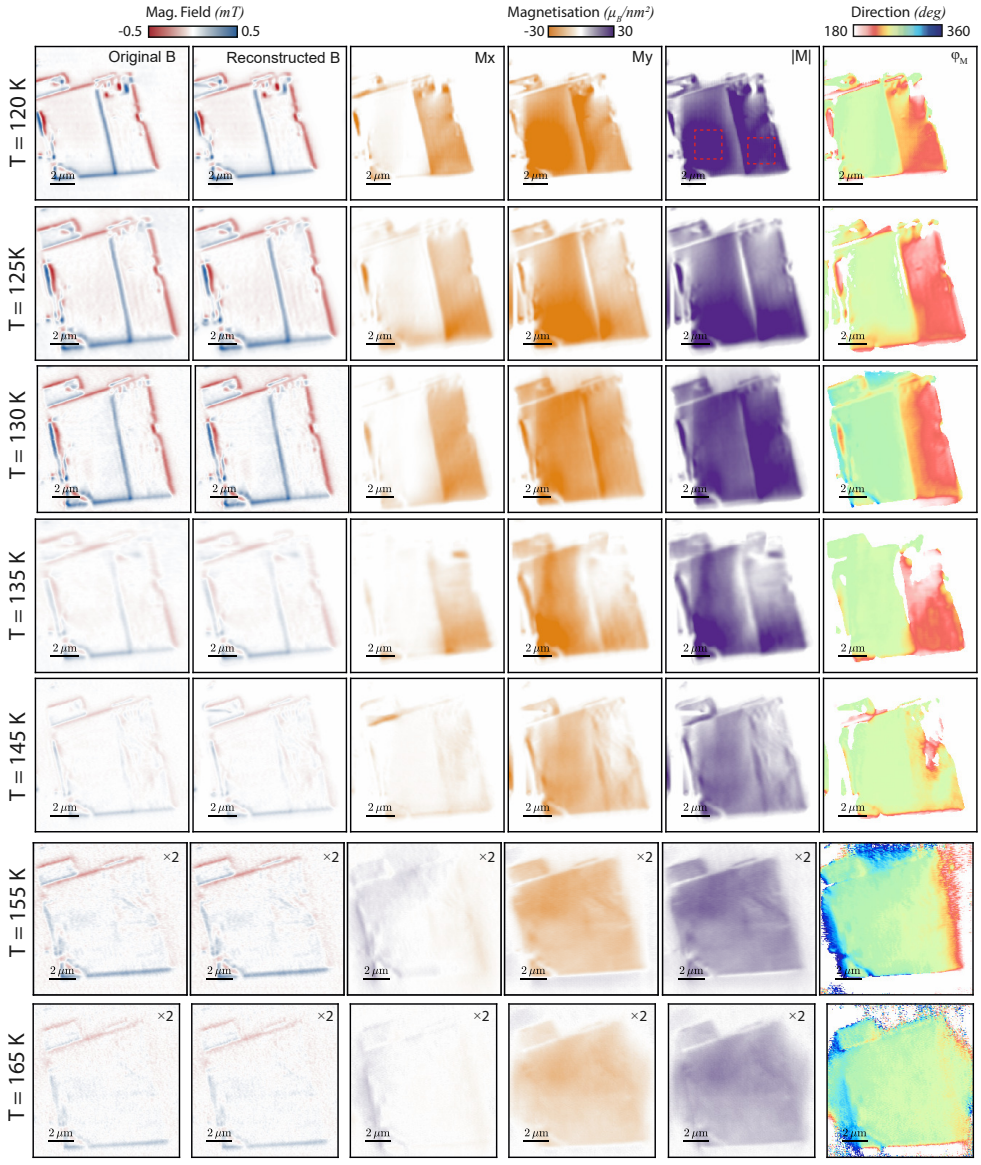

Figure A.3.: Magnetization reconstruction of all the magnetic images taken at different temperatures from Fig.4.9. The panels from left to right are: The original magnetic field, the reconstructed magnetic field by the neural network, the magnetization along the X-direction of the image, the magnetization along the Y-direction of the image, the magnitude of the magnetization, and the direction of the magnetization. The bottom two rows have the data multiplied by two to make the data visible.

A.3.4. Magnetic structure of different CrSBr flakes near T_c

We performed a smaller temperature scan on Sample $S1_{\text{Air}}$, over a region containing both a bi- and trilayer. At $T = 4K$ and low applied magnetic fields, the bilayer was observed to be perfectly AFM, with no observable stray magnetic field, while the trilayer was uniformly magnetized over regions of 10s of microns, shown in Fig. A.4**a**. When heated to near the Néel Temperature ($T = 130K \approx T_N$) the trilayer showed evidence of spontaneous reordering of the magnetization direction. This is observed in the small red section of the left hand side in Fig. A.4**b**. The change in magnetic field direction indicates that for a few lines (image taken by scanning with a faster horizontal axis and a slow vertical axis) the magnetization direction had flipped. We also observed for a previous smaller scan at the same temperature that the magnetization direction was opposite to the scan shown in **b**. We suggest that the system was close enough to the Néel temperature that small local perturbations in temperature may have resulted in a flipping of the magnetization direction through heating above T_N and then cooling back down.

By increasing the temperature further to above the Néel Temperature ($T = 140$ K), we observed the bi-layer to become weakly FM, which results in a small stray field even for weak applied magnetic fields. While the trilayer became significantly weaker in strength and formed small magnetic textures similar to the samples discussed in section 4.5.2.

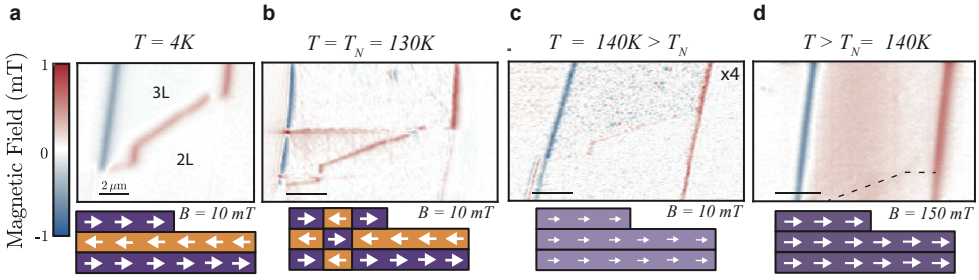

Figure A.4.: Temperature series for tri- and bilayer flake. **a** Magnetic image at $T = 120K$ with trilayer in the FM state and the bilayer in the AFM state. The rough state of the material is illustrated below the image. **b** Magnetic image at $T = 130K \approx T_N$ showing the same state as in **a** except for one region that had the opposite sign. This was concluded to be a short term flip of the entire flake rather than a local domain, see text for details. **c** Magnetic image at $T = 140K$ where both regions are in the FM state but now have zero remnant field, resulting in a reduced field strength. **d** Magnetic image at $T = 140K$ measured at a higher field $B = 150mT$ which magnetizes the layers to a similar strength to before the Néel temperature. All measurements are performed with a magnetic field pointing approximately along the CrSBr b-axis with a small $\sim 30°$ out of plane component.

A.3.5. Micromagnetic simulations of CrSBr

We employ computational micromagnetic simulations [129–131] to investigate the formation of AFM-FM phase boundaries. To do so, we simulate the fraction of the

CrSBr flake that has been imaged using the scanning NV magnetometer and is shown in Fig. 4.7.

To estimate material parameters, we consider a 200 nm x 200 nm x 200 nm simulation volume with periodic boundary conditions in all three dimensions, representing a bulk CrSBr crystal. The corresponding cell sizes are 4 nm x 4 nm x 0.8 nm, respectively. As a starting point, the in-plane exchange stiffness is estimated by $A_{ex,xy} \approx k_B T_c/(2(a+b)/2) = 2.35\,\mathrm{pJ/m}$ [164] using $a = 0.350\,43\,\mathrm{nm}$, $b = 0.473\,79\,\mathrm{nm}$, and $T_c = 140\,\mathrm{K}$. The saturation magnetization is set to its bulk value of $M_{sat} \approx 36\ \mu_B/\mathrm{nm}^2$. Then, interlayer exchange coupling and strength of crystalline anisotropy axes (a and b axes of the material) are estimated in an iterative process: The relative strength of the two uniaxial crystalline easy anisotropy axes is taken from Fig. 4.13b, and interlayer exchange coupling $A_{ex,z}$ is known to be negative and small compared to $A_{ex,xy}$. With this input these three parameters are adjusted until the bulk values for the saturation fields along the main crystal axes and the spin-flip field [117, 121, 122] are roughly matched. This leads to $K_a = 106\,098\,\mathrm{J/m}^3$, $K_b = 40\,244\,\mathrm{J/m}^3$, and $A_{ex,z} = -0.008 \cdot A_{ex,xy}$.

For the simulations of the flake we use black and white images of each layer that are deduced from optical images of the flake as geometry. The finite element mesh is set to a size of 825 x 2525 x 6 cells with corresponding cell sizes of 4 nm x 4 nm x 0.8 nm, respectively.

An x (along b-axis) gradient in $A_{ex,z}$ of about 1.25 aJ/m/nm is introduced to the simulation, which facilitates gradual movement of the AFM/FM phase boundary through the flake with external field. This corresponds to $A_{ex,z} = -0.008 \cdot A_{ex,xy}$ on the left hand side and $A_{ex,z} = -0.0105 \cdot A_{ex,xy}$ right hand side of the flake. Further, a small 'defect' in the top left corner of the flake, namely a spot with positive $A_{ex,z}$, serves as nucleation point for the FM domain.

The saturation magnetization is set to our measured value $M_{sat} \approx 30\ \mu_B/\mathrm{nm}^2$, and $A_{ex,xy} = 1.75\,\mathrm{pJ/m}$ is adjusted in an other iterative process to match the field range of phase boundary movement, while the gradient field of $A_{ex,z}$ is kept at constant relative value.

Unlike in experiment, the simulated phase boundary is perfectly vertical, except if in proximity to an edge of the sample. This is owed to the perfect orientation of the gradient in $A_{ex,z}$ with x. We have tested diagonal gradients leading to diagonal boundary orientations, implying that the irregular boundary in the experiment may originate in an equally irregular gradient in $A_{ex,z}$.

A.4. AFM Domain Walls in Bilayer CrSBr

We turn to micromagnetic simulations to study the internal spin structure of horizontal AFM domains in bilayer CrSBr. The simulations have been conducted by Dr. Boris Gross. The material parameters and setting of the CrSBr unitcell is identical to the simulations described in A.3.5. In this section we discuss two different simulation sets: First, we discuss the stray field emerging from an AFM domain wall in a bilayer CrSBr flake, which has been imaged using the scanning NV magnetometer (Fig. 5.2). Afterwards, we show simulations of a simplified CrSBr bilayer geometry to assess the difference in magnetic stray field arising for different domain core formations (FM versus AFM).

A.4.1. Simulations AFM domain wall in bilayer CrSBr

The reconstructed magnetic stray field corresponding to the simulated magnetization map of the bi-/trilayer CrSBr flake shown in Fig. 5.2b is plotted in Fig.A.5a.

The stray field is projected along the NV-axis ($\phi = 340°$, $\theta = 53°$) and calculated at 40 nm above the sample. A linecut of the AFM domain wall stray field is plotted in Fig.A.5. Note that this is the same linecut as shown in Fig. 5.2d, plotted on a larger x-range. To minimize the background introduced by the trilayer stray field,

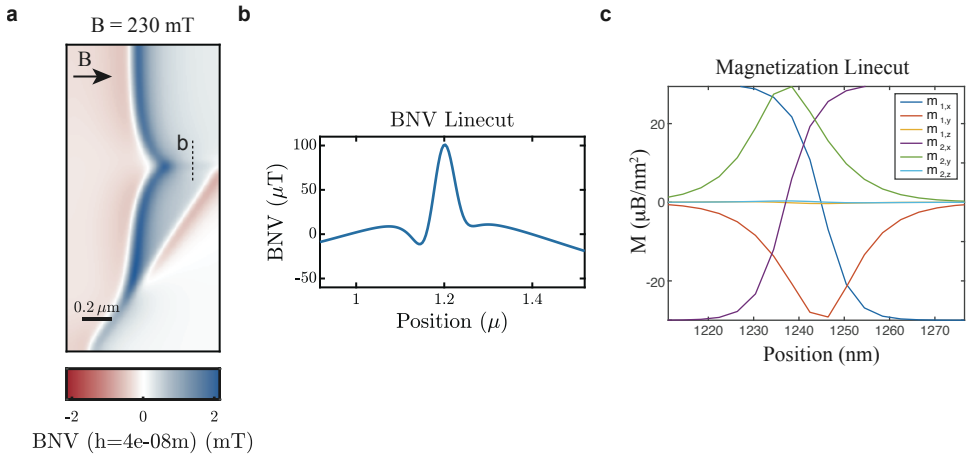

Figure A.5.: Micromagnetic simulation of an AFM domain wall in bilayer CrSBr in an external field of $B_{\text{ext}} = 230$ mT along the b-axis. **a** Reconstructed magnetic stray field along the NV-axis ($\phi = 340°$, $\theta = 53°$) generated from the magnetization calculated in mumax, see Fig. 5.2b. **b** Linecut though the magnetic stray field of the AFM domain wall (extracted at an NV-to-sample-distance of 40 nm), as indicated by the dashed line in **a**. To minimize the background, only the stray field for the bilayer flake is plotted here, neglecting any contribution from the third layer in the simulation, which corresponds to the trilayer. **c** Linecuts of the simulated magnetization components of the individual CrSBr layers within the bilayer showing an offset of the DW core within the two layers.

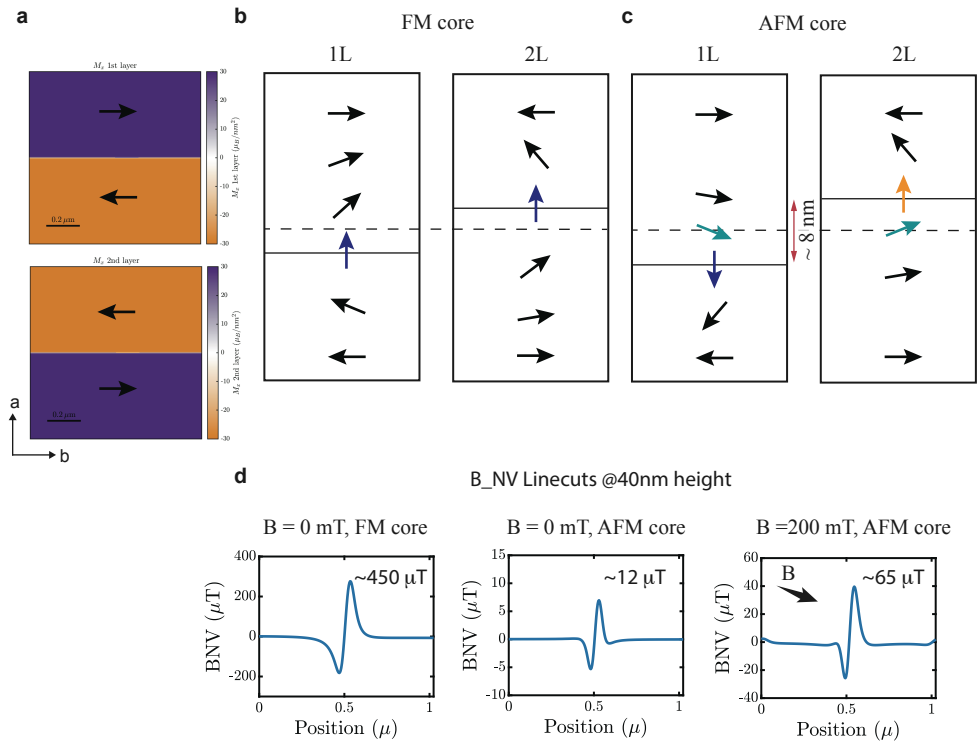

Figure A.6.: Toy model simulation of a horizontal domain wall in bilayer CrSBr. **a** Simulating an area of $\sim$ 1x1 μm^2 bilayer CrSBr with two differently coupled AFM regions separated by a domain wall (white line in the middle). The spin orientation of the individual regions are indicated by black arrows. **b** Implementing the simulation with a FM domain wall core, where the spins of both layers point along the y-axis ath the domain wall core (a-axis for CrSBr). **c** Same as **b** but with an AFM core, where the spins in the different layers point into opposite directions within the domain core. A lateral displacement of the domain wall core is observed within the two layers, which leads to a measurable magnetic stray field of such an AFM domain wall (as indicated by the two teal arrows, which sum up to a net magnetization contribution). **d** Linecuts of the domain walls for the three different configurations: FM (AFM) domain wall core at zero external bias field, creating a stray field of $\sim 450\mu$T ($\sim 12\mu$T) and an AFM core in an external bias field of $B_{\text{ext}} = 200$ mT generating a stay field of $\sim 65\mu$T. All stay field profiles are plotted for an NV-to-sample distance of 40 nm.

we only plot the stray field of the bilayer (layer 1 and 2 in the simulation) for the domain line cut. In order to visualize the lateral displacement of the domain wall core within the CrSBr sheets, we show the simulated magnetization component profiles as a linecut through the domain wall in Fig.A.5c. Our simulations suggest a lateral offset of $\sim$ 8 nm between the spin alignment within the domain.

We simulate the stray fields arising for different domain wall core spin configurations, i.e. spins coupling FM or AFM within the domain wall core of two adjacent

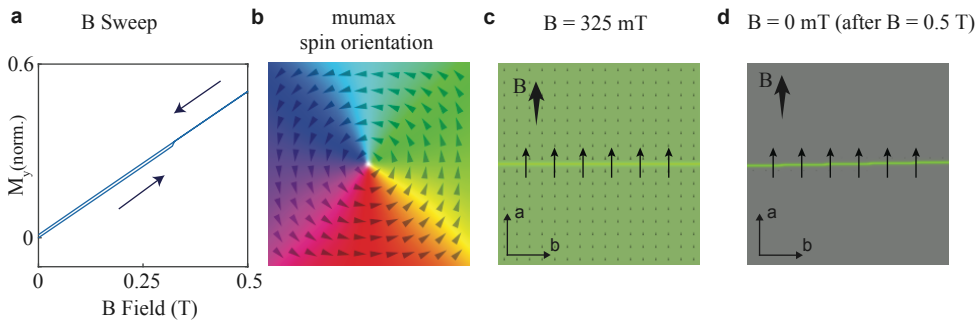

Figure A.7.: Toy model simulation of the spin reorientation in the domain wall core from AFM to FM. **a** Magnetization component of the flake along the *a*-axis (y-axis in the simulation) plotted as a function of an external magnetic field applied along an NV center parallel to the *a*-axis ($\phi = 90°$, $\theta = 53°$). The spins within the flake will progressively tilt and at $\sim B_{\text{ext}} = 325$ mT (indicated by jump in M_y), the spins within a horizontal domain wall with an AFM core will flip into a FM arrangement, i.e. to a FM core. Retracting the external field to zero will leave the spins in a FM configuration aligned with the *a*-axis of CrSBr. **b** Color code used in the micromagnetic simulation software mumax for the spin orientation [165]. **c** Snapshot of the spin orientation of bilayer CrSBr with an AFM domain at $\sim B_{\text{ext}} = 325$ mT, where the spins in the domain core have flipped from an AFM to a FM configuration pointing along the *a*-axis of the material (indicated by black arrows) and green color code. **d** Same as **c** but after sweeping the external field back down to zero.

monolayers CrSBr sheets, shown in Fig.A.6. Comparing these results with the measured stray field strength of the domain wall (Fig. 5.2c) allows for qualitatively assigning a most likely spin structure to the observed domain wall. Since this "toy model" simulation is reduced to a simplified version of a $\sim$ 1x1 μm^2 bilayer CrSBr flake with a manually induced domain wall and no neighboring flakes, we expect a mismatch between the obtained stray field values from the simulation versus the measured values and only qualitative comparisons can be drawn.

In the simulations, we implement two different AFM regions in bilayer CrSBr with opposite spin alignment per CrSBr layer, as shown in Fig. A.6a. The regions are separated by a manually induced domain wall, which we choose to have spins aligning along the *a*-axis (y-axis of the plots) in either a FM or AFM configuration. Afterwards, the simulation finds the energy minima of each configuration, where in all configurations the domain wall core settles to approximately a width of $\sim 15-20$ nm. Fig. A.6b,c show the spin configuration of the domain wall in each CrSBr layer after minimizing the system's energy: FM core (b) versus AFM core (c). In the presence of an external field $B_{\text{ext}} = 200$ mT along the NV-axis ($\phi = 340°$, $\theta = 53°$), the spins within the AFM core domain wall will rotate towards the external field. The lateral displacement of the two domain walls within the layers leads to a measurable stray field. The corresponding magnetic stray field profiles of the domain walls (along the NV axis, at 40 nm above the sample) are shown in Fig. A.6d. We conclude that the stray field of a tilted AFM core ($\sim 65\,\mu$T) qualitatively fits best to our observed

domain wall with a stray field of $\sim 140\,\mu$T. The discrepancy between the toy model simulation of a tilted AFM domain core ($\sim 65\,\mu$T) and the value extracted from the simulation of the full flake geometry ($\sim 110\,\mu$T) could stem from the simplification of the bilayer flake in the toymodel (smaller flake size, artificially introduced domain wall, no neighboring layers) and the difference of external field direction and magnitude employed in the two different simulation series (toy model: 200 mT applied along $\phi = 340°$, $\theta = 53°$, full flake simulation: 230 mT applied along $\phi = 0°$, $\theta = 90°$).

We use our toy model simulation to assess if the AFM domain wall core can be switched into a FM configuration by applying an external field along the a-axis (y-axis in simulation) of the material. Fig. A.7 summarizes our finding that applying a field of ~ 300 mT along the a-axis is enough to change the spins within the domain wall core into a FM configuration.

These simulations start off with a horizontal induced AFM domain with an AFM core in the presence of an external magnetic field pointing along the b-axis. Afterwards, the direction of the external field is changed to point along an NV pointing along the a-axis of CrSBr and slightly out of plane (due to the diamond lattice structure, i.e. $\phi = 90°$, $\theta = 53°$) and is swept from 0 mT to 0.5 T and back to zero. Fig. A.7a shows that the spins within the domain core change their configuration to align FM at $B = 325$ mT. A snapshot of the spin alignment at this field is shown in Fig. A.7c. The green color code denotes spins orienting along the a-axis of CrSBr (c.f. color code of mumax plotted in Fig. A.7b) and is additionally highlighted with black arrows. After reducing the field back to 0 mT, the FM alignment within the domain wall core remains stable, see Fig. A.7d.

A.4.2. Cusp in Bilayer CrSBr sample $S3_{\mathrm{Air}}$

We have previously observed a FM cusp in sample $S3_{\mathrm{Air}}$, when measuring the magnetization during the AFM-to-FM spin-flip transition, shown in Fig. A.8. The observation of the cusp would indicate the presence of an AFM domain wall, however, we were unable to resolve any potential feature above noise emerging form the cusp in our measurement series, see Fig. A.8b.

Plotting the same data on a more restricted magnetic field range of 300 μT (signal of AFM domain wall is expected to be $60 - 150\ \mu$T), Fig A.8c, shows a slight increase in magnetic noise along the cusp tip, which could result from an AFM domain wall. It could be plausible that an increased NV-to-sample distance in this specific measurement series made it impossible to detect a stray field from a potential domain. However, these are only speculations and it is not possible to conclude from this data set whether domain wall was present in this flake or not.

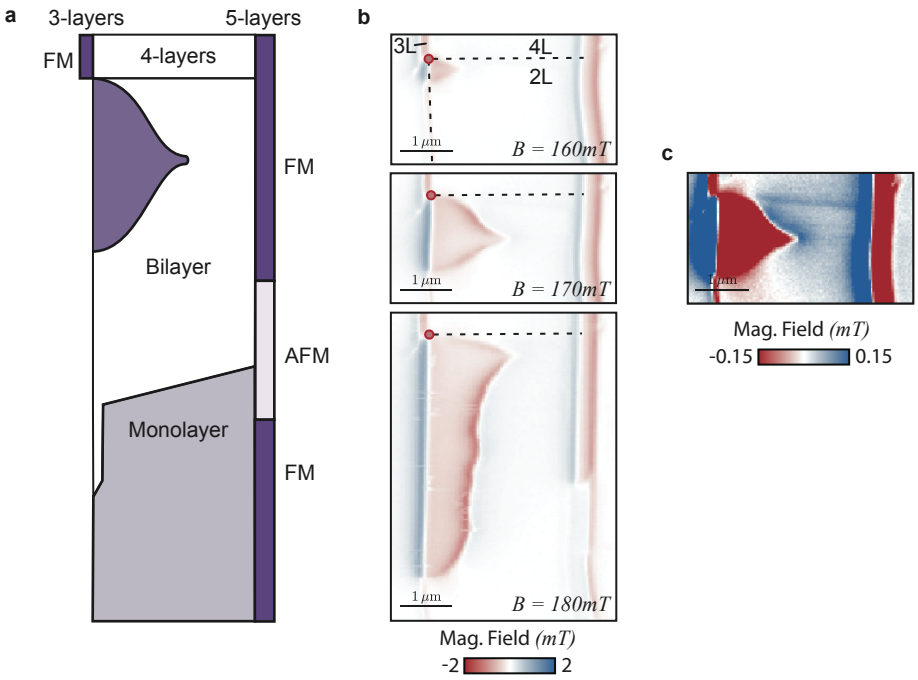

Figure A.8.: Observation of a FM cusp in bilayer CrSBr sample $S3_{\mathrm{Air}}$. **a** Schematic of sample $S3_{\mathrm{Air}}$ illustrating the formation of an FM region in bilayer CrSBr region. **b** Magnetic image at 160mT, showing the nucleation of a FM region at the interface of 2,3 and 4 layers. Magnetic image at 170mT (180mT) showing the emergence (expansion) of a FM cusp shaped region within the bilayer flake. **c** Magnetic field data recorded at 170mT plotted on a smaller field range to highlight magnetic signals below 300 mT. There is a faint increase in magnetic noise once at the bi-/four-layer interface and once as a horizontal line emerging from the cusp end. It is, however, not possible to conclude weather this signal corresponds to a domain wall or not.

A.5. The zoo of 2D materials

When talking about vdW materials, scientists sometimes refer to them as *the zoo of 2D materials*, due to their large variety of different material properties. When working with such vdW crystals, it gets quickly apparent that another interpretation of *the zoo of 2D materials* exists, as shown in Fig. A.9.

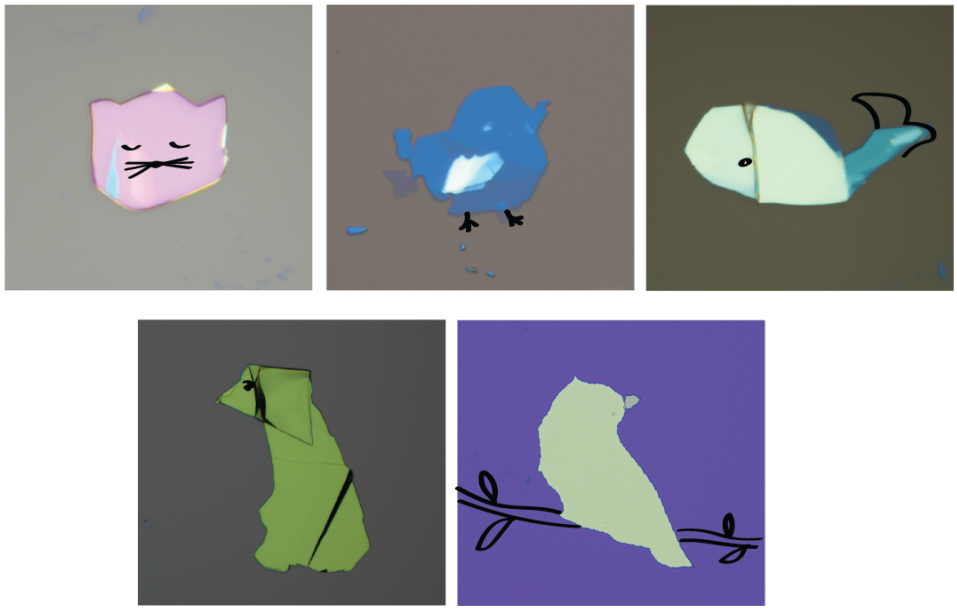

Figure A.9.: An artistic interpretation of *the zoo of 2D materials*. Depicted are graphite, hBN and CrX_3 flakes, all in the size of several μms. The black brush drawings help spark imagination.

B. Bibliography

[1] N. D. Mermin and H. Wagner, *Absence of ferromagnetism or antiferromagnetism in one- or two-dimensional isotropic Heisenberg models*, Phys. Rev. Lett. **17**, 1133 (1966).

[2] C. Gong and X. Zhang, *Two-dimensional magnetic crystals and emergent heterostructure devices*, Science **363**, 706 (2019).

[3] M. Gibertini, M. Koperski, A. F. Morpurgo, and K. S. Novoselov, *Magnetic 2D materials and heterostructures*, Nature Nanotechnology **14**, 408 (2019).

[4] K. S. Novoselov, A. K. Geim, S. V. Morozov, D. Jiang, Y. Zhang, S. V. Dubonos, I. V. Grigorieva, and A. A. Firsov, *Electric field effect in atomically thin carbon films*, Science **306**, 666 (2004).

[5] *Twenty years of 2D materials*, Nature Physics **20**, 1 (2024).

[6] B. Huang, G. Clark, E. Navarro-Moratalla, D. R. Klein, R. Cheng, K. L. Seyler, D. Zhong, E. Schmidgall, M. A. McGuire, D. H. Cobden, W. Yao, D. Xiao, P. Jarillo-Herrero, and X. Xu, *Layer-dependent ferromagnetism in a van der Waals crystal down to the monolayer limit*, Nature **546**, 270 (2017).

[7] C. Gong, L. Li, Z. Li, H. Ji, A. Stern, Y. Xia, T. Cao, W. Bao, C. Wang, Y. Wang, Z. Q. Qiu, R. J. Cava, S. G. Louie, J. Xia, and X. Zhang, *Discovery of intrinsic ferromagnetism in two-dimensional van der Waals crystals*, Nature **546**, 265 (2017).

[8] Q.-C. Sun, T. Song, E. Anderson, A. Brunner, J. Förster, T. Shalomayeva, T. Taniguchi, K. Watanabe, J. Gräfe, R. Stöhr, X. Xu, and J. Wrachtrup, *Magnetic domains and domain wall pinning in atomically thin $CrBr_3$ revealed by nanoscale imaging*, Nature Communications **12** (2021).

[9] M. A. Tschudin, D. A. Broadway, P. Siegwolf, C. Schrader, E. J. Telford, B. Gross, J. Cox, A. E. E. Dubois, D. G. Chica, R. Rama-Eiroa, E. J. G. Santos, M. Poggio, M. E. Ziebel, C. R. Dean, X. Roy, and P. Maletinsky, *Imaging nanomagnetism and magnetic phase transitions in atomically thin crsbr*, Nature Communications **15**, 6005 (2024).

[10] K. Hejazi, Z.-X. Luo, and L. Balents, *Noncollinear phases in moiré magnets*, Proceedings of the National Academy of Sciences **117**, 10721–10726 (2020).

[11] T. Song, Q.-C. Sun, E. Anderson, C. Wang, J. Qian, T. Taniguchi, K. Watanabe, M. A. McGuire, R. Stöhr, D. Xiao, T. Cao, J. Wrachtrup, and X. Xu, *Direct visualization of magnetic domains and moiré magnetism in twisted 2D magnets*, Science **374**, 1140 (2021).

[12] M. Huang, Z. Sun, G. Yan, H. Xie, N. Agarwal, G. Ye, S. H. Sung, H. Lu, J. Zhou, S. Yan, S. Tian, H. Lei, R. Hovden, R. He, H. Wang, L. Zhao, and C. R. Du, *Revealing intrinsic domains and fluctuations of moiré magnetism by a wide-field quantum microscope*, Nature Communications **14** (2023).

[13] Y. Wu, S. Zhang, J. Zhang, W. Wang, Y. L. Zhu, J. Hu, G. Yin, K. Wong, C. Fang, C. Wan, X. Han, Q. Shao, T. Taniguchi, K. Watanabe, J. Zang, Z. Mao, X. Zhang, and K. L. Wang, *Néel-type skyrmion in WTe_2/Fe_3GeTe_2 van der Waals heterostructure*, Nature Communications **11** (2020).

[14] L. Thiel, Z. Wang, M. A. Tschudin, D. Rohner, I. Gutiérrez-Lezama, N. Ubrig, M. Gibertini, E. Giannini, A. F. Morpurgo, and P. Maletinsky, *Probing magnetism in 2D materials at the nanoscale with single-spin microscopy*, Science **364**, 973 (2019).

[15] L. Rondin, J.-P. Tetienne, T. Hingant, J.-F. Roch, P. Maletinsky, and V. Jacques, *Magnetometry with nitrogen-vacancy defects in diamond*, Reports on Progress in Physics **77**, 056503 (2014).

[16] V. M. Acosta, L. S. Bouchard, D. Budker, R. Folman, T. Lenz, P. Maletinsky, D. Rohner, Y. Schlussel, and L. Thiel, *Color centers in diamond as novel probes of superconductivity*, Journal of Superconductivity and Novel Magnetism **32**, 85–95 (2018).

[17] L. Thiel, *Nanoscale magnetometry with a single spin in diamond at cryogenic temperatures*, Ph.D. thesis, University of Basel (2019).

[18] N. Sivadas, S. Okamoto, X. Xu, C. J. Fennie, and D. Xiao, *Stacking-dependent magnetism in bilayer CrI_3*, Nano Letters **18**, 7658–7664 (2018).

[19] Q. Tong, F. Liu, J. Xiao, and W. Yao, *Skyrmions in the moiré of van der Waals 2D magnets*, Nano Letters **18**, 7194–7199 (2018).

[20] M. Akram, H. LaBollita, D. Dey, J. Kapeghian, O. Erten, and A. S. Botana, *Moiré skyrmions and chiral magnetic phases in twisted CrX_3 (X = I, Br, and Cl) bilayers*, Nano Letters **21**, 6633–6639 (2021).

[21] M. Bode, E. Y. Vedmedenko, K. von Bergmann, A. Kubetzka, P. Ferriani, S. Heinze, and R. Wiesendanger, *Atomic spin structure of antiferromagnetic domain walls*, Nature Materials **5**, 477 (2006).

[22] I. Gross, W. Akhtar, V. Garcia, L. J. Martínez, S. Chouaieb, K. Garcia, C. Carrétéro, A. Barthélémy, P. Appel, P. Maletinsky, J. V. Kim, J. Y. Chauleau, N. Jaouen, M. Viret, M. Bibes, S. Fusil, and V. Jacques, *Real-space imaging of non-collinear antiferromagnetic order with a single-spin magnetometer*, Nature **549**, 252 (2017).

[23] P. M. Sass, W. Ge, J. Yan, D. Obeysekera, J. J. Yang, and W. Wu, *Magnetic imaging of domain walls in the antiferromagnetic topological insulator $MnBi_2Te_4$*, Nano Letters **20**, 2609 (2020).

[24] Y. Lee, C. Kim, S. Son, J. Cui, G. Park, K.-X. Zhang, S. Oh, H. Cheong, A. Kleibert, and J.-G. Park, *Imaging thermally fluctuating Néel vectors in van der Waals antiferromagnet $NiPS_3$*, Nano Letters (2024).

[25] Y. Zhang, Y.-W. Tan, H. L. Stormer, and P. Kim, *Experimental observation of the quantum Hall effect and Berry's phase in graphene*, Nature **438**, 201–204 (2005).

[26] N. Mounet, M. Gibertini, P. Schwaller, D. Campi, A. Merkys, A. Marrazzo, T. Sohier, I. E. Castelli, A. Cepellotti, G. Pizzi, and N. Marzari, *Two-dimensional materials from high-throughput computational exfoliation of experimentally known compounds*, Nature Nanotechnology **13**, 246–252 (2018).

[27] K. S. Novoselov, A. Mishchenko, A. Carvalho, and A. H. C. Neto, *2D materials and van der Waals heterostructures*, Science **353**, aac9439 (2016).

[28] K. F. Mak, C. Lee, J. Hone, J. Shan, and T. F. Heinz, *Atomically thin MoS_2: A new direct-gap semiconductor*, Phys. Rev. Lett. **105**, 136805 (2010).

[29] D. A. Broadway, S. C. Scholten, C. Tan, N. Dontschuk, S. E. Lillie, B. C. Johnson, G. Zheng, Z. Wang, A. R. Oganov, S. Tian, C. Li, H. Lei, L. Wang, L. C. L. Hollenberg, and J.-P. Tetienne, *Imaging domain reversal in an ultrathin van der Waals ferromagnet*, Advanced Materials **32**, 2003314 (2020).

[30] T. S. Ghiasi, M. Borst, S. Kurdi, B. G. Simon, I. Bertelli, C. Boix-Constant, S. Mañas-Valero, H. S. J. van der Zant, and T. van der Sar, *Nitrogen-vacancy magnetometry of CrSBr by diamond membrane transfer*, npj 2D Materials and Applications **7**, 62 (2023).

[31] Y. Cao, V. Fatemi, S. Fang, K. Watanabe, T. Taniguchi, E. Kaxiras, and P. Jarillo-Herrero, *Unconventional superconductivity in magic-angle graphene superlattices*, Nature **556**, 43 (2018).

[32] Y. Cao, V. Fatemi, A. Demir, S. Fang, S. L. Tomarken, J. Y. Luo, J. D. Sanchez-Yamagishi, K. Watanabe, T. Taniguchi, E. Kaxiras, R. C. Ashoori, and P. Jarillo-Herrero, *Correlated insulator behaviour at half-filling in magic-angle graphene superlattices*, Nature **556**, 80–84 (2018).

[33] A. L. Sharpe, E. J. Fox, A. W. Barnard, J. Finney, K. Watanabe, T. Taniguchi, M. A. Kastner, and D. Goldhaber-Gordon, *Emergent ferromagnetism near three-quarters filling in twisted bilayer graphene*, Science **365**, 605 (2019).

[34] H. Polshyn, J. Zhu, M. A. Kumar, Y. Zhang, F. Yang, C. L. Tschirhart, M. Serlin, K. Watanabe, T. Taniguchi, A. H. MacDonald, and A. F. Young, *Electrical switching of magnetic order in an orbital Chern insulator*, Nature **588**, 66–70 (2020).

[35] D. Zhong, K. L. Seyler, X. Linpeng, R. Cheng, N. Sivadas, B. Huang, E. Schmidgall, T. Taniguchi, K. Watanabe, M. A. McGuire, W. Yao, D. Xiao, K.-M. C. Fu, and X. Xu, *Van der Waals engineering of ferromagnetic semiconductor heterostructures for spin and valleytronics*, Science Advances **3** (2017).

[36] L. Ciorciaro, M. Kroner, K. Watanabe, T. Taniguchi, and A. Imamoglu, *Observation of magnetic proximity effect using resonant optical spectroscopy of an electrically tunable $MoSe_2/CrBr_3$ heterostructure*, Physical Review Letters **124** (2020).

[37] S. Jiang, L. Li, Z. Wang, K. F. Mak, and J. Shan, *Controlling magnetism in 2D CrI_3 by electrostatic doping*, Nature Nanotechnology **13**, 549 (2018).

[38] J. Cenker, S. Sivakumar, K. Xie, A. Miller, P. Thijssen, Z. Liu, A. Dismukes, J. Fonseca, E. Anderson, X. Zhu, X. Roy, D. Xiao, J.-H. Chu, T. Cao, and X. Xu, *Reversible strain-induced magnetic phase transition in a van der Waals magnet*, Nature Nanotechnology **17**, 256 (2022).

[39] Y. Ahn, X. Guo, S. Son, Z. Sun, and L. Zhao, *Progress and prospects in two-dimensional magnetism of van der Waals materials*, arXiv:2401.13781 (2024).

[40] J.-U. Lee, S. Lee, J. H. Ryoo, S. Kang, T. Y. Kim, P. Kim, C.-H. Park, J.-G. Park, and H. Cheong, *Ising-type magnetic ordering in atomically thin $FePS_3$*, Nano Letters **16**, 7433–7438 (2016).

[41] M. McGuire, *Crystal and magnetic structures in layered, transition metal dihalides and trihalides*, Crystals **7**, 121 (2017).

[42] K. S. Burch, D. Mandrus, and J.-G. Park, *Magnetism in two-dimensional van der Waals materials*, Nature **563**, 47–52 (2018).

[43] A. Bedoya-Pinto, J.-R. Ji, A. K. Pandeya, P. Gargiani, M. Valvidares, P. Sessi, J. M. Taylor, F. Radu, K. Chang, and S. S. P. Parkin, *Intrinsic 2D-XY ferromagnetism in a van der Waals monolayer*, Science **374**, 616 (2021).

[44] J.-P. Tetienne, T. Hingant, L. Martínez, S. Rohart, A. Thiaville, L. H. Diez, K. Garcia, J.-P. Adam, J.-V. Kim, J.-F. Roch, I. Miron, G. Gaudin, L. Vila, B. Ocker, D. Ravelosona, and V. Jacques, *The nature of domain walls in ultrathin ferromagnets revealed by scanning nanomagnetometry*, Nature Communications **6** (2015).

[45] T. Li, S. Jiang, N. Sivadas, Z. Wang, Y. Xu, D. Weber, J. E. Goldberger, K. Watanabe, T. Taniguchi, C. J. Fennie, K. Fai Mak, and J. Shan, *Pressure-controlled interlayer magnetism in atomically thin CrI_3*, Nature Materials **18**, 1303–1308 (2019).

[46] T. Song, Z. Fei, M. Yankowitz, Z. Lin, Q. Jiang, K. Hwangbo, Q. Zhang, B. Sun, T. Taniguchi, K. Watanabe, M. A. McGuire, D. Graf, T. Cao, J.-H. Chu, D. H. Cobden, C. R. Dean, D. Xiao, and X. Xu, *Switching 2D magnetic states via pressure tuning of layer stacking*, Nature Materials **18**, 1298–1302 (2019).

[47] Y.-H. Li and R. Cheng, *Moiré magnons in twisted bilayer magnets with collinear order*, Physical Review B **102** (2020).

[48] Y. Xu, A. Ray, Y.-T. Shao, S. Jiang, K. Lee, D. Weber, J. E. Goldberger, K. Watanabe, T. Taniguchi, D. A. Muller, K. F. Mak, and J. Shan, *Coexisting*

ferromagnetic–antiferromagnetic state in twisted bilayer CrI_3, Nature Nanotechnology **17**, 143–147 (2021).

[49] H. Xie, X. Luo, Z. Ye, Z. Sun, G. Ye, S. H. Sung, H. Ge, S. Yan, Y. Fu, S. Tian, H. Lei, K. Sun, R. Hovden, R. He, and L. Zhao, *Evidence of non-collinear spin texture in magnetic moiré superlattices*, Nature Physics **19**, 1150–1155 (2023).

[50] Q. Song, C. A. Occhialini, E. Ergeçen, B. Ilyas, D. Amoroso, P. Barone, J. Kapeghian, K. Watanabe, T. Taniguchi, A. S. Botana, S. Picozzi, N. Gedik, and R. Comin, *Evidence for a single-layer van der Waals multiferroic*, Nature **602**, 601–605 (2022).

[51] D. R. Klein, D. MacNeill, J. L. Lado, D. Soriano, E. Navarro-Moratalla, K. Watanabe, T. Taniguchi, S. Manni, P. Canfield, J. Fernández-Rossier, and P. Jarillo-Herrero, *Probing magnetism in 2D van der Waals crystalline insulators via electron tunneling*, Science **360**, 1218 (2018).

[52] D. R. Klein, D. MacNeill, Q. Song, D. T. Larson, S. Fang, M. Xu, R. A. Ribeiro, P. C. Canfield, E. Kaxiras, R. Comin, and P. Jarillo-Herrero, *Enhancement of interlayer exchange in an ultrathin two-dimensional magnet*, Nature Physics **15**, 1255–1260 (2019).

[53] E. J. Telford, A. H. Dismukes, K. Lee, M. Cheng, A. Wieteska, A. K. Bartholomew, Y.-S. Chen, X. Xu, A. N. Pasupathy, X. Zhu, C. R. Dean, X. Roy, E. J. Telford, M. Cheng, A. Wieteska, A. N. Pasupathy, C. R. Dean, A. H. Dismukes, K. Lee, A. M. Bartholomew, X. y Zhu, X. Roy, Y. s Chen, and X. Xu, *Layered antiferromagnetism induces large negative magnetoresistance in the van der Waals semiconductor CrSBr*, Advanced Materials **32**, 2003240 (2020).

[54] Z. Fei, B. Huang, P. Malinowski, W. Wang, T. Song, J. Sanchez, W. Yao, D. Xiao, X. Zhu, A. F. May, W. Wu, D. H. Cobden, J.-H. Chu, and X. Xu, *Two-dimensional itinerant ferromagnetism in atomically thin Fe_3GeTe_2*, Nature Materials **17**, 778–782 (2018).

[55] J.-X. Qiu, C. Tzschaschel, J. Ahn, A. Gao, H. Li, X.-Y. Zhang, B. Ghosh, C. Hu, Y.-X. Wang, Y.-F. Liu, D. Bérubé, T. Dinh, Z. Gong, S.-W. Lien, S.-C. Ho, B. Singh, K. Watanabe, T. Taniguchi, D. C. Bell, H.-Z. Lu, A. Bansil, H. Lin, T.-R. Chang, B. B. Zhou, Q. Ma, A. Vishwanath, N. Ni, and S.-Y. Xu, *Axion optical induction of antiferromagnetic order*, Nature Materials **22**, 583–590 (2023).

[56] N. P. Wilson, K. Lee, J. Cenker, K. Xie, A. H. Dismukes, E. J. Telford, J. Fonseca, S. Sivakumar, C. Dean, T. Cao, X. Roy, X. Xu, and X. Zhu, *Interlayer electronic coupling on demand in a 2D magnetic semiconductor*, Nature Materials **20**, 1657 (2021).

[57] F. Tabataba-Vakili, H. P. G. Nguyen, A. Rupp, K. Mosina, A. Papavasileiou, K. Watanabe, T. Taniguchi, P. Maletinsky, M. M. Glazov, Z. Sofer, A. S. Baimuratov, and A. Högele, *Doping-control of excitons and magnetism in few-layer crsbr*, Nature Communications **15**, 4735 (2024).

[58] N. J. McLaughlin, C. Hu, M. Huang, S. Zhang, H. Lu, G. Q. Yan, H. Wang, Y. Tserkovnyak, N. Ni, and C. R. Du, *Quantum imaging of magnetic phase transitions and spin fluctuations in intrinsic magnetic topological nanoflakes*, Nano Letters **22**, 5810–5817 (2022).

[59] W. Chen, Z. Sun, Z. Wang, L. Gu, X. Xu, S. Wu, and C. Gao, *Direct observation of van der Waals stacking–dependent interlayer magnetism*, Science **366**, 983–987 (2019).

[60] B. Niu, T. Su, B. A. Francisco, S. Ghosh, F. Kargar, X. Huang, M. Lohmann, J. Li, Y. Xu, T. Taniguchi, K. Watanabe, D. Wu, A. Balandin, J. Shi, and Y.-T. Cui, *Coexistence of magnetic orders in two-dimensional magnet CrI_3*, Nano Letters **20**, 553–558 (2019).

[61] W. Ci, H. Yang, W. Xue, R. Yang, B. Lv, P. Wang, R.-W. Li, and X.-H. Xu, *Thickness-dependent and strain-tunable magnetism in two-dimensional van der Waals VSe_2*, Nano Research **15**, 7597–7603 (2022).

[62] D. J. Rizzo, A. S. McLeod, C. Carnahan, E. J. Telford, A. H. Dismukes, R. A. Wiscons, Y. Dong, C. Nuckolls, C. R. Dean, A. N. Pasupathy, X. Roy, D. Xiao, and D. N. Basov, *Visualizing atomically layered magnetism in CrSBr*, Advanced Materials **2022**, 2201000 (2022).

[63] E. Marchiori, L. Ceccarelli, N. Rossi, L. Lorenzelli, C. L. Degen, and M. Poggio, *Nanoscale magnetic field imaging for 2D materials*, Nature Reviews Physics **4**, 49–60 (2021).

[64] C. L. Tschirhart, M. Serlin, H. Polshyn, A. Shragai, Z. Xia, J. Zhu, Y. Zhang, K. Watanabe, T. Taniguchi, M. E. Huber, and A. F. Young, *Imaging orbital ferromagnetism in a moiré Chern insulator*, Science **372**, 1323 (2021).

[65] A. Vervelaki, K. Bagani, D. Jetter, M.-H. Doan, T. K. Chau, B. Gross, D. V. Christensen, P. Bøggild, and M. Poggio, *Visualizing thickness-dependent magnetic textures in few-layer $Cr_2Ge_2Te_6$*, Communications Materials **5** (2024).

[66] A. Finkler, Y. Segev, Y. Myasoedov, M. L. Rappaport, L. Ne'eman, D. Vasyukov, E. Zeldov, M. E. Huber, J. Martin, and A. Yacoby, *Self-aligned nanoscale SQUID on a tip*, Nano Letters **10**, 1046–1049 (2010).

[67] M. Wyss, K. Bagani, D. Jetter, E. Marchiori, A. Vervelaki, B. Gross, J. Ridderbos, S. Gliga, C. Schönenberger, and M. Poggio, *Magnetic, thermal, and topographic imaging with a nanometer-scale SQUID-on-lever scanning probe*, Physical Review Applied **17** (2022).

[68] J. M. Taylor, P. Cappellaro, L. Childress, L. Jiang, D. Budker, P. R. Hemmer, A. Yacoby, R. Walsworth, and M. D. Lukin, *High-sensitivity diamond magnetometer with nanoscale resolution*, Nature Physics **4**, 810 (2008).

[69] J. R. Maze, P. L. Stanwix, J. S. Hodges, S. Hong, J. M. Taylor, P. Cappellaro, L. Jiang, M. V. G. Dutt, E. Togan, A. S. Zibrov, A. Yacoby, R. L. Walsworth, and M. D. Lukin, *Nanoscale magnetic sensing with an individual electronic spin in diamond*, Nature **455**, 644 (2008).

[70] P. Maletinsky, S. Hong, M. S. Grinolds, B. Hausmann, M. D. Lukin, R. L. Walsworth, M. Loncar, and A. Yacoby, *A robust scanning diamond sensor for nanoscale imaging with single nitrogen-vacancy centres*, Nature Nanotechnology **7**, 320 (2012).

[71] F. Casola, T. van der Sar, and A. Yacoby, *Probing condensed matter physics with magnetometry based on nitrogen-vacancy centres in diamond*, Nature Reviews Materials **3**, 17088 (2018).

[72] N. B. Manson, J. P. Harrison, and M. J. Sellars, *Nitrogen-vacancy center in diamond: Model of the electronic structure and associated dynamics*, Phys. Rev. B **74**, 104303 (2006).

[73] R. Schirhagl, K. Chang, M. Loretz, and C. L. Degen, *Nitrogen-Vacancy centers in diamond: Nanoscale sensors for physics and biology*, Annu. Rev. Phys. Chem. **65**, 83 (2014).

[74] D. Riedel, I. Söllner, B. J. Shields, S. Starosielec, P. Appel, E. Neu, P. Maletinsky, and R. J. Warburton, *Deterministic enhancement of coherent photon generation from a nitrogen-vacancy center in ultrapure diamond*, Phys. Rev. X **7**, 031040 (2017).

[75] M. W. Doherty, N. B. Manson, P. Delaney, F. Jelezko, J. Wrachtrup, and L. C. Hollenberg, *The nitrogen-vacancy colour centre in diamond*, Physics Reports **528**, 1 (2013).

[76] A. Dréau, M. Lesik, L. Rondin, P. Spinicelli, O. Arcizet, J.-F. Roch, and V. Jacques, *Avoiding power broadening in optically detected magnetic resonance of single NV defects for enhanced dc magnetic field sensitivity*, Physical Review B **84** (2011).

[77] J. F. Barry, J. M. Schloss, E. Bauch, M. J. Turner, C. A. Hart, L. M. Pham, and R. L. Walsworth, *Sensitivity optimization for NV-diamond magnetometry*, Reviews of Modern Physics **92** (2020).

[78] L. Rondin, J.-P. Tetienne, T. Hingant, J.-F. Roch, P. Maletinsky, and V. Jacques, *Magnetometry with nitrogen-vacancy defects in diamond*, Reports on Progress in Physics **77**, 56503 (2014).

[79] F. Casola, T. van der Sar, and A. Yacoby, *Probing condensed matter physics with magnetometry based on nitrogen-vacancy centres in diamond*, Nature Reviews Materials **3** (2018).

[80] P. Siegwolf, *Exploring two-dimensional magnetism by scanning nitrogen-vacancy magnetometry*, Ph.D. thesis, University of Basel (2024).

[81] M. A. McGuire, H. Dixit, V. R. Cooper, and B. C. Sales, *Coupling of crystal structure and magnetism in the layered, ferromagnetic insulator CrI_3*, Chemistry of Materials **27**, 612 (2015).

[82] F. Yao, V. Multian, Z. Wang, N. Ubrig, J. Teyssier, F. Wu, E. Giannini, M. Gibertini, I. Gutiérrez-Lezama, and A. F. Morpurgo, *Multiple antiferromagnetic phases and magnetic anisotropy in exfoliated $CrBr_3$ multilayers*, Nature Communications **14** (2023).

[83] S. J. Haigh, A. Gholinia, R. Jalil, S. Romani, L. Britnell, D. C. Elias, K. S. Novoselov, L. A. Ponomarenko, A. K. Geim, and R. Gorbachev, *Cross-sectional imaging of individual layers and buried interfaces of graphene-based heterostructures and superlattices*, Nature Materials **11**, 764 (2012).

[84] Z. Wang, I. Gutiérrez-Lezama, N. Ubrig, M. Kroner, M. Gibertini, T. Taniguchi, K. Watanabe, A. Imamoğlu, E. Giannini, and A. F. Morpurgo, *Very large tunneling magnetoresistance in layered magnetic semiconductor CrI_3*, Nature Communications **9**, 2516 (2018).

[85] C. Zhang, J. Song, and Q. Yang, *Periodic buckling patterns of graphene/hexagonal boron nitride heterostructure*, Nanotechnology **25**, 445401 (2014).

[86] A. K. Geim and I. V. Grigorieva, *Van der Waals heterostructures*, Nature **499**, 419 (2013).

[87] K. S. Novoselov, D. Jiang, F. Schedin, T. J. Booth, V. V. Khotkevich, S. V. Morozov, and A. K. Geim, *Two-dimensional atomic crystals*, Proceedings of the National Academy of Sciences **102**, 10451 (2005).

[88] P. Blake, E. W. Hill, A. H. Castro Neto, K. S. Novoselov, D. Jiang, R. Yang, T. J. Booth, and A. K. Geim, *Making graphene visible*, Applied Physics Letters **91**, 063124 (2007).

[89] R. V. Gorbachev, I. Riaz, R. R. Nair, R. Jalil, L. Britnell, B. D. Belle, E. W. Hill, K. S. Novoselov, K. Watanabe, T. Taniguchi, A. K. Geim, and P. Blake, *Hunting for monolayer boron nitride: Optical and Raman signatures*, Small **7**, 465 (2011).

[90] L. Wang, I. Meric, P. Y. Huang, Q. Gao, Y. Gao, H. Tran, T. Taniguchi, K. Watanabe, L. M. Campos, D. A. Muller, J. Guo, P. Kim, J. Hone, K. L. Shepard, and C. R. Dean, *One-dimensional electrical contact to a two-dimensional material*, Science **342**, 614 (2013).

[91] P. J. Zomer, M. H. D. Guimarães, J. C. Brant, N. Tombros, and B. J. van Wees, *Fast pick up technique for high quality heterostructures of bilayer graphene and hexagonal boron nitride*, Applied Physics Letters **105**, 013101 (2014).

[92] D. Shcherbakov, P. Stepanov, D. Weber, Y. Wang, J. Hu, Y. Zhu, K. Watanabe, T. Taniguchi, Z. Mao, W. Windl, J. Goldberger, M. Bockrath, and C. N. Lau, *Raman spectroscopy, photocatalytic degradation, and stabilization of atomically thin chromium tri-iodide*, Nano Letters **18**, 4214 (2018).

[93] T. Zhang, M. Grzeszczyk, J. Li, W. Yu, H. Xu, P. He, L. Yang, Z. Qiu, H. Lin, H. Yang, J. Zeng, T. Sun, Z. Li, J. Wu, M. Lin, K. P. Loh, C. Su, K. S. Novoselov, A. Carvalho, M. Koperski, and J. Lu, *Degradation chemistry and*

kinetic stabilization of magnetic CrI_3, Journal of the American Chemical Society **144**, 5295 (2022).

[94] Y. Kim, P. Herlinger, T. Taniguchi, K. Watanabe, and J. H. Smet, *Reliable postprocessing improvement of van der Waals heterostructures*, ACS Nano **13**, 14182 (2019).

[95] L. J. McGilly, A. Kerelsky, N. R. Finney, K. Shapovalov, E.-M. Shih, A. Ghiotto, Y. Zeng, S. L. Moore, W. Wu, Y. Bai, K. Watanabe, T. Taniguchi, M. Stengel, L. Zhou, J. Hone, X. Zhu, D. N. Basov, C. Dean, C. E. Dreyer, and A. N. Pasupathy, *Visualization of moiré superlattices*, Nature Nanotechnology **15**, 580 (2020).

[96] P. Appel, E. Neu, M. Ganzhorn, A. Barfuss, M. Batzer, M. Gratz, A. Tschöpe, and P. Maletinsky, *Fabrication of all diamond scanning probes for nanoscale magnetometry*, Review of Scientific Instruments **87**, 063703 (2016).

[97] N. Hedrich, D. Rohner, M. Batzer, P. Maletinsky, and B. J. Shields, *Parabolic diamond scanning probes for single-spin magnetic field imaging*, Phys. Rev. Appl. **14**, 064007 (2020).

[98] D. F. Wise, *Could NV centres in diamond be used to measure donor spins in silicon?*, Ph.D. thesis, University College London (2021).

[99] J.-P. Tetienne, L. Rondin, P. Spinicelli, M. Chipaux, T. Debuisschert, J.-F. Roch, and V. Jacques, *Magnetic-field-dependent photodynamics of single NV defects in diamond: an application to qualitative all-optical magnetic imaging*, New Journal of Physics **14**, 103033 (2012).

[100] D. Rohner, J. Happacher, P. Reiser, M. A. Tschudin, A. Tallaire, J. Achard, B. J. Shields, and P. Maletinsky, *(111)-oriented, single crystal diamond tips for nanoscale scanning probe imaging of out-of-plane magnetic fields*, Applied Physics Letters **115**, 192401 (2019).

[101] P. Welter, J. Rhensius, A. Morales, M. S. Wörnle, C.-H. Lambert, G. Puebla-Hellmann, P. Gambardella, and C. L. Degen, *Scanning nitrogen-vacancy center magnetometry in large in-plane magnetic fields*, Applied Physics Letters **120**, 074003 (2022).

[102] J. Happacher, D. A. Broadway, J. Bocquel, P. Reiser, A. Jimenéz, M. A. Tschudin, L. Thiel, D. Rohner, M. l. G. Puigibert, B. Shields, J. R. Maze, V. Jacques, and P. Maletinsky, *Low-temperature photophysics of single nitrogen-vacancy centers in diamond*, Phys. Rev. Lett. **128**, 177401 (2022).

[103] J. Happacher, J. Bocquel, H. T. Dinani, M. A. , P. Reiser, D. A. Broadway, J. R. Maze, and P. Maletinsky, *Temperature-dependent photophysics of single NV centers in diamond*, Phys. Rev. Lett. **131**, 086904 (2023).

[104] A. P. Rooney, A. Kozikov, A. N. Rudenko, E. Prestat, M. J. Hamer, F. Withers, Y. Cao, K. S. Novoselov, M. I. Katsnelson, R. Gorbachev, and S. J. Haigh, *Observing imperfection in atomic interfaces for van der Waals heterostructures*, Nano Letters **17**, 5222 (2017).

[105] F. Pizzocchero, L. Gammelgaard, B. S. Jessen, J. Caridad, L. Wang, J. Hone, P. Bøggild, and T. J. Booth, *The hot pick-up technique for batch assembly of van der Waals heterostructures*, Nature Communications **7**, 11894 (2016).

[106] W. Wang, N. Clark, M. Hamer, A. Carl, E. Tovari, S. Sullivan-Allsop, E. Tillotson, Y. Gao, H. de Latour, F. Selles, J. Howarth, E. G. Castanon, M. Zhou, H. Bai, X. Li, A. Weston, K. Watanabe, T. Taniguchi, C. Mattevi, T. H. Bointon, P. V. Wiper, A. J. Strudwick, L. A. Ponomarenko, A. V. Kretinin, S. J. Haigh, A. Summerfield, and R. Gorbachev, *Clean assembly of van der Waals heterostructures using silicon nitride membranes*, Nature Electronics **6**, 981 (2023).

[107] S. Sangtawesin, B. L. Dwyer, S. Srinivasan, J. J. Allred, L. V. H. Rodgers, K. De Greve, A. Stacey, N. Dontschuk, K. M. O'Donnell, D. Hu, D. A. Evans, C. Jaye, D. A. Fischer, M. L. Markham, D. J. Twitchen, H. Park, M. D. Lukin, and N. P. de Leon, *Origins of diamond surface noise probed by correlating single-spin measurements with surface spectroscopy*, Phys. Rev. X **9**, 031052 (2019).

[108] S. Grover, M. Bocarsly, A. Uri, P. Stepanov, G. Di Battista, I. Roy, J. Xiao, A. Y. Meltzer, Y. Myasoedov, K. Pareek, K. Watanabe, T. Taniguchi, B. Yan, A. Stern, E. Berg, D. K. Efetov, and E. Zeldov, *Chern mosaic and Berry-curvature magnetism in magic-angle graphene*, Nature Physics **18**, 885 (2022).

[109] J. A. Zuber, M. Li, M. l. Grimau Puigibert, J. Happacher, P. Reiser, B. J. Shields, and P. Maletinsky, *Shallow silicon vacancy centers with lifetime-limited optical linewidths in diamond nanostructures*, Nano Letters **23**, 10901 (2023).

[110] D. MacNeill, G. M. Stiehl, M. H. D. Guimaraes, R. A. Buhrman, J. Park, and D. C. Ralph, *Control of spin–orbit torques through crystal symmetry in WTe_2/ferromagnet bilayers*, Nature Physics **13**, 300 (2017).

[111] Q. H. Wang, A. Bedoya-Pinto, M. Blei, A. H. Dismukes, A. Hamo, S. Jenkins, M. Koperski, Y. Liu, Q.-C. Sun, E. J. Telford, H. H. Kim, M. Augustin, U. Vool, J.-X. Yin, L. H. Li, A. Falin, C. R. Dean, F. Casanova, R. F. L. Evans, M. Chshiev, A. Mishchenko, C. Petrovic, R. He, L. Zhao, A. W. Tsen, B. D. Gerardot, M. Brotons-Gisbert, Z. Guguchia, X. Roy, S. Tongay, Z. Wang, M. Z. Hasan, J. Wrachtrup, A. Yacoby, A. Fert, S. Parkin, K. S. Novoselov, P. Dai, L. Balicas, and E. J. G. Santos, *The magnetic genome of two-dimensional van der Waals materials*, ACS Nano **11**, 35 (2022).

[112] F. Wu, I. Gutiérrez-Lezama, S. A. López-Paz, M. Gibertini, K. Watanabe, T. Taniguchi, F. O. von Rohr, N. Ubrig, and A. F. Morpurgo, *Quasi-1D electronic transport in a 2D magnetic semiconductor*, Advanced Materials **2022**, 2109759 (2022).

[113] F. Dirnberger, J. Quan, R. Bushati, G. M. Diederich, M. Florian, J. Klein, K. Mosina, Z. Sofer, X. Xu, A. Kamra, F. J. García-Vidal, A. Alù, and V. M. Menon, *Magneto-optics in a van der Waals magnet tuned by self-hybridized polaritons*, Nature **620**, 533 (2023).

[114] K. Lee, A. H. Dismukes, E. J. Telford, R. A. Wiscons, J. Wang, X. Xu, C. Nuckolls, C. R. Dean, X. Roy, and X. Zhu, *Magnetic order and symmetry in the 2D semiconductor CrSBr*, Nano Letters **21**, 3511 (2021).

[115] J. Beck, *Über chalkogenidhalogenide des chroms synthese, kristallstruktur und magnetismus von chromsulfidbromid, CrSBr*, Zeitschrift für anorganische und allgemeine Chemie **585**, 157 (1990).

[116] O. Göser, W. Paul, and H. Kahle, *Magnetic properties of CrSBr*, Journal of Magnetism and Magnetic Materials **92**, 129 (1990).

[117] S. A. López-Paz, Z. Guguchia, V. Y. Pomjakushin, C. Witteveen, A. Cervellino, H. Luetkens, N. Casati, A. F. Morpurgo, and F. O. von Rohr, *Dynamic magnetic crossover at the origin of the hidden-order in van der Waals antiferromagnet CrSBr*, Nature Communications **13** (2022).

[118] J. B. Goodenough, *Theory of the role of covalence in the perovskite-type manganites [La, M(II)]MnO_3*, Phys. Rev. **100**, 564 (1955).

[119] J. Kanamori, *Superexchange interaction and symmetry properties of electron orbitals*, Journal of Physics and Chemistry of Solids **10**, 87 (1959).

[120] K. Yang, G. Wang, L. Liu, D. Lu, and H. Wu, *Triaxial magnetic anisotropy in the two-dimensional ferromagnetic semiconductor CrSBr*, Physical Review B **104** (2021).

[121] C. Boix-Constant, S. Mañas-Valero, A. M. Ruiz, A. Rybakov, K. A. Konieczny, S. Pillet, J. J. Baldoví, and E. Coronado, *Probing the spin dimensionality in single-layer CrSBr van der Waals heterostructures by magneto-transport measurements*, Advanced Materials **34**, 2204940 (2022).

[122] E. J. Telford, A. H. Dismukes, R. L. Dudley, R. A. Wiscons, K. Lee, D. G. Chica, M. E. Ziebel, M.-G. Han, J. Yu, S. Shabani, A. Scheie, K. Watanabe, T. Taniguchi, D. Xiao, Y. Zhu, A. N. Pasupathy, C. Nuckolls, X. Zhu, C. R. Dean, and X. Roy, *Coupling between magnetic order and charge transport in a two-dimensional magnetic semiconductor*, Nature Materials **21**, 754 (2022).

[123] Y. Zur, A. Noah, C. Boix-Constant, S. Mañas-Valero, N. Fridman, R. Rama-Eiroa, M. E. Huber, E. J. G. Santos, E. Coronado, and Y. Anahory, *Magnetic imaging and domain nucleation in CrSBr down to the 2D limit*, Advanced Materials **35**, 2307195 (2023).

[124] T. Hingant, J.-P. Tetienne, L. J. Martínez, K. Garcia, D. Ravelosona, J.-F. Roch, and V. Jacques, *Measuring the magnetic moment density in patterned ultrathin ferromagnets with submicrometer resolution*, Phys. Rev. Applied **4**, 014003 (2015).

[125] X. Bo, F. Li, X. Xu, X. Wan, and Y. Pu, *Calculated magnetic exchange interactions in the van der Waals layered magnet CrSBr*, New Journal of Physics **25**, 013026 (2023).

[126] R. M. White, *Quantum Theory of Magnetism: Magnetic Properties of Materials*, (Springer Berlin Heidelberg) (2007).

[127] M. E. Ziebel, M. L. Feuer, J. Cox, X. Zhu, C. R. Dean, and X. Roy, *CrSBr: An air-stable, two-dimensional magnetic semiconductor*, Nano Letters **24**, 4319–4329 (2024).

[128] C. Ye, C. Wang, Q. Wu, S. Liu, J. Zhou, G. Wang, A. Söll, Z. Sofer, M. Yue, X. Liu, M. Tian, Q. Xiong, W. Ji, and X. Renshaw Wang, *Layer-dependent interlayer antiferromagnetic spin reorientation in air-stable semiconductor CrSBr*, ACS Nano **16**, 11876 (2022).

[129] A. Vansteenkiste, J. Leliaert, M. Dvornik, M. Helsen, F. Garcia-Sanchez, and B. Van Waeyenberge, *The design and verification of Mumax3*, AIP Advances **4**, 107133 (2014).

[130] J. Leliaert, J. Mulkers, J. De Clercq, A. Coene, M. Dvornik, and B. Van Waeyenberge, *Adaptively time stepping the stochastic Landau-Lifshitz-Gilbert equation at nonzero temperature: implementation and validation in MuMax*^{3}, AIP Advances **7**, 125010 (2017).

[131] L. Exl, S. Bance, F. Reichel, T. Schrefl, H. Peter Stimming, and N. J. Mauser, *LaBonte's method revisited: An effective steepest descent method for micromagnetic energy minimization*, Journal of Applied Physics **115**, 17D118 (2014).

[132] A. Jain, P. Bharadwaj, S. Heeg, M. Parzefall, T. Taniguchi, K. Watanabe, and L. Novotny, *Minimizing residues and strain in 2D materials transferred from PDMS*, Nanotechnology **29**, 265203 (2018).

[133] E. C. Stoner and E. P. Wohlfarth, *A mechanism of magnetic hysteresis in heterogeneous alloys*, Philosophical Transactions of the Royal Society of London. Series A, Mathematical and Physical Sciences **240**, 599 (1948).

[134] A. Dubois, D. Broadway, A. Stark, M. Tschudin, A. Healey, S. Huber, J.-P. Tetienne, E. Greplova, and P. Maletinsky, *Untrained physically informed neural network for image reconstruction of magnetic field sources*, Physical Review Applied **18**, 064076 (2022).

[135] T. M. J. Cham, S. Karimeddiny, A. H. Dismukes, X. Roy, D. C. Ralph, and Y. K. Luo, *Anisotropic gigahertz antiferromagnetic resonances of the easy-axis van der Waals antiferromagnet CrSBr*, Nano Letters **22**, 6716 (2022).

[136] F. Moro, S. Ke, A. G. del Águila, A. Söll, Z. Sofer, Q. Wu, M. Yue, L. Li, X. Liu, and M. Fanciulli, *Revealing 2D magnetism in a bulk CrSBr single crystal by electron spin resonance*, Advanced Functional Materials **32**, de2207044 (2022).

[137] J. H. Zhao, H. P. Kunkel, X. Z. Zhou, G. Williams, and M. A. Subramanian, *Critical behavior of the magnetoresistive pyrochlore* $Tl_2Mn_2O_7$, Physical Review Letters **83**, 219 (1999).

[138] H. E. Stanley, *Introduction to phase transitions and critical phenomena*, , International Series of Monographs on Physics (Oxford University Press) (1987).

[139] S. T. Bramwell and P. C. Holdsworth, *Magnetization and universal sub-critical behaviour in two-dimensional XY magnets*, Journal of Physics: Condensed Matter **5**, L53 (1993).

[140] A. Scheie, M. Ziebel, D. G. Chica, Y. J. Bae, X. Wang, A. I. Kolesnikov, X. Zhu, and X. Roy, *Spin waves and magnetic exchange Hamiltonian in CrSBr*, Advanced Science **9**, 2202467 (2022).

[141] E. J. Telford, D. G. Chica, M. E. Ziebel, K. Xie, N. S. Manganaro, C.-Y. Huang, J. Cox, A. H. Dismukes, X. Zhu, J. P. S. Walsh, T. Cao, C. R. Dean, and X. Roy, *Designing magnetic properties in CrSBr through hydrostatic pressure and ligand substitution*, Advanced Physics Research **2** (2023).

[142] J. M. Kosterlitz and D. J. Thouless, *Ordering, metastability and phase transitions in two-dimensional systems*, Journal of Physics C: Solid State Physics **6**, 1181 (1973).

[143] C. Boix-Constant, S. Jenkins, R. Rama-Eiroa, E. J. G. Santos, S. Mañas-Valero, and E. Coronado, *Multistep magnetization switching in orthogonally twisted ferromagnetic monolayers*, Nature Materials **23**, 212 (2024).

[144] Z. He, K. Dou, W. Du, Y. Dai, B. Huang, and Y. Ma, *Multiple topological magnetism in van der Waals heterostructure of $MnTe_2/ZrS_2$*, Nano Letters **23**, 312 (2023).

[145] K.-M. Kim, D. H. Kiem, G. Bednik, M. J. Han, and M. J. Park, *Theory of moire magnets and topological magnons: Applications to twisted bilayer CrI_3*, arXiv:2206.05264 (2022).

[146] S. S. P. Parkin, M. Hayashi, and L. Thomas, *Magnetic domain-wall racetrack memory*, Science **320**, 190 (2008).

[147] N. B. Weber, H. Ohldag, H. Gomonaj, and F. U. Hillebrecht, *Magnetostrictive domain walls in antiferromagnetic NiO*, Physical Review Letters **91** (2003).

[148] S.-W. Cheong, M. Fiebig, W. Wu, L. Chapon, and V. Kiryukhin, *Seeing is believing: visualization of antiferromagnetic domains*, npj Quantum Materials **5**, 3 (2020).

[149] T. Jungwirth, X. Marti, P. Wadley, and J. Wunderlich, *Antiferromagnetic spintronics*, Nature Nanotechnology **11**, 231 (2016).

[150] V. Baltz, A. Manchon, M. Tsoi, T. Moriyama, T. Ono, and Y. Tserkovnyak, *Antiferromagnetic spintronics*, Rev. Mod. Phys. **90**, 015005 (2018).

[151] N. Hedrich, K. Wagner, O. V. Pylypovskyi, B. J. Shields, T. Kosub, D. D. Sheka, D. Makarov, and P. Maletinsky, *Nanoscale mechanics of antiferromagnetic domain walls*, Nature Physics **17**, 574–577 (2021).

[152] L. Thiel, D. Rohner, M. Ganzhorn, P. Appel, E. Neu, B. Müller, R. Kleiner, D. Koelle, and P. Maletinsky, *Quantitative nanoscale vortex imaging using a cryogenic quantum magnetometer*, Nature Nanotechnology **11**, 677 (2016).

[153] T. van der Sar, F. Casola, R. Walsworth, and A. Yacoby, *Nanometre-scale probing of spin waves using single electron spins*, Nature Communications **6** (2015).

[154] I. Bertelli, B. G. Simon, T. Yu, J. Aarts, G. E. W. Bauer, Y. M. Blanter, and T. van der Sar, *Imaging spin-wave damping underneath metals using electron spins in diamond*, Advanced Quantum Technologies **4** (2021).

[155] D. MacNeill, J. T. Hou, D. R. Klein, P. Zhang, P. Jarillo-Herrero, and L. Liu, *Gigahertz frequency antiferromagnetic resonance and strong magnon-magnon coupling in the layered crystal $CrCl_3$*, Physical Review Letters **123** (2019).

[156] A. K. Behera, S. Chowdhury, and S. R. Das, *Magnetic skyrmions in atomic thin CrI_3 monolayer*, Applied Physics Letters **114** (2019).

[157] M. Kapfer, B. S. Jessen, M. E. Eisele, M. Fu, D. R. Danielsen, T. P. Darlington, S. L. Moore, N. R. Finney, A. Marchese, V. Hsieh, P. Majchrzak, Z. Jiang, D. Biswas, P. Dudin, J. Avila, K. Watanabe, T. Taniguchi, S. Ulstrup, P. Bøggild, P. J. Schuck, D. N. Basov, J. Hone, and C. R. Dean, *Programming twist angle and strain profiles in 2D materials*, Science **381**, 677–681 (2023).

[158] A. Inbar, J. Birkbeck, J. Xiao, T. Taniguchi, K. Watanabe, B. Yan, Y. Oreg, A. Stern, E. Berg, and S. Ilani, *The quantum twisting microscope*, Nature **614**, 682–687 (2023).

[159] J.-P. Tetienne, *Quantum sensors go flat*, Nature Physics **17**, 1074–1075 (2021).

[160] A. Gottscholl, M. Diez, V. Soltamov, C. Kasper, D. Krauße, A. Sperlich, M. Kianinia, C. Bradac, I. Aharonovich, and V. Dyakonov, *Spin defects in hBN as promising temperature, pressure and magnetic field quantum sensors*, Nature Communications **12** (2021).

[161] A. Durand, T. Clua-Provost, F. Fabre, P. Kumar, J. Li, J. Edgar, P. Udvarhelyi, A. Gali, X. Marie, C. Robert, J. Gérard, B. Gil, G. Cassabois, and V. Jacques, *Optically active spin defects in few-layer thick hexagonal boron nitride*, Physical Review Letters **131** (2023).

[162] S. Tan, Y. P. Ma, I. Thomas, and J. Wikswo, *Reconstruction of two-dimensional magnetization and susceptibility distributions from the magnetic field of soft magnetic materials*, IEEE Transactions on Magnetics **32**, 230–234 (1996).

[163] Y. Dovzhenko, F. Casola, S. Schlotter, T. X. Zhou, F. Büttner, R. L. Walsworth, G. S. D. Beach, and A. Yacoby, *Magnetostatic twists in room-temperature skyrmions explored by nitrogen-vacancy center spin texture reconstruction*, Nature Communications **9** (2018).

[164] J. M. D. Coey, *Magnetism and magnetic materials*, (Cambridge University Press) (2010).

[165] *mumax3 gpu-accelerated micromagnetism*, `https://mumax.github.io/examples.html`, accessed: 2024-05-10.

Acknowledgment

This PhD has been a long and exciting journey traversing the flatland of 2D magnets, climbing domain walls and passing the forest of diamond tips. I would not have found my way through this maze without the help of many people along the path.

First, and foremost I would like to thank my supervisor, Patrick, for giving me the opportunity to do a PhD thesis in his group. Patrick, thank you for granting me the freedom to explore a wide range of research directions and giving me guidance, help and assistance when I was about to loose track of my hiking path through the PhD. Your great enthusiasm about physics is very inspiring and I much enjoyed all of our discussions whether about magnetism, spins or cryogenics (and bouldering)! I also appreciate the positive and cheerful way in which you are leading the Quantum Sensing Group (and your humor, even if some Germans in the group try to overstretch it), all of this sets a wonderful atmosphere in your group. I would also like to thank Christian for taking over the role of my second supervisor. My excitement about experimental quantum physics goes back to a summer lab course during my Bachelor studies in Christian's group. Ever since you have helped and encouraged me and I am very grateful for all the support you have and still are giving me. Reading a PhD thesis and traveling to Switzerland for a defense is time consuming and I am very thankful to Roman for willing to take on all these duties as the external referee of my thesis. I have learned and benefited a lot from all our discussions on research matters.

My journey as a PhD student included many formative exchanges abroad. First, I would like to thank Pablo for welcoming me at MIT during the beginning of my PhD. I have learned invaluable insights about 2D magnets in the PJH group! I would like to thank especially Dahlia and David for including me in the 2D Magnets team and teaching me everything about making tiny, magnetic sandwiches! I would also like to thank Amir for hosting me at Harvard for an exchange towards the end of my PhD. I have learned a lot working on NV experiments with 2D magnets in the Y-lab and I would like to thank in particular Ruolan and Nikola for including me in your team. Furthermore, I am very grateful for all our collaborators, specifically to the Morpurgo lab from Geneva and the Roy and Dean labs from Columbia University NY, for providing us with beautiful samples.

I had the luck to work alongside many very experienced people in the lab. Thank you Lucas for teaching me everything about your low temperature NV magnetometry setup, about ice cream breaks and German jokes. I had an amazing start into both the research on 2D magnetism and the Quantum Sensing group thanks to you! During the majority of my PhD I was working with David, our Australian PostDoc in the 4K-Team. We faced so many difficult times in the lab with our setups, but your incredible optimism, efficiency and motivation helped us to overcome all these obstacles, thanks to you we are the 2K4K team now! You have also greatly enriched my to-watch-list for comedy and TV shows and taught me the true art of good coffee (well, as good as it can get in Switzerland). Although never officially assigned as my PostDoc, Paritosh has taken over the roll to help and support me with all the 2D-fabrication related topics in my PhD. Thank you for the countless hours of helping me debug the transfer setup and for all the lunches and coffee breaks to fight the frustration

of sample fabrication. Finally, joining towards the end of my PhD, Clément took over the role of the 2K4K-PostDoc. I am very thankful that you read and re-read almost my entire thesis (even on my very last minute schedule) and helped me to manage to finish this project just in time. Your dedication in the lab helped push our experiments forward a lot and your very french humor spreads a great mood in the team (but we do need to discuss your taste of *Abondance* cheese!).

Besides the PostDocs I was working alongside a fantastic team of PhDs and Master students. P2 (Patrick), thank you for sharing all the ups and downs of such a PhD journey. I am very grateful for all your support, the great team work and the Rheinswimmings and conference trips we could share! Thank you Debarghya for all your efforts in the lab and for bringing the magnons to life in our 2D magnets. And Carolin, thank you for giving me the chance to supervise you during your Master Thesis and for not only sharing interests in physics but also in ice cream and sushi! I would also like to thank all of the Quantum Sensing Group members who have made these 5 years special! And in particular, thank you to the best office crew in the world Johannes, Josh and Beat. And thank you Paul and Silvia for all your valuable tips and tricks concerning Quantum Sensing Minis.

Throughout my academic career I was lucky to have the support from two very inspiring professors. Thank you Lily for introducing me to the world of NVs in diamond and for encouraging me in the lab. Thank you Ilaria for including me in our department's women in physics group and for all your advice on how to navigate through life at University. Of course non of our experiments would have worked if it wasn't for all the help we got from our University staff! Thank you for providing us with helium, for fabricating complex custom designed parts and pieces for our experiments, for your patience with our reimbursement sheets, for keeping the cleanroom running and the list goes on and on.

Sometimes a PhD can get almost unbearably hard - and it was with the help of my friends that I managed to continue on my path of the PhD journey. At the University I have gotten to know many great scientists who have also become dear friends. Thank you Dahlia, Viktoria, Noemi, Nadine and Brendan for keeping in touch even across oceans and different time zones! Thank you to Max and Johannes for the time at E6, I think no other WG can top our attic bouldering wall! Thank you also to our bouldering (and surviving-through-hard-PhD-phases)crew, Ramon, Pascal and Yannik, I think my bouldering skills scaled inversely with my motivation in the lab. And thank you for the countless coffees, ice creams and movie nights to Livia and Max and Sofie and Juli! Many thanks for the endless long phone calls, hikes, weekend trips and plenty of dinners Salome and Anja!

Last but not least I would like to thank my family. Thank you Mama and Papa for supporting me on my PhD adventures in every way, for visiting me when I decided to go abroad and for always cheering me on. Thank you Moritz for being the best littlebig brother and for brightening my mood with your unpaired humor. Xav, no words can describe how grateful I am to live life with you! Thank you for all the morning coffees, late night teas, bouldering trips, Sunday walks in Langescheisse, climbing session in Ticino, the list could go on forever..! You helped me in the most beautiful way to master this PhD. Und danke kline Finn dass du mi wortwörtlich gingt hesch zum dä PhD abzschliesse, du bisch die schönsti Motivation gse und ich freu mi uf alli neue Abentür mit dir und em Xav! ♡